

DENDRITIC SIGNAL INTEGRATION IN HIPPOCAMPAL INTERNEURONS

PhD thesis

Attila Kaszás

János Szentágothai Neurosciences Doctoral School
Semmelweis University



Supervisors: Prof. E. Sylvester Vizi MD, D.Sc
Balázs J. Rózsa MD, PhD

Official opponents:
Dr. Zoltán Kisvárdy MD, D.Sc
Dr. Anita Kamondi CsC

Head of the Final Examination Committee:
Dr. József Kiss MD, D.Sc

Members of the Final Examination Committee:
Dr. István Ulbert PhD
Dr. Árpád Dobolyi MD, PhD

Budapest, 2012

I. TABLE OF CONTENTS

I. TABLE OF CONTENTS	1
II. LIST OF ABBREVIATIONS	4
III. FOREWORD	6
IV. INTRODUCTION TO THE LITERATURE	7
IV.1. Hippocampal Structure and Circuitry.....	8
IV.2. Interneurons of the Hippocampus – A Brief Overview	10
IV.3. Dendritic Characteristics	13
IV.3.1. Dendritic Morphology	13
IV.3.2. Dendritic Physiology	14
IV.3.2.1 Passive Dendrites	15
IV.3.2.2 Active Neuronal Processes	17
IV.3.3. Dendritic Signal Integration	19
IV.3.4. Dendritic Spikes	20
IV.3.4.1 Dendritic Sodium Spikes.....	21
IV.3.4.2 Dendritic Calcium Spikes.....	23
IV.3.4.3 Dendritic NMDA Spikes	25
IV.3.5. The Role of nAChRs in Active Dendritic Processes.....	27
IV.4. Two-Photon Microscopy for Neuroscience	28
IV.4.1. Introduction on Two-Photon Microscopy	29
IV.4.2. Laser Light Sources.....	31
IV.4.3. Scanning Methods (<i>x-y</i> plane).....	32
IV.4.4. Objectives	34
IV.4.5. Detectors.....	35
IV.4.6. Three-Dimensional Imaging by Fast Objective Movement	36
IV.4.7. Three-Dimensional Imaging by Acousto-Optic Scanning	37
V. AIMS	38
VI. METHODS	39
VI.1. Slice Preparation and Electrophysiology	39
VI.2. Dual Superfusion Chamber	40
VI.3. Roller Coaster Scanning	41

VI.4. Calcium Imaging	42
VI.5. Calculating Supralinearity	44
VI.6. Two-Photon Uncaging	45
VI.7. Investigating nAChR Effects	46
VI.8. Histology	47
VI.9. Data Analysis and Statistics	47
VII. RESULTS.....	49
VII.1. Synaptic Integration Between Dendritic Computational Subunits	49
VII.1.1. Electrical Stimulation.....	49
VII.1.2. Two-Photon Photoactivation of Glutamate	54
VII.1.3. Coincidence Detection in CA1 Interneuron Dendrites	57
VII.1.4. Distance Dependence of Signal Integration in CA1 Interneurons	61
VII.1.5. Spatial Characteristics of Dendritic Signal Integration in CA1 Interneurons	62
VII.2. Active Dendrites in CA1 Str. Rad. Interneurons	68
VII.3. Channels Taking Part in Synaptic Processing.....	75
VII.3.1. N-methyl-D-aspartate Receptors (NMDAR).....	75
VII.3.2. Voltage-Gated Calcium Channels (VGCCs)	81
VII.3.3. Voltage-Dependent Sodium Channels (Na _v).....	82
VII.3.4. Nicotinic Acetylcholine Receptors (nAChRs).....	84
VII.4. Dendritic Spike Propagation	86
VII.5. Action Potential Backpropagation in Interneuron Dendrites	88
VII.5.1. Dendritic NMDA-Spikes and bAPs in Interneurons.....	89
VII.5.2. Nicotinic Effects on bAPs.....	91
VIII. DISCUSSION	94
VIII.1. Novel Imaging Methods Applied in Search of Dendritic Phenomena	94
VIII.2. Cable Theory and Compensatory Mechanisms for Signal Loss.....	95
VIII.3. Compartmentalization in Dendritic Processes.....	97
VIII.4. Dendritic Signal Amplification.....	98
VIII.5. Dendritic Spikes	98
VIII.6. Spontaneously Occurring NMDA-Spikes	100
VIII.7. nAChRs and Dendritic Function in Hippocampal Interneurons	102

VIII.8. $\alpha 7$ -nAChRs and Plasticity	103
IX. CONCLUSIONS	105
X. ÖSSZEFOGLALÁS.....	107
XI. SUMMARY	108
XII. BIBLIOGRAPHY.....	109
XIII. LIST OF THE AUTHOR'S PUBLICATIONS.....	133
XIII.1. Publications Related to the Thesis.....	133
XIII.2. Patents Related to the Thesis	133
XIII.3. Other Publications	134
XIV. ACKNOWLEDGEMENTS	135

II. LIST OF ABBREVIATIONS

2P – two-photon

3D – three-dimensional

AC – associational commissural fibers

ACh – acetylcholine

AO – acousto-optic

AOD – acousto-optic deflector

AMPA – α -amino-3-hydroxy-5-methyl-4-isoxazole propionic acid

AMPA-receptor – α -amino-3-hydroxy-5-methyl-4-isoxazole propionic acid receptor

AP – action potential

bAP – backpropagating action potential

CA – Cornu Ammonis

CA1 – hippocampal CA1 region

CA3 – hippocampal CA3 region

CB – calbindin

CCD – charge-coupled device

CCK – cholecystokinin

C_m – membrane capacitance

CR – calretinin

CV – coefficient of variation

DG – dentate gyrus

dSpike – dendritic spike

EC – entorhinal cortex

EPSP – excitatory postsynaptic potential

GABA – γ -aminobutyric acid

gluEPSP – uncaging-evoked excitatory postsynaptic potential

HC – hippocampus

HCN – hyperpolarization-activated cation channel

IN – interneuron

IR – infrared

ISI – interstimulus interval

LEC – lateral entorhinal cortex

LM – stratum lacunosum-moleculare
LPP – lateral perforant path
LTP – long-term potentiation
MEC – medial entorhinal cortex
mEPSC – miniature excitatory postsynaptic current
MF – mossy fibers
MPP – medial perforant path
NA – numerical aperture
nAChR – nicotinic acetylcholine receptor
Nav – voltage-gated Sodium channel
NPY – neuropeptide-Y
NMDA – N-methyl-D-aspartate
NMDAR – N-methyl-D-aspartate receptor
OGB-1 – oregon green BAPTA-1
O-LM – oriens–lacunosum-moleculare
PMT – photomultiplier
PP – perforant path
PPR – paired-pulse ratio
RAD-LM – radiatum–lacunosum-moleculare
ROI – region of interest
 R_i – internal axis resistance
 R_m – membrane resistance
SC – Schaffer collateral
SNR – signal to noise ration
SST – somatostatin
Str. rad. – stratum radiatum
TIR – transmission infrared
TTX – tetrodotoxin
uEPSC – unitary excitatory postsynaptic current
uEPSP – unitary excitatory postsynaptic potential
VGLUT – vesicular glutamate transporter
VIP – vasoactive intestinal peptide

III. FOREWORD

The human brain consists of approximately 80 billion neurons and despite their vast numbers, they do their tasks almost unnoticeably. The nature of this task is the question for many researchers: how simple, cellular or even subcellular events can add up to produce such complex behavioral patterns as running, having a conversation or remembering past events. These patterns can be pictured as different levels of computation, all performed by anatomically separated structures of single neurons or neuronal networks that are synaptically interconnected in almost infinite ways.

As formulated by David Marr in his book *Vision* (Marr 1982), the information processing in the brain can be divided into three levels. The *computational theory* level defines what the goal of the processing is; the *representational and algorithmic* level determines how the input and output is represented and how the information is transformed, while the third level, *hardware implementation* shows how the representation and algorithm can be realized physically. Though these theories still stand, only recent advances in the methodology could provide the means for their thorough experimental testing, with the proper technical methods to observe or resolve the physical and temporal subcomponents.

This work will focus on the representational and algorithmic level, mainly dealing with how the inputs and outputs are represented and how they are transformed by the subcellular physical components of the network. Nevertheless, the data presented will give insight on the hardware implementation level as well, since the structural characteristics of the neuronal processes are inherently observed with the microscopy techniques used.

The last two decades have brought results showing how the major excitatory components of the network – the pyramidal cells – process inputs on the local, subcellular level. The results shown here on the inhibitory neurons integrate into the research aiming at the identification of the subcellular basic building blocks of information processing that has been rising with the coming of novel research methods. As such, they might provide a glimpse on the unnoticeable action of brain computation, by showing how major controllers of neuronal activity – the inhibitory interneurons – do their input processing in the local compartments of their dendritic processes.

IV. INTRODUCTION TO THE LITERATURE

The cellular structure of neuronal cells has long intrigued scientists dealing with the nervous system. These issues were first scrupulously examined more than a 100 years ago in the works of Santiago Ramón Y Cajal (Ramón y Cajal 1909; Ramón y Cajal 1990), underlining two major hypotheses in studying the neuronal processes (**Fig. 1**). Cajal noticed that axons and dendrites – despite being greatly intertwined – are separate cellular processes and do not fuse in anastomotic structures. This strengthened the notion of the *Neuron Doctrine* (**Fig. 1B**), which states that instead of being a reticular structure, the brain is formed by neurons that are independent entities. Secondly, based on morphological studies only, he established the law of *dynamic polarization* (**Fig. 1C**), describing that the direction of information flow is from the axons towards the dendrites in the network.

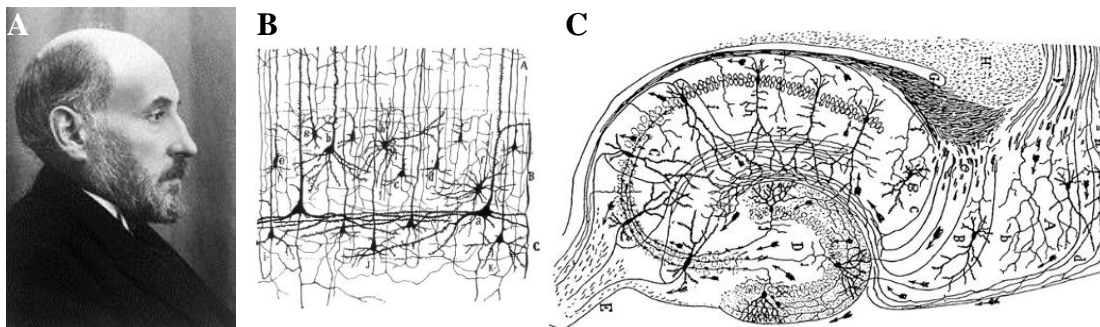


Figure 1 – The Neuron Doctrine and the law of dynamic polarization.

A) Santiago Ramón Y Cajal (1852-1934). **B)** Ramón y Cajal's drawing of different types of pyramidal neurons in layers 5–7 of the 15-day-old human infant visual cortex, using the Golgi method. **C)** The graphical representation of the hippocampus by Cajal showing the presumed flow of information and the layered structure of the hippocampus. *Source: (Ramón y Cajal 1909)*

Our view on the communication between neurons has since expanded, as not just axo-dendritic, but axo-axonic (Somogyi et al. 1982; Buhl et al. 1994) and dendro-dendritic connections (Rall et al. 1966; Price and Powell 1970) have also been discovered. Although many studies dealt with synaptic transmission, the integration of

local signals on the postsynaptic site has been extensively studied only recently, since new techniques – both electrophysiological and imaging-based dendritic recordings – were needed to uncover how these local phenomena take place (Svoboda et al. 1996; Svoboda et al. 1997; Helmchen et al. 1999; Nevian et al. 2007).

In order to analyze the information processing conducted by the neurons in the hippocampus, one first needs to place them in their anatomical location and familiarize with their classifications. As such, I will give a brief anatomical description on macroanatomical structure of the hippocampal formation, and then provide a brief classification of interneurons in the hippocampus. Since my aim is to point out what role the smallest computational subunits might play in large-scale computations, I will characterize the subcellular structure of neurons, with tight focus on their dendrites. Here, I will give a more detailed description of the currently known passive and active dendritic processing capabilities. Finally, since my work involves many technical aspects, I will introduce the novel imaging methods currently available for fine-scale or large-scale neuroscience research.

IV.1. Hippocampal Structure and Circuitry

The hippocampal formation is a set of structures situated in the medial temporal lobe that consists of the dentate gyrus, the hippocampus proper or Cornu Ammonis (CA), the presubiculum, the subiculum, the parasubiculum and the entorhinal cortex (Andersen 2007). The coronal section of the hippocampus gives an explanation to why it is called the archicortex: when compared to the layered nature of the neocortex, the hippocampus has similar lamellar anatomy, but lags behind in the number of layers. Though the different parts of the CA regions show different layers, the basic layers from dorsal to ventral in the adult rat hippocampus are (**Fig. 2**):

1. stratum oriens: scattered interneurons and glial cells can be seen here, with efferent inputs from the amygdala
2. stratum pyramidale: the pyramidal layer is mostly built up of densely packed pyramidal cells

3. stratum radiatum: the name is derived from the radiating pyramidal cell apical dendrites; CA3 innervates the apical dendrites of CA1 pyramidal cells here, through the Schaffer-collaterals.
4. stratum lacunosum-moleculare: the molecular layer, with efferent inputs from the entorhinal cortex and the thalamus.

The CA1 region has a more prominent pyramidal layer, with bigger pyramidal cells, while CA3 has a lucidum layer under the pyramidal layer, where mossy fibers terminate from the dentate gyrus. As my work does not involve the dentate gyrus, I will not deal with its detailed structure and from here on by hippocampus I will address only the CA1-3 regions.

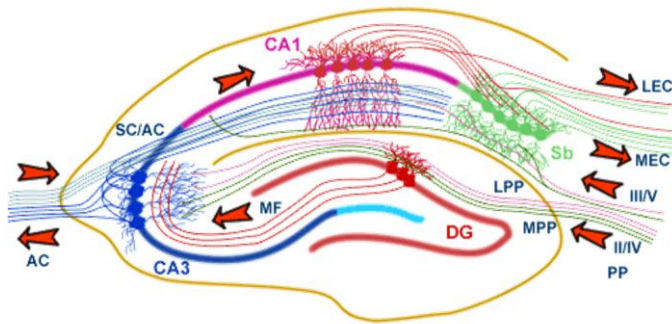


Figure 2 – Basic hippocampal pathways.

The afferent and efferent excitatory inputs of the hippocampal formation.

Abbreviations: LEC: lateral entorhinal cortex; MEC: medial entorhinal cortex; PP: perforant path; LPP: lateral perforant path; MPP: medial perforant path; DG: dentate gyrus; MF: mossy fibers; SC: Schaffer collateral; AC: associational commissural fibers. Source: <http://www.bristol.ac.uk/synaptic/pathways/>

The hippocampus proper receives many inputs from the entorhinal cortex, the contralateral hippocampus, the amygdala, the thalamus, and projects amongst others to the septum and the retrosplenial cortex. The well-described trisynaptic loop forms the basic input and output pathways in the hippocampus proper. Here, the inputs arriving from the entorhinal cortex layer II/IV through the perforant path reach the DG granule cells, which then innervate the CA3 pyramidal cells, which – through the Schaffer collaterals – innervate the CA1 stratum radiatum. Other inputs include the direct innervation from EC Layer III/V to the CA1 pyramidal cell distal dendrites in str. lacunosum-moleculare, or the direct innervation of CA3 pyramidal cells through EC Layer II/IV.

The hippocampus, amongst its various and very important functions in cognition such as in attention, has an essential role in memory formation and spatial navigation (O'Keefe and Dostrovsky 1971; Burgess et al. 2002). The role it plays in memory formation and spatial navigation is clearly linked to the network oscillations, mostly to theta and gamma oscillation appearing under different brain states (Burgess et al. 2002; Klausberger et al. 2003; Buzsáki 2006; Tukker et al. 2007).

IV.2. Interneurons of the Hippocampus – A Brief Overview

One of many exceptional students and followers of Ramón Y Cajal was Lorente de Nó, who stated that “The pyramidal cells will carry the impulses further, and the internuncial neurons have to regulate the discharge of the efferent ones.” (Lorente de Nó 1938), giving birth to the notion of the internuncial neurons or interneurons. These were the relay neurons that connected sensory systems of the peripheral nervous system or the local connectors of cortical circuits. Though interneurons in the developing nervous system can be excitatory, most interneurons in the mature central nervous system are usually inhibitory, releasing γ -aminobutyric acid (GABA) or glycine that exert hyperpolarizing action on the postsynaptic neuron. Exceptions are rare, such as the axo-axonic or chandelier neurons in the neocortex (Szabadics et al. 2006).

Since there is a large difference in morphology, immunohistochemical markers, intrinsic electrical properties and hence firing and summation characteristics, the proper classification of interneurons is a major issue. According to immunohistochemical markers, we can differentiate between cholecystokinin-positive (CCK+), calbindin-positive (CB+), vesicular intestinal peptide positive (VIP+), neuropeptide-Y positive (NPY+), somatostatin-positive (SST+), enkephalin-positive and parvalbumin-positive (PV+) interneurons (Freund and Buzsaki 1996). Another classification is based on the target of innervation or projection for the interneurons. According to these properties, interneurons can be targeting the somata of principal cells (e.g. basket cells) (Martin et al. 1983; Buhl et al. 1994; Halasy et al. 1996), the axon initial segment of pyramidal cells (axo-axonic cells) (Somogyi et al. 1982) or the dendrites of pyramidal cells (e.g. dendrite-targeting bistratified cells) (Klausberger 2009; Takacs et al. 2011). The classification markers have been collected to provide a standard for the proper grouping

of cells (Ascoli et al. 2008). The relation between different immunohistochemical and innervation characteristics in the hippocampus have been thoroughly described in two recent reviews, as shown on **Fig. 3** (Klausberger and Somogyi 2008; Klausberger 2009).

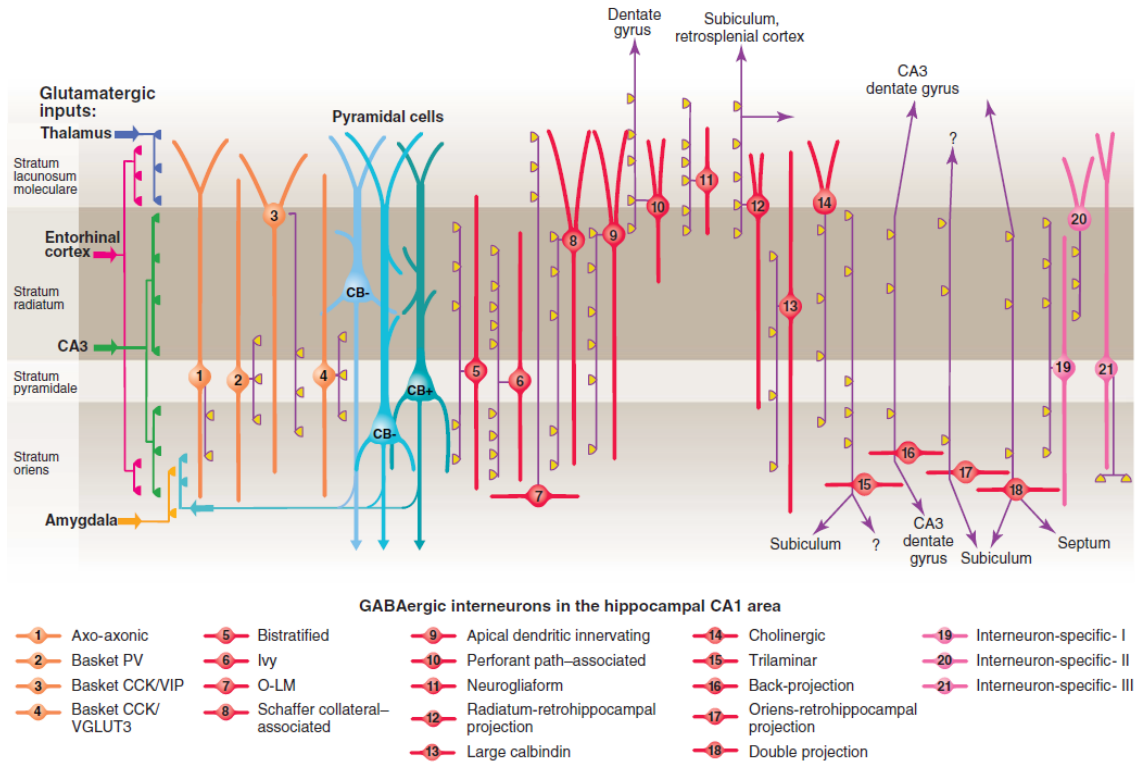


Figure 3 – Interneuron subtypes in the hippocampal CA1 area.

Three types of pyramidal cell are accompanied by at least 21 classes of interneuron in the hippocampal CA1 area. The main termination of five glutamatergic inputs are indicated on the left. The somata and dendrites of interneurons innervating pyramidal cells (blue) are orange, and those innervating mainly other interneurons are pink. Axons are purple; the main synaptic terminations are yellow. VIP, vasoactive intestinal polypeptide; VGLUT, vesicular glutamate transporter; O-LM, oriens lacunosum moleculare. *Source: (Klausberger and Somogyi 2008).*

The electrophysiological characteristics of interneurons can be used to define a separate set of properties, which is – of course – intertwined with the immunohistochemical markers. According to the Petilla convention, regarding their electrophysiological properties interneurons can be placed into five major groups (Lamsa et al. 2007; Ascoli et al. 2008):

1. Regular-spiking non-pyramidal neurons
 - a) Rebounding regular-spiking non-pyramidal neurons
 - b) Non-rebounding regular-spiking non-pyramidal neurons
 - c) Rapidly adapting regular-spiking non-pyramidal neurons
2. Fast-spiking interneurons
3. Burst-spiking non-pyramidal neurons
4. Irregularly-spiking interneurons
5. Delayed-spiking interneurons.

Regular spiking interneurons usually fire at 60Hz to 120Hz (Lamsa et al. 2007). When using a 500 ms depolarizing step in current clamp mode and driven at maximum firing frequency, these cells display moderate levels around (30%) of firing adaptation, meaning that the interspike interval of the first few spikes is nearly the same as that of the last few spikes, except for a subgroup showing high adaptation levels of around 60%. After the current step, when the cell is set to resting membrane potential, some of these show rebounding action potentials, possibly as a result of higher hyperpolarization-activated cyclic nucleotide-gated (HCN) channel density. Fast spikers show spike rates ranging from 120 Hz to 300 Hz, and very low firing adaptation below 20%. Burst-spiking non-pyramidal neurons show “stuttering” in their firing rate during the current step, giving short, high frequency burst of action potentials, and they show rebound action potential bursts. Irregular-spiking interneurons do not have a clear pattern of firing, and fire action potential at random during the current step, while delayed spikers show a long onset time of approximately 50 ms to 80 ms for action potentials at the beginning of the current step, which is followed by a regular spiking pattern of around 40 to 60Hz (Lamsa et al. 2007).

IV.3. Dendritic Characteristics

IV.3.1. Dendritic Morphology

The dendrite is what Cajal called a ‘protoplasmic expansion’ (Ramón y Cajal 1909); an extension of the cell body specialized for receiving and processing synaptic inputs, similar to the cell body in intracellular organelles, containing smooth endoplasmic reticulum and machinery for both mass transport and protein synthesis. In contrast, axons contain almost exclusively microtubules with the transport machinery, with mitochondria and the release machinery usually accumulating near the boutons or release sites. Another major difference between dendritic and axonal processes is the thickness of the structure, where axons stay at a lower thickness of approximately 0.2-0.5 μm , while dendrites rarely reach such minimal thickness of 0.5 μm . The structural components of the dendrites give three major groups, according to morphological properties (**Fig. 4**):

1. *Dendritic shaft*. The main structural element of the dendrite. The tapering of dendrites towards the distal parts away from the soma has functional implications (Rall 1969b). They contain a lower number of synapses, in pyramidal cells mostly inhibitory ones, while in aspiny interneurons the excitatory and inhibitory synapses are intermingled (Gulyas et al. 1999; Takacs et al. 2011).
2. *Bifurcations*. The branching of dendritic shafts happens at these points. The dendrites can be categorized according to these as first order (originating from the soma), second order (dendritic branch after the first bifurcation), third order (after the second bifurcation), etc. They can play a role in functional specializations (hot or cold spots) (Larkum et al. 2009).
3. *Fine dendritic processes*. The synaptic specializations of dendrites. These can be filopodia, excrescences, appendages, dendritic endings or different forms of spines.

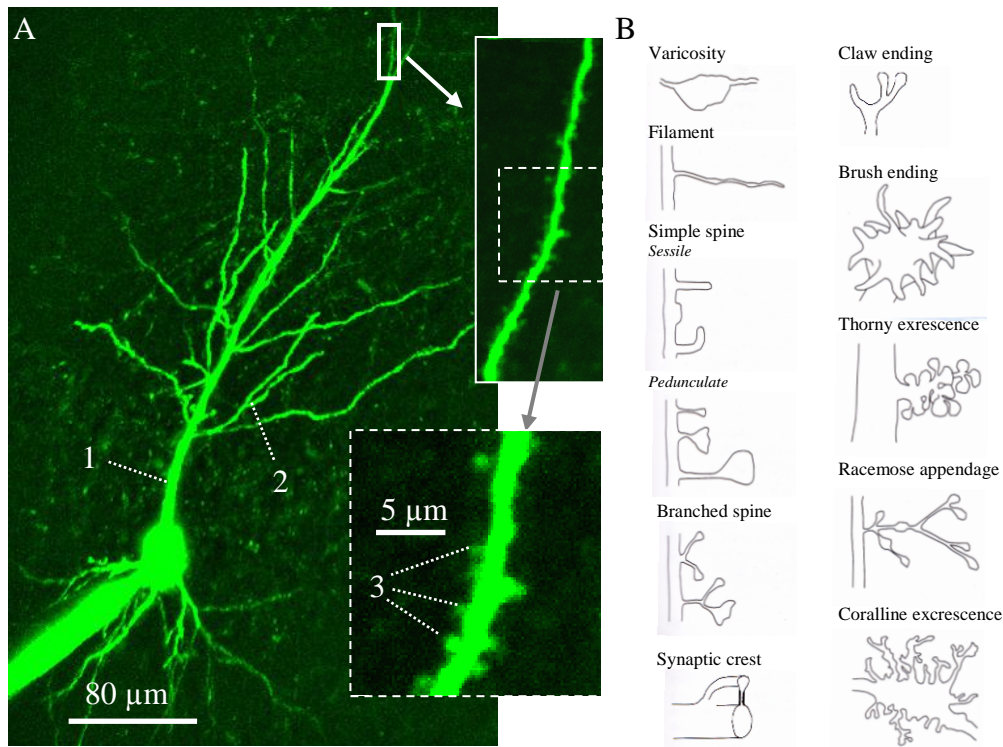


Figure 4 – Morphology of dendrites.

A) Maximum z-projection view of an Oregon Green BAPTA-1 filled hippocampal CA1 pyramidal cell imaged with a three-dimensional acousto-optic microscope. Insets: enlarged views of a spiny dendritic branch. 1: Main apical trunk; 2: dendritic bifurcation; 3: spines. *Modified from: (Rozsa et al. 2007).* B) Different synaptic specializations of dendrites. *Modified from: (Stuart et al. 2007)*

Together, the dendrites form the dendritic arbor of neurons, which can be extremely diverse, ranging from the lack of dendrites in dorsal root ganglion cells to the extremely arborized cerebellar Purkinje cells.

IV.3.2. Dendritic Physiology

When describing the functional characteristics of dendrites, there are multiple aspects to be taken into consideration, such as the mere shape of the dendrite or dendritic structure, the membrane surface it provides, the synapses it contains and the ion channels that take an active part in the arising excitation or inhibition of the neuron. I will go through these issues in the following paragraphs.

IV.3.2.1 Passive Dendrites

Dendrites can be considered as cytoplasmic tubes with a certain diameter, covered by a phospholipid bilayer. In this way, their electrical properties resemble that of a simple electric cable (Rall 1969a; Rall 1969b) – hence the name Cable Theory. The different parameters that affect signal propagation in such a cable are the internal axial resistance (R_i), the membrane capacitance (C_m) and the specific membrane resistivity (R_m).

In these early studies, Rall described the dendrites as neuronal integrative compartments that receive inputs and that pass signals towards the soma by simple signal addition in case of multiple, synchronized afferent inputs. This type of signal processing is called linear summation. Here, the net effect of local inhibition and excitation provides the needed signal for driving the neurons to a depolarized state, meaning that whenever excitatory inputs overcome the inhibitory ones, the cell gets more depolarized. The only parameters affecting signal propagation to the soma are R_i , R_m and C_m , along with the morphology of the dendrites. Bifurcations are taken into account only as a decrease or increase in these factors, and no active ion channel contribution is considered.

The study on the morphology of dendrites quickly showed that the distance-dependent change in dendritic shape or width has disadvantageous effects on the propagation of signals towards the soma. As a result of the leaking synaptic current (low R_i) and the attenuating effect of C_m acting as a low-pass filter, the more distal the input is from the soma, the lower the amplitude and the slower the rise time will be. The attenuation of the signals traveling towards the soma is even more aggravated by the distance-dependent tapering of the dendrites that favors signals propagating from the soma. All in all, the passive characteristics can heavily reduce dendritic inputs arriving to the soma in many neuronal types including neocortical pyramidal neurons (Stuart and Spruston 1998), Purkinje cells (Vetter et al. 2001) just as in hippocampal interneurons (Emri et al. 2001), reaching up to a 100-fold decrease (**Fig. 5**) (Gulledge et al. 2005).

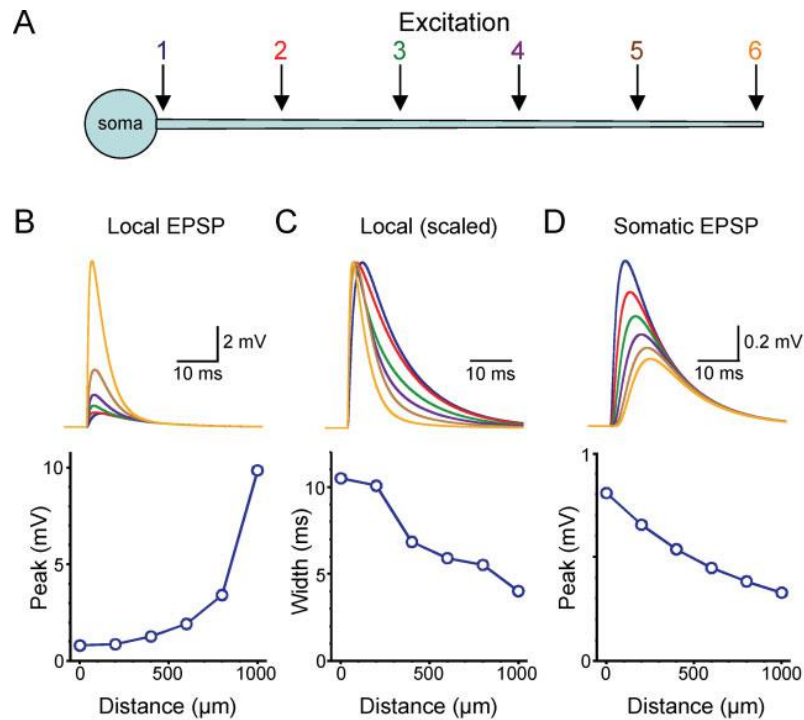


Figure 5 – Passive dendritic properties and synaptic signal propagation.

A) Schematic of a passive model neuron [50- μm diameter soma with 1000- μm tapering dendrite (5 μm – 1 μm); $R_m = 10,000 \Omega\text{cm}^2$; $C_m = 1 \mu\text{F}/\text{cm}^2$; $R_i = 100 \Omega\text{cm}$] CA1 pyramidal neuron. Numbered arrows indicate the location of excitatory inputs ($\tau_{\text{rise}}=0.2$ ms, $\tau_{\text{decay}}=2$ ms). **B)** Local voltage responses (*top*) to EPSPs (1 nS) generated at each of six locations shown in (**A**), and a summary plot of the relationship between local EPSP amplitude and the location of the synapse (*bottom*). **C)** Local EPSPs scaled to show changes in kinetics with distance from the soma (*top*) and plot of response half-width with distance from the soma (*bottom*). **D)** As in (**B**), but showing the somatic response (*top*) and amplitude (*bottom*) for EPSPs generated at locations shown in (**A**). *Source:* (Gulledge *et al.* 2005)

Though passive cable properties suggest a high level of attenuation, *in vitro* measurements showed that synapses can compensate for the loss by the mechanism named ‘synaptic scaling’ (Magee and Cook 2000; London and Segev 2001). The scaling effect can arise from AMPA receptor density increasing approximately twofold (from ~500 receptors per synapse to ~1000) when proximal and distal synapses were compared (Magee and Cook 2000; Andrasfalvy *et al.* 2003; Smith *et al.* 2003). On the

other hand, no such scaling is present in neocortical layer 5 neurons or possibly under *in vivo* conditions (London and Segev 2001; Williams and Stuart 2002; Nevian et al. 2007). Furthermore, the synaptic scaling cannot fully compensate for unlimited distances.

The relevance of passive electrical properties and Cable Theory can easily be realized, as they serve as the backbone for electrical signaling in neurons. Nevertheless, if there were only these parameters, the dendrites would serve as mere “antennae” of the neurons, with their parameters fixed and this would rule out any further processing capability, thus reducing the higher information processing capability of neurons to the somata and axon hillock of neurons.

IV.3.2.2 Active Neuronal Processes

The dendritic processes might serve simply as electric cables serving the conduction of input signals towards the soma, where these signals are to be summed and the output produced, as considered for many years (Eccles 1964; Kandel et al. 1977). Nevertheless, it has long been proposed that this is not the case, since besides the passive membrane properties, many active characteristics are present on the dendrites. Notably, the presence of voltage-gated ion channels on dendrites can aid the active amplification of the conducted signals. Evidence on the active backpropagation of action potentials into the dendritic tree suggested a major role for voltage-gated calcium channels (VGCCs) (Stuart and Sakmann 1994), sodium channels and N-methyl-D-aspartate receptors (NMDA-R) (Stuart et al. 1997). It has also been shown that the amplification of backpropagating action potentials (bAPs) is different with the increase of distance from the soma (**Fig. 6**) (Magee and Johnston 1997; Bernard and Johnston 2003). Furthermore, the range of the backpropagation of action potentials itself has been shown to rely mostly on the density of voltage-gated ion channels, particularly to voltage-gated sodium and potassium channels, besides the local characteristics of dendritic branching (Golding et al. 2001). The role of HCN channels is also suggested, as these tune dendritic resonance characteristics (Narayanan and Johnston 2007; Hu et al. 2009; Gastrein et al. 2011) and take part in the signal modulation by attenuating the propagation of signals along the dendrites (Nolan et al. 2004; Golding et al. 2005).

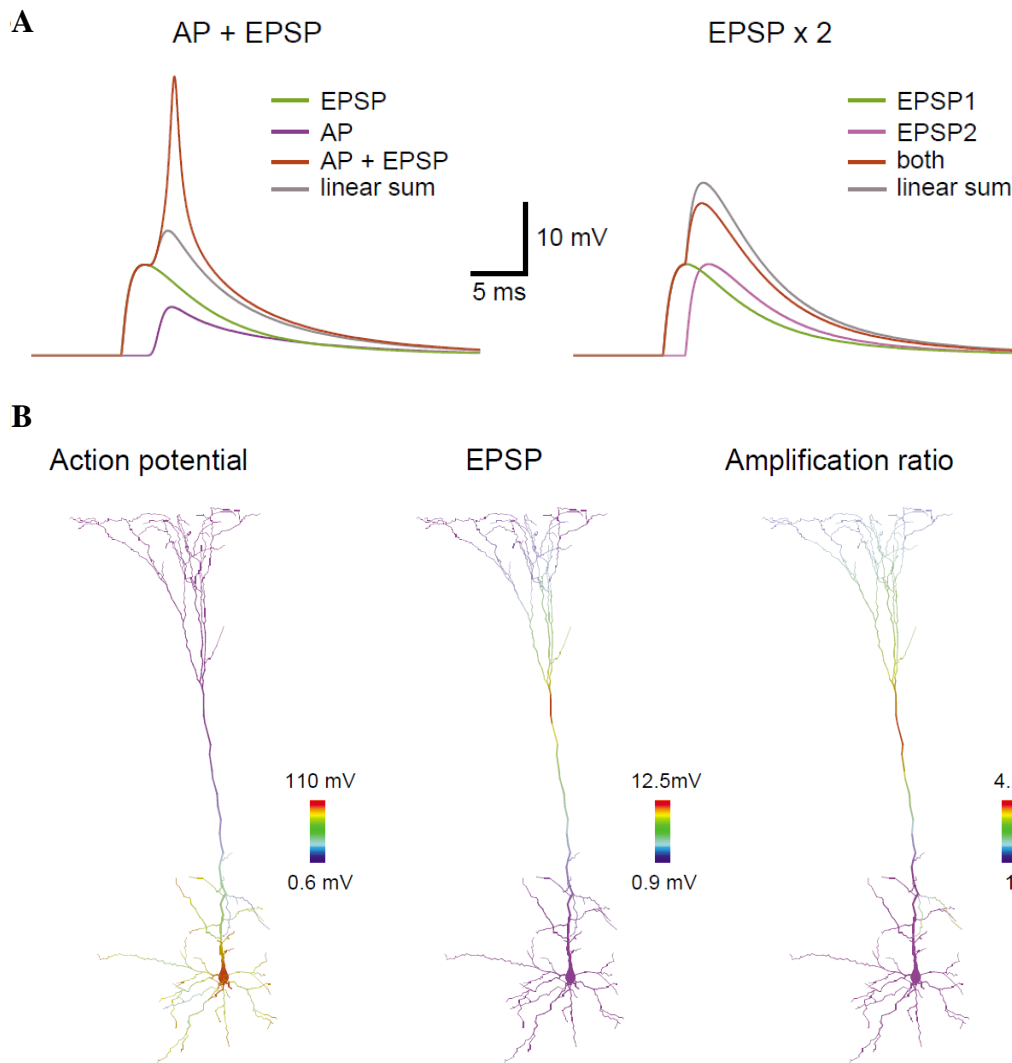


Figure 6 – Simulations on action potential amplification.

A) *Left*, superimposed sweeps of an action potential, an AMPA EPSP at optimum timing for action potential amplification (10.2 nS, -2 ms delay), the combined action potential plus EPSP response and their linear sum. *Right*, superimposed sweeps where the action potential was replaced by a second EPSP (10.2 nS, -2 ms delay). Recorded at the site of the synaptic input 583 μm from the soma in a compartmental model of a neocortical layer 5 pyramidal neuron. **B)** The peak voltage reached at different dendritic locations coded by color during a backpropagating action potential (*left*) and an AMPA EPSP (*middle*; 10.2 nS; 583 μm) in the same compartmental model as in **(A)**. *Right*, spatial distribution of action potential amplification when the action potential is paired with the EPSP (expressed as a ratio relative to control). The length of the color bar corresponds to 135 μm . *Source: (Stuart and Hausser 2001)*

IV.3.3. Dendritic Signal Integration

Synaptic signal integration has long been proposed as being a key component in how neurons compute in the neuronal network. The inputs arriving onto the dendritic 'antenna' may or may not reach the soma, with the levels of signal attenuation depending on the morphology of the dendritic arbor and the density of the various voltage-gated ion channels (Bernard and Johnston 2003; Golding et al. 2005; Barth et al. 2008; Katz et al. 2009; Larkum et al. 2009). The signals arising from distant, weak synapses are most likely filtered out when travelling towards the soma – but is there a mechanism to prevent that? Morphological characteristics of pyramidal cells pointed to the role of dendritic spines in integrating afferent excitatory inputs and backpropagating action potentials (Yuste and Denk 1995), using focal electrical stimulation and two-photon imaging. The somatic current injection combined with synaptic stimulation resulted in supralinear summation of calcium responses, suggesting that this phenomenon can serve as a means for synaptic plasticity. Similar studies were conducted on the combined role of synaptic responses and backpropagating action potentials in interneurons, where not only dendritic spines, but dendritic shafts were also examined, and both sublinearly and supralinearly integrating dendrites were found in this respect (Rozsa et al. 2004).

Many studies point to the possibility of synaptic signal enhancement when certain criteria are fulfilled (Schiller and Schiller 2001; London and Hausser 2005; Losonczy and Magee 2006). Firstly, though single inputs can also be amplified, in most cases a number of inputs must be active synchronously to overstep the linear summation regime and observe amplified signals. In pyramidal cells, around 6 synchronously activated spines are needed for supralinear signals. If the inputs are activated even mildly asynchronously, with 1 ms between the single synapse activations, then the summation of signals will remain at the simple arithmetic sum of single inputs (Losonczy and Magee 2006).

However, pyramidal neurons provide an anatomical compartmentalization for the ionic influx – the dendritic spine –, which is missing in many interneuron types (Losonczy et al. 2008; Spruston 2008; Makara et al. 2009). Evidence for the functional compartmentalization of responses (Goldberg et al. 2003a; Goldberg et al. 2003b; Rozsa et al. 2004) in interneuron dendrites gave the possibility of similar integrational

properties to appear locally as in pyramidal neurons. Two recent studies explored how different pathway-driven inputs show temporal summation in CA3 interneurons (Calixto et al. 2008; Cosgrove et al. 2010), but the methods used provided no direct spatial information on the exact location of the stimulated inputs.

More recently, the thin dendrites of cerebellar interneurons were shown to summate inputs sublinearly (Abrahamsson et al. 2012; Vervaeke et al. 2012). The sublinearity of the signals was attributed to their low diameter and passive characteristics.

IV.3.4. Dendritic Spikes

As previously described, dendritic signal integration can either be linear with passive propagation (Rall et al. 1966; Abrahamsson et al. 2012; Vervaeke et al. 2012) or can provide a signal amplification mechanism (**Fig. 7**) (Stuart and Sakmann 1994; Yuste and Denk 1995; Stuart and Hausser 2001; Rozsa et al. 2004; London and Hausser 2005; Larkum et al. 2009). Though it is widely accepted that the action potential – the final output of the cell – is the most important means in how dendritic integration affects the state of the neuronal network, it is well-established that not only backpropagating action potentials serve as a basis for modifying input relevance. One has to take into account the different ion channels that are locally present on the dendrites near the input sites and their effect on those synaptic events that do not lead to the firing of the cell. Theoretically, the arrival of multiple inputs to the same dendritic segment can increase the local membrane potential to above the threshold levels for the locally present, voltage-dependent ion channels.

The types of different dendritic spikes have been defined according to the major determinants in their occurrence – the channels that take part in their appearance such as VGCCs (Llinas and Sugimori 1980b; Larkum et al. 1999b; Waters et al. 2003; Byrne 2008; Larkum et al. 2009) or voltage-sensitive sodium channels (Ariav et al. 2003; Magee and Johnston 2005; Losonczy and Magee 2006; Gomez Gonzalez et al. 2011). Furthermore, local activation of NMDA-receptors can also be observed (**Fig. 7**) (Schiller et al. 1997; Schiller et al. 2000; Schiller and Schiller 2001; Larkum et al. 2009; Antic et al. 2010). All of these events can show rather similar characteristics to that of the action potential, but without the involvement of the axon initial segment and its very

dense population of ion channels (Lorincz and Nusser 2008; Lorincz and Nusser 2010; Kole and Stuart 2012). These local regenerative events have been named dendritic spikes (Llinas et al. 1968; Golding et al. 1999; Gasparini et al. 2004). Namely, dendritic spikes can be Sodium spikes, Calcium spikes or NMDA spikes.

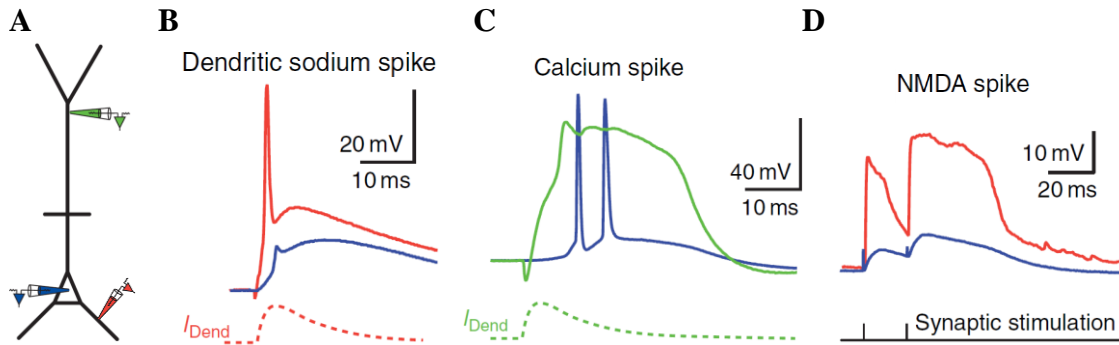


Figure 7 – Amplification of dendritic responses.

A) Different types of action potentials observed in dendrites of neocortical pyramidal neurons. Electrodes schematically indicate the site of recordings from neocortical pyramidal neurons at the soma (*blue*), distal apical dendrite (*green*), or basal dendrites (*red*). Membrane voltage recordings in corresponding colors. **B)** Sodium spikes can be elicited locally in both apical and (as shown here) basal dendrites. **C)** Apical dendrites of layer 5 pyramidal neurons can generate Calcium spikes mediated by VGCCs (evoked by local dendritic depolarization). **D)** Strong synaptic activation can result in the initiation of an NMDA spike. *Sources: adapted from (Byrne 2008), using (Larkum et al. 1999a; Waters et al. 2003; Nevian et al. 2007)*

IV.3.4.1 Dendritic Sodium Spikes

As implied by their name, these local dendritic regenerative events are mainly fueled by the voltage-gated sodium channels present locally on the dendrites. Many signs pointed to the active involvement of these channels located on the dendrites, mostly revealing themselves in the fast prepotentials that preceded the somatic action potentials (Spencer and Kandel 1961; Turner et al. 1993). When examining the basal dendrites of neocortical pyramidal cells using glutamate puffs and focal synaptic stimulation, a response showing quick rise times and fast decay constants both on

somatic electrophysiological recordings and dendritic voltage imaging could be detected dubbed a 'spikelet', which was highly sensitive to the voltage-gated Sodium channel blocker tetrodotoxin (TTX) (Milojkovic et al. 2005b). Using two-photon glutamate uncaging on CA1 pyramidal cell oblique dendrites, the evoked synaptic response showed a similar fast rise time and the appearance of a spikelet (**Fig. 8**) when recorded somatically, sitting on top of the conventional, fast AMPA-receptor mediated excitatory responses.

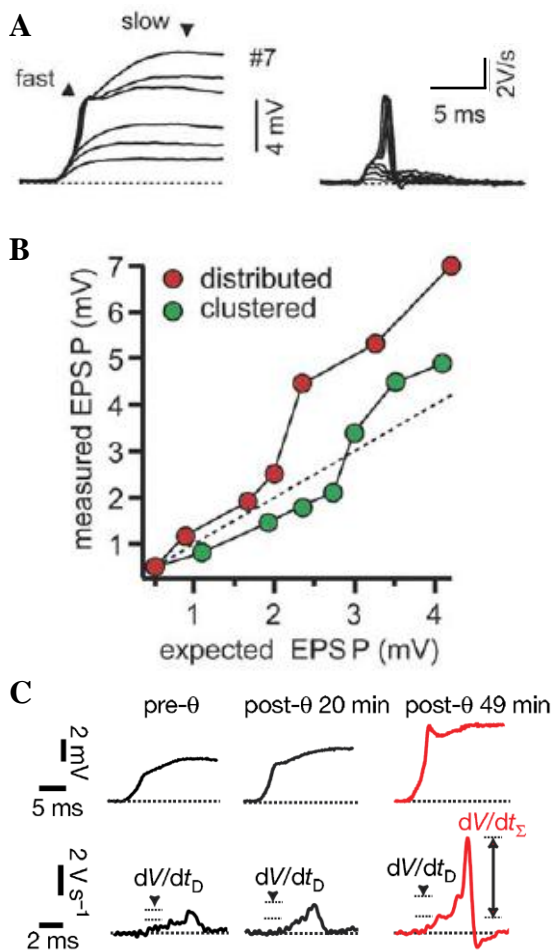


Figure 8 – Dendritic Sodium spikes.

A) Somatically recorded current responses (*left*) to glutamate uncaging at 7 dendritic spines simultaneously on CA1 pyramidal cells caused a sudden jump in the response, as shown by the derivatives of signals (*right*). **B**) The input-output curve of the responses clearly shows a deviation from the linear towards the supralinear summation for both distributed or clustered input patterns on CA1 pyramidal cells. **C**) Theta-burst stimulation LTP protocol leads to the appearance of local Sodium spikelets. Sources: A-B) (Losonczy and Magee 2006); C) (Losonczy et al. 2008)

The number of synchronously activated synaptic inputs that resulted in the appearance of a dendritic Sodium spike was found to be ~ 6 (Poirazi et al. 2003a; Losonczy and Magee 2006), and the spikelet could be blocked by TTX (Losonczy and Magee 2006). The elevated membrane potentials can lead to the relief of the Magnesium block in NMDA-receptors, thus causing the Na-spike to turn into an NMDA-spike in case of CA1 pyramidal neurons (Losonczy and Magee 2006), though

in this case the voltage-gated calcium channels do not play a significant role in shaping the response, possibly as a result of their lower density on pyramidal cell oblique dendrites (Losonczy and Magee 2006).

The functional significance of dendritic Sodium spikes has been suggested in some instances. Firstly, Na-spikes can have a role in long-term potentiation (LTP) of synaptic inputs, since these events can cause potentially weak synapses to be strengthened by repeated stimuli (Markram et al. 1997; Bi and Poo 1998). Namely, it has been shown that the branches of hippocampal CA1 pyramidal neurons that showed linear summation produced dendritic Sodium spikes after a well-known protocol for evoking synaptic long-term potentiation, the theta-burst protocol (Losonczy et al. 2008). Another example is that dendritic Sodium spikes help in lowering the threshold of action potentials, thus making a cell either more active under normal conditions or pulling the neurons out of hyperpolarization caused by inhibition (Crochet et al. 2004).

IV.3.4.2 Dendritic Calcium Spikes

Voltage-gated calcium channels have long been implied in local synaptic responses on dendrites, but their active role in creating local regenerative events has only been discovered recently. One of the first descriptions of dendritic Calcium spikes was in alligator Purkinje cell dendrites (Llinas et al. 1968). Further on, studies on avian and mammalian Purkinje cells clearly stated that the recorded intradendritic regenerative events showed no TTX sensitivity (Llinas and Hess 1976; Llinas and Sugimori 1980a). In contrast, the events were blocked by the VGCC-blockers Cd^{2+} , Co^{2+} , Mn^{2+} , or by the removal of extracellular Calcium (Llinas and Sugimori 1980b). Furthermore, these dendritic action potentials have since also been described in neocortical pyramidal neurons both *in vitro* (Schiller et al. 1997; Larkum et al. 1999a) and *in vivo* (Kamondi et al. 1998; Helmchen et al. 1999; Svoboda et al. 1999; Larkum and Zhu 2002).

Dendritic calcium spikes usually appear in the form of multiple events locally (**Fig. 9**), and can take up two different forms. There are fast, burst-like events that follow short synaptic events that reach high enough amplitudes to exceed the threshold for VGCC activation, but decay swiftly, lacking further upkeep of activation. On the other hand, longer depolarization at the dendrite leads to Calcium plateau potentials that

start with the short, burst-like events and keep the dendrite at a hypopolarized state for a longer period, and might be fuelled by prolonged synaptic activation (**Fig. 9**) (Golding et al. 1999; Crochet et al. 2004). Due to their lower rise time and slower decay time, they can override the passive propagation properties of dendrites, travelling below the low-pass filtering threshold. Thus, they have been shown to provide a boost to firing frequency, but in a distance-dependent manner, showing less and less amplificative effects with the Calcium spike initiation zone moving away from the soma (Oakley et al. 2001a; Oakley et al. 2001b). Although dendritic calcium spikes were proven to play a lesser role in the generation of somatic complex spikes in Purkinje cells (Davie et al. 2008), there is experimental evidence that they can drive bursts of Sodium action potentials at the soma (Golding et al. 1999).

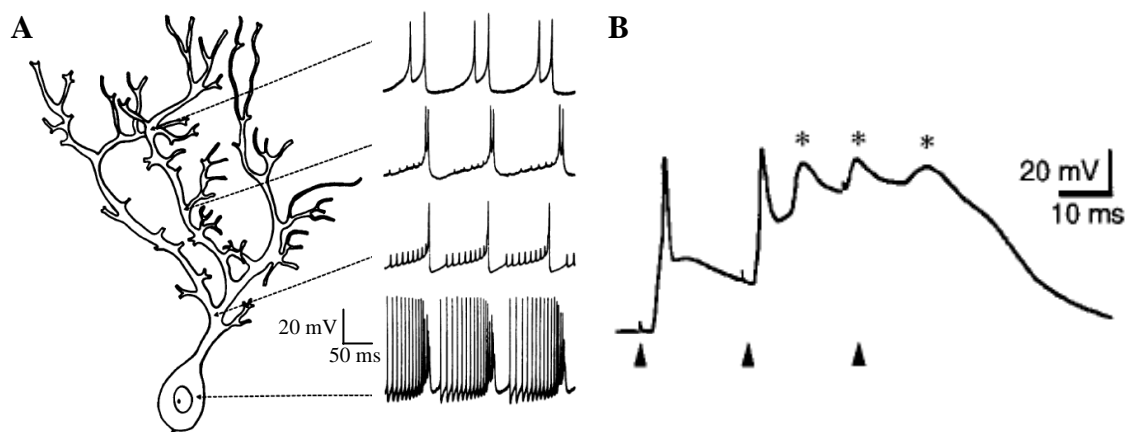


Figure 9 – Dendritic Calcium spikes.

A) Calcium spikes in Purkinje cells (*left*) unmasked with the increasing distance from soma after somatic action potential induction (*bottom right* is somatic, *top right* is farthest dendritic recording). **B)** Pyramidal cell dendritic responses to synaptic stimulation show the short and plateau form of dendritic Calcium spikes. *Sources: A) (Llinas and Sugimori 1980a); B) (Golding et al. 1999)*

Experimental evidence exists for the functional relevance of dendritic calcium spikes for both the synaptic or network point of view (Kamondi et al. 1998; Golding et al. 2002; Gullledge et al. 2005). On the level of the synapses, local Calcium spikes have been shown to induce LTP on pyramidal cells (Golding et al. 2002). As for their effect

on the network, these can be easily derived from their impact on somatic action potential firing (Golding et al. 1999). The role dendritic Calcium spikes play in network function has been demonstrated by the *in vivo* recording of dendritic Calcium spikes on pyramidal cells during sharp-wave oscillations in the hippocampus (Kamondi et al. 1998), which suggests a major role for dSpikes for modifying oscillative network activity by local processing.

IV.3.4.3 Dendritic NMDA Spikes

The third type of local regenerative activity is driven by NMDA-receptors (Antic et al. 2010). NMDA receptors are heterotetrameric ligand-gated ion channels that are activated by glutamate and the co-activator glycine, where the activation leads to opening on the pore that is selective for cations, resulting in the influx of Sodium and Calcium ions and efflux of Potassium ions (Purves 2008). The activation is blocked by Magnesium ions, and the relief of Mg-block is linked to the increase in membrane voltage (Nowak et al. 1984; Jahr and Stevens 1990). Hence, the NMDA-receptor functions as a voltage-gated ion channel, particularly when considering the increase of Calcium influx, which is almost none with the Mg block in place (Goldberg et al. 2003b).

Both dendritic Sodium and Calcium spikes are triggered by the increase in the local membrane voltage above the activation threshold of voltage-gated Sodium channels and VGCCs, respectively (Larkum and Zhu 2002; Losonczy and Magee 2006; Hao and Oertner 2011). Since they are not ligand-gated ion channels, their own ionic influx can help to sustain the increased membrane potential and can aide their propagation along the dendritic arbor. On the other hand, since NMDA spikes are ligand-gated ion channels, without their ligand, they are not activated. As a consequence, the action of these receptors stays localized without any further help from other ion channels to and around the synaptic sites, where the glutamate concentration is high enough for their activation. Nevertheless, the propagation of NMDA spikes is less hindered by the passive properties of dendrites, as NMDA-spikes are slow-rising plateau potentials, which partly overcome the low-pass filtering effect of the dendritic membrane (**Fig. 10**) (Schiller et al. 2000; Schiller and Schiller 2001; Antic et al. 2010). Furthermore, the spatial limits for NMDA spikes can be extended beyond the activated cluster of synapses by glutamate spillover (Chalifoux and Carter 2011).

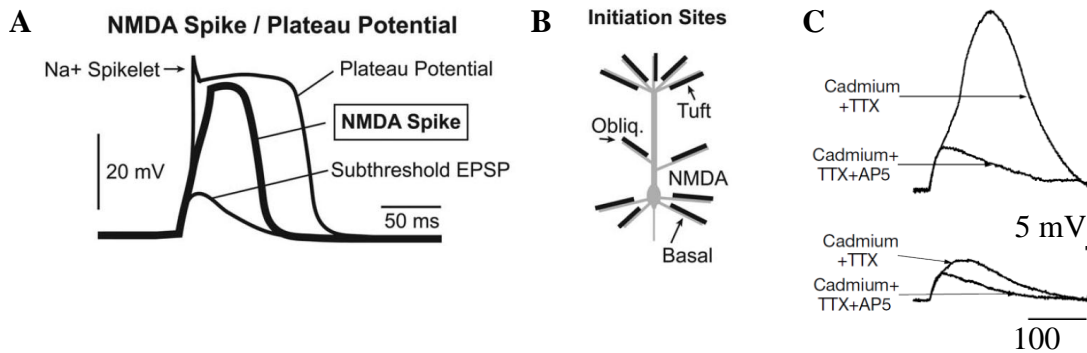


Figure 10 – Dendritic NMDA spikes.

The voltage trace (**A**) and initiation sites (**B**) of NMDA spikes in pyramidal cell thin dendrites. **C**) Glutamate uncaging evoked basal dendritic responses show a ‘pure’ NMDA spike that is unaffected by NaV or VGCC-blockage. *Sources: A-B* (Antic et al. 2010); *C* (Schiller et al. 2000)

The physiological properties of NMDA-spikes include the glutamate threshold that might be one of the limiting factors why mostly thin dendrites of pyramidal cells display NMDA spikes, and that they are not present on the thick apical dendrites (Schiller et al. 2000; Schiller and Schiller 2001). The lower membrane surface of these thin branches along with the same number of NMDA-receptors (NMDARs) that are present on the membrane surface translates to a higher relative density of NMDARs, which in turn yields higher synaptic responses and easier unblocking of the receptors pore. Previous studies proved that a glutamate concentration of $\leq 1\text{mM}$ is sufficient to evoke dendritic NMDA-spikes on basal dendrites (Schiller et al. 2000; Schiller and Schiller 2001; Antic et al. 2010).

Another important characteristic of NMDA-spikes is its ionic composition, as under physiological conditions, NMDARs are activated after AMPA-receptors, along with voltage-gated Sodium and Calcium channels, thus producing a local complex spike (**Fig. 10B**) (Schiller et al. 2000). When taking into account the timing of different ionic fluxes during this complex spike, the delay of the NMDAR-evoked response might suggest that NMDA-spikes require the preceding activation of either AMPA-receptors or voltage-gated Sodium channels to reach their threshold. Nevertheless, experimental data show that dendritic Sodium spikes are not a necessary requirement for NMDA spike initiation, since blocking voltage-gated Sodium channels did not affect the

initiation of plateau potentials (Milojkovic et al. 2005a; Major et al. 2008; Antic et al. 2010), and many dendrites lack the Sodium channel density to support a dendritic Sodium spike that might be serving as a trigger for NMDA spikes (Nevian et al. 2007). In addition, a threshold of ~8–10 nS NMDA conductance concentrated within a 25 μm dendritic region is required, but AMPA synaptic input is not necessary for the production of simulated NMDA spikes (Rhodes 2006).

Dendritic NMDA spikes play a role in the functioning brain on the computational level, affecting dendritic integration. The summation of inputs raises the Calcium influx by NMDA spikes, which in turn helps the local synaptic plasticity processes to take place, driving both long-term and short-term plasticity or modifying intracellular signaling cascades (Golding et al. 2002; Holthoff et al. 2004; Gordon et al. 2006; Remy and Spruston 2007). The 20-50 μm spatial extent of the NMDA-spikes along a single dendritic branch that can reach even 100 μm suggests that multiple, dynamic functional subunits might exist within one dendritic branch (Branco and Hausser 2011). Nevertheless, the activation of the same number of inputs in a clustered or a distributed fashion yielded similar results on hippocampal oblique dendrites, both evoking dendritic spikes, which supports the 'one branch – one computational subunit' hypothesis (Losonczy and Magee 2006; Branco and Hausser 2010).

IV.3.5. The Role of nAChRs in Active Dendritic Processes

Neuronal nicotinic acetylcholine receptors are ligand-gated cation transmembrane channels comprised of five subunits of types α , β , γ or δ either in a homomeric or heteromeric fashion (Dani and Bertrand 2007). The receptors contain a hydrophilic pore, which is surrounded by the subunits. Neuronal subunits that form nAChRs in $\alpha\beta$ combinations include $\alpha 2$ – $\alpha 6$ and $\beta 2$ – $\beta 4$. Not all subunits are capable of forming homomeric receptors, and the most common homomeric subunit composition in the mammalian neuronal tissue is built up from $\alpha 7$ subunits. The two acetylcholine binding sites are placed in between two adjacent subunits that form a ligand-binding pocket. Though composed of different subunits, nAChRs can take up three distinct functional states in response to an agonist: closed at rest, open pore, and closed desensitized. Brief exposure to high concentrations of the neurotransmitter,

acetylcholine (ACh), causes opening of the water-filled, cation-selective pore. After a couple of milliseconds, the receptor closes to a nonconducting state. Prolonged exposure to low concentrations of nicotine, as obtained from tobacco use, produces significant desensitization, which stabilizes the receptor in a closed state that is unresponsive to agonists (Dani et al. 2000).

Although much evidence indicates that nAChRs expressed in the hippocampus are involved in synaptic plasticity and cognitive function (Dani et al. 2001; McGehee 2002; Dani and Bertrand 2007), little is known about how this regulation occurs, particularly in brain regions known to be important for cognition. The $\alpha 7$ -nAChRs are ligand-gated cation channels with high permeability to Ca^{2+} (Castro and Albuquerque 1995; Khiroug et al. 2003; Fucile 2004; Fayuk and Yakel 2005), which is involved in a variety of signal transduction cascades. Although fast postsynaptic nAChR-mediated responses and a consequent nAChR-induced boosting of LTP induction were suggested in one study of pyramidal cells (Ji et al. 2001), many studies have been unable to demonstrate the rapid postsynaptic nAChR-mediated excitation in principal cells (Frazier et al. 1998; Khiroug et al. 2003). In our earlier study, we showed a timing-dependent facilitation of excitatory synaptic input-induced calcium transients in hippocampal interneurons (Vizi et al. 2004). These observations suggested a role for $\alpha 7$ -nAChRs in spike timing-dependent plasticity (Rozsa et al. 2008), which have been proven just recently (Gu and Yakel 2011).

IV.4. Two-Photon Microscopy for Neuroscience

Over the last twenty years, neuroscientists have become increasingly interested in two-photon microscopy. One of the reasons for this interest is that two-photon fluorescence excitation allows counterbalancing the deterioration of the optical signals due to light scattering, which opens the door for high resolution imaging at considerable depth in living tissue. Due to progress in fluorescent marking techniques, to-date, two-photon microscopy allows the functional exploration of neuronal activity at multiple scales, from the sub-processes of a single cell (dendrites, single spines...), through single cells or small networks of a few neurons, up to large neuronal populations in the order of a cortical column. This chapter is aimed to provide some information on the

practical aspects of two-photon microscopy applied to imaging neurons in living tissue, and to state the advantages, shortcomings and possible developments of the technique. Since my work involves high-speed imaging of 3D objects, particular attention is devoted to the introduction to z -axis scanning techniques.

IV.4.1. Introduction on Two-Photon Microscopy

Fluorescence microscopy has proven an essential tool for the examination of biological specimen, both fixed or alive (Yuste 2005). One of the reasons for its great success is that fluorescent objects can be selectively visualized at good signal-to-background ratio even at small fluorophore concentrations.

When applied to thick (over $\sim 100\ \mu\text{m}$) samples, conventional fluorescent microscopy suffers from the shortcoming that the fluorophore is excited in a comparatively large volume, giving rise to a large out-of-focus component in the fluorescence reaching the detector. Confocal microscopy (Conchello and Lichtman 2005) deals with this problem by using a pinhole to reject the photons originating from all locations other than from one point in the focal plane, providing an optical section of the sample. The focal plane is then scanned in 2 dimensions (x, y). The same procedure is repeated, serially, for each desired depth (z -dimension) until the relevant part of the biological specimen is covered. Subsequently, the imaged volume is visualized using three-dimensional reconstruction. It is important to realize that, although in confocal microscopy the out-of-focus photons do not contribute to the image, the corresponding molecules are still excited, leading to a high imaging cost in terms of photodamage and photobleaching. A partial solution to this problem consists in recording through many pinholes in parallel (e.g., using Nipkow disk-based approaches). There, the same sample location is visited multiple times, leading to a higher signal rate. This allows the lowering of laser powers used and finally leads to less photodamage and bleaching.

Another shortcoming, however, remains: detection through the pinhole(s) blocks not only the fluorescence originating from out-of-focus excitation, but also the photons that were indeed emitted from the in-focus-point, yet underwent scattering on their way out of the tissue. This loss of “good” photons further reduces the yield of the instruments. All of these problems are exacerbated by the strong light scattering of biological tissue, which makes high-resolution depth imaging impossible with conventional and confocal microscopy.

The application of two-photon excitation to biological microscopy can thus be considered as a true break-through in fluorescent microscopy depth-imaging. Several excellent reviews and books (Frostig 2009) of two-photon functional imaging, and calcium imaging in particular, can be found in the literature, which either focus on its technical aspects (Koester et al. 1999; Zipfel et al. 2003; Helmchen and Denk 2005; Göbel and Helmchen 2007), on its applications (Hubener and Bonhoeffer 2005; Garaschuk et al. 2006; Svoboda and Yasuda 2006; Kerr and Denk 2008), or on its place in the wider context of the various recent technological developments, which provide tools for a "reverse engineering" on the brain (O'Connor et al. 2009).

To introduce briefly the basic principles and advantages of two-photon microscopy over more conventional approaches, two-photon excitation occurs when two low-energy photons together excite a fluorescent molecule, which then decays back to its fundamental state by emission of a photon of somewhat lower energy than the sum of the two exciting ones. The theoretical grounds of two-photon absorption have been set already in 1931 by Maria Göppert-Mayer (Göppert-Mayer 1931). However, experimental confirmation had to wait until progress in laser technology in the 1960s that made ultra-short pulsed lasers available, which finally allowed the design of two-photon microscopes (Denk et al. 1990).

Why has two-photon microscopy become so popular over the last ten years or so?

First, living tissue scatters light less in the infrared than at visible wavelengths, which are typical of most common fluorophores upon single-photon excitation. It thus became possible to optically examine fluorescent objects within living specimen up to depths that were so far inaccessible (Flusberg et al. 2005; Helmchen and Denk 2005). These reach from typical depths of several hundreds of microns up to one millimeter (Theer et al. 2003)

Second, two photons must be absorbed simultaneously for excitation to occur. Therefore, the probability that a fluorescent molecule is excited depends quadratically on light intensity, rather than linearly as in the case of single photon fluorescence. In simple terms, significant excitation occurs only where the local concentration of photons is very high, which happens essentially only at the focal point of the microscope, even in the presence of scattering. Photobleaching and photodamage to the tissue are thus greatly reduced. Most important, no fluorescence is emitted from out-of-

focus locations resulting in “automatic” optical sectioning, without any need for out-of-focus rejection strategies like that implemented in confocal microscopy by the usage of one or more pinholes.

Finally, in two-photon microscopy all emitted fluorescence photons are useful – even the ones that were scattered on their way out of the tissue. Collecting them allows to dramatically increase signal-to-noise ratio (SNR) with respect to situations where the scattered photons are rejected, as in confocal microscopy. For the above reasons, two-photon excitation allows to selectively excite (or photochemically activate or inactivate) microscopic parts of a biological sample, at depths up to one millimeter and only at the in-focus plane, avoiding the photodamage and photobleaching that would result from a comparable excitation with confocal microscopy.

Overall, two-photon microscopy is thus a unique tool for imaging biological samples – *in vivo* in particular – in depth and for local photochemistry. However, its performance in imaging transparent or very thin specimen is worse than that of confocal or even wide field fluorescence microscopy, because the longer wavelengths used for imaging reduce the maximal achievable spatial resolution.

IV.4.2. Laser Light Sources

Instead of the continuous wave emitting lasers used for confocal microscopy, two-photon microscopy requires pulsed lasers. These are usually Ti:Sapphire lasers, which are pumped with a laser beam from an Argon or frequency-doubled Nd:YVO₄ laser and yield outputs of 1 W average power or more in the central part of their wavelength range. This power is usually enough, except for ultra-deep imaging (500 - 1200 μm), where the laser pulses have to be powered-up by regenerative amplification, at the expenses of pulse frequency, typically by a factor of 1000 (Theer et al. 2003). Nevertheless, an ultimate depth limit is imposed on imaging by the fluorescence generated at the surface of the sample by out-of-focus light, with a consequently worse localized excitation and a deterioration of contrast. In gray matter, this limit appears to be in the order of 1000 μm (Theer et al. 2003). In addition, one has to take into account that after excitation, the lower wavelength light emitted in deep tissue regions undergoes heavy scattering and absorption, which also degrades the resolution and SNR of deep imaging.

Pulse rates have to be such as to balance the fluorophore's excitation efficiency and onset of saturation. This criterion is met by the typical Ti:Sapphire pulse rates (~ 100 MHz) for most common molecules, which is fortunate because in mode-locked lasers pulse rate is difficult to change. Stable excitation rate being an important consideration, it is essential that a constant number of pulses arrives on a pixel. Assuming a typical pulse rate of 100 MHz and a typical dwell time of 1 μ s, more than 100 pulses arrive on a pixel. The number of pulses per pixel will thus be stable at the 1% level.

The optimal pulse length is more difficult to define. The optical components in the excitation path cause dispersion, pulses reaching the sample are thus broadened ("chirped") with respect to their initial duration. Indeed, in an optical medium the propagation speed of electromagnetic radiation depends on wavelength, and this effect is stronger for short pulses (typically around or below 100 fs) than for long ones. Being constant and known for a given microscope's excitation path, such dispersive broadening can be pre-compensated by "negatively dispersing" the pulses. These "pre-chirped" pulses are thus restored to short ones when exiting the objective, which maximizes two-photon absorption at the sample level. Although this procedure is relatively easy to implement, the added optical components unavoidably result in some power loss one has to take account of.

IV.4.3. Scanning Methods (x - y plane)

Once the desired pulse duration has been set and power of the laser beam into the excitation path has been adjusted (usually with the help of a Pockels cell), the beam has to be scanned through the sample. The most common solution to do this is to use mirrors moved by galvanometers, which allow rapid, arbitrary positioning of the focus in the focal plane (x - y). When used in raster scanning application, galvanometric mirrors not only have excellent optical properties, but also allow zooming and image rotation. However, such applications are limited to the study of relatively slow phenomena, because of their limited speed (~ 1 ms per line at best, resulting in a typical frame duration of ~1 s). Speed can be increased at the cost of the resolution and the area covered, but still a large portion of the scanning is wasted on measuring the background part, *i.e.*, the non-interesting regions of the image.

There are raster scanning methods for *in vivo* imaging that are intrinsically faster. For example, the scanning speed along the critical of the two in-plane dimensions can be increased using the resonant galvanometer technology (Fan et al. 1999; Nguyen et al. 2001). In rapid raster scanning, the whole x - y plane is scanned, yielding images of excellent quality.

A classical alternative to scanning the whole plane is the so-called “line scan”. Here, the laser beam is scanned by the galvanometer-based mirrors along a line placed by the user on top of the structure of interest, rather than across the whole 2D plane. High speeds can be reached in this way; for instance, multiple nearby dendritic spines can be visited in less than 1 ms (Lorincz et al. 2007). On the other hand, the increase in scanning speed for a given region of interest (ROI) happens at the expense of spatial information, since spatial information is collected only from a single line. Also, selection and adjustment of the scanning trajectories should be made efficiently within the time of the experiment, which can be quite cumbersome because in most systems the structure of interest has to be a straight line (e.g., a dendritic spine, an “adequate” dendritic segment, etc.). Moreover, measurement speed usually cannot be controlled. Therefore, precious measurement time is wasted, because the extracellular space of no interest between ROIs is swept over at the same speed as the ROIs themselves. This can be circumvented by jump commands where mirrors are driven to maximal scanning speeds in between ROIs to cross areas of no interest.

Similarly to x - y scanning, line-scanning also becomes increasingly wasteful when the structures of interest are sparsely distributed. Indeed, galvanometer-based approaches are still mechanical systems, where the speed of scanning is limited by the acceleration/deceleration rates of the motors. Most important, all the structures to be scanned have to lie in the focal plane (lines can be scanned only at constant z value), with the exception of three-dimensional approaches (see sections below). As a final consideration, line-scans – and in general, all ROI scanning methods – need extensive software support, which is not always provided by microscope manufacturers.

Instead of continuously scanning along a plane or a line, novel random-access scanning methods follow a different concept: the focused laser beam is directed selectively to predetermined targets (points). Therefore, this approach is of interest when the ROIs are sparsely distributed within the sample. There, scanning the whole x - y

plane as done in raster scanning is not only inefficient in terms of time, but also counterproductive because of useless fluorophore excitation outside the ROI and consequent bleaching and photodamage. Although this is possible using galvanometric mirror technology, speeds reach at best ~ 0.2 ms/point because of mechanical inertia. A valid alternative consists in using acousto-optic devices to direct the laser beam.

An acousto-optic deflector is a transparent crystal, within which an optical grating is created by sound waves. The frequency of the sound wave determines the spacing of the grating, and thus the angle of diffraction of the laser beam on this grating. In this way the laser beam can be diverted without mechanical movements, allowing positioning speeds that are orders of magnitude faster than those obtainable with galvanometric mirrors. However, the involved optical materials are highly dispersive, leading to substantial temporal and angular dispersion, which, for typical pulse durations (< 1 ps) deteriorates the excitation efficiency and point spread function (Iyer et al. 2006) and thus image quality. Compensations are possible using gratings, prisms and/or additional acousto-optic devices (Ngoi et al. 2001; Lechleiter et al. 2002; Iyer et al. 2003). In addition, acousto-optic deflectors have also been proposed (Reddy and Saggau 2005) for tackling scanning also along the z axis, which has only recently been more fully explored (Göbel et al. 2007; Duemani Reddy et al. 2008; Kirkby et al. 2010; Grewe et al. 2011).

IV.4.4. Objectives

The objective generates the laser focus required for localization of excitation and is therefore a critical element of the microscope. A large choice of objectives suitable for two-photon microscopy can be found on the market. Important criteria for a choice include: (i) the numerical aperture, which has to be large because it determines resolution and the collection angle for fluorescence; (ii) the magnification, which has to be chosen according to the desired field of view; (iii) the working distance, which has to be relatively large, especially in *in vivo* applications, where several media have to be stacked between the objective and the sample (coverglass, agarose...); and (iv) a good transmission efficiency in the near-infrared and visible wavelengths.

Before impinging onto the sample, the beam is expanded to “fill” the back aperture of the microscope objective, which finally focuses the light into the sample. Since the radial intensity profile of a laser beam is Gaussian, the question arises of what

an optimal filling is. A laser beam is said to “overfill” the back aperture of the objective when the latter accepts the central part of the beam up to the radius R at which its intensity decays to 13.7% ($1/e^2$). In this case, 84% of the beam’s power is transmitted and lateral and axial resolution (Zipfel et al. 2003) are nearly as good as with a uniform excitation beam (92 and 96%, respectively). Underfilling the objective using a narrower beam increases the amount of power transmitted by the objective, but results in a reduced effective numerical aperture (NA) and thus in a loss of resolution (for more details including calculations, see (Zipfel et al. 2003; Helmchen and Denk 2005)). However, it has to be considered that with increasing depth the effective NA is reduced: large angle photons travel considerable longer distances in the tissue than photons near to the optical axis and are thus more likely to be scattered away or to be absorbed (e.g. by surface blood vessels). Depending on the application, underfilling the objective might thus be the way to go, in particular, if the objects to be observed are comparatively large and their detectability does not suffer under the slightly reduced accuracy. Indeed, as the size of the focal volume grows with decreasing effective NA, the peak intensity therein decreases, thus decreasing photobleaching and photodamage.

IV.4.5. Detectors

In two-photon microscopy, optical sectioning is achieved by spatially ultra-selective excitation. Therefore, all photons emitted by the excited fluorescent molecules are useful and should thus be collected, including scattered ones. As mentioned above, fluorescence has shorter wavelengths than excitation light, therefore it is more heavily scattered and beyond depths of a few 100 μm , the amount of ballistic photons emerging from the sample is negligible. Therefore, large numerical aperture and low-magnification objectives (e.g. 20x at a NA of 1.0) are preferable to capture as many photons as possible and large sensitive area photomultipliers (PMTs – a performance comparison between different types can be found in (Zipfel et al. 2003)) are disposed in an arrangement that allows to detect as much of them as possible, either scattered in the forward direction (“trans”- collection geometry) or backwards (“epi”- collection geometry). For *in vivo* imaging, samples can in most cases be considered semi-infinite thus impeding trans-collection, which makes an efficient epi-detection particularly important. Of most common use is the so-called “whole-area” configuration, where the back of the objective is projected onto the PMT’s sensitive area and thus allows all

photons collected by the objective to end up on a detector preferably placed as close as possible to the objective. Importantly, new approaches emerge for *in vivo* applications, using mirrors to collect the light that does not even enter the objective (Combs et al. 2011).

IV.4.6. Three-Dimensional Imaging by Fast Objective Movement

Ideally, one would like to investigate physiological functions at high spatial and temporal resolution in many arbitrary 3D positions, simultaneously. For example, simultaneous (that is, millisecond-near) measurement of hundreds of neurons (somata and/or processes) are required in order to understand the functioning of even a small patch of cortex, hippocampus or any other brain structure. Even at the single neuron level, in order to find and image individual local dendritic spikes at high temporal and spatial resolution, one needs to acquire hundreds of pixels every few milliseconds from the same dendritic segment, over at least several tens of micrometers z -scanning range.

One of the main limitations of “classical” laser scanning microscopy is the sequentiality of scanning in 3D, which is essentially limited to so-called “3D stacks”. Here, xy planes are scanned for different z positions, which is time-consuming. Whereas this procedure allows obtaining quite complete 3D information for anatomical (structural) imaging, the long collection times (seconds to minutes) are unfeasible for functional imaging. Recently, the development of methods for 3D functional imaging that overcome this limitation, using galvanometric mirror scanning in the xy plane combined with axial scanning relying on a piezoelectric actuator has been reported (Göbel et al. 2007). As it involves the objective being moved up and down in a sinusoidal fashion ($z(t)$ -movement), mechanical inertia is a major constraint on the possible spatiotemporal trajectories of the focal point within the sample. Although performance is ideally optimized by defining such 3D trajectories case-by-case, depending on the particular spatial distribution of points of interest, in practice, stereotypical movements sampling the whole 3D volume are often preferable (e.g., spirals). For instance, when imaging neuronal populations, (Göbel et al. 2007) showed that 90% of the neurons in volumes up to $250 \mu\text{m}^3$ could be imaged with acquisition rates on the order of 10 Hz, using either a spiral-like or a custom, user-defined trajectory.

An intrinsic limitation of the above approach is the mechanical weight of the objective – this limits high-speed measurements to a small z-range. Furthermore, at higher speeds, the vibration from physical movement of the objective lens can easily disturb image quality and disrupt biological samples.

IV.4.7. Three-Dimensional Imaging by Acousto-Optic Scanning

To overcome the limitations of piezo-driven z-scanning, such as the constraints imposed by only few available mechanical resonances and the small z-scanning ranges obtainable at high scanning speeds, it is advantageous to scan without mechanically moving parts. In this perspective, acousto- and electro-optical scanning open new horizons for rapid scanning along the z axis at 400kHz (Kaplan et al. 2001), tens of kHz (Reddy and Saggau 2005) or at several kHz (Duemani Reddy et al. 2008). Three dimensional scanning can be achieved by changing incident laser light divergence using four deflectors generating two cylindrical lenses (Duemani Reddy et al. 2008).

Random access scanning is a promising, novel approach. However, scanning ranges have so far been limited, e.g., $50 \times 200 \times 200 \mu\text{m}^3$ (Duemani Reddy et al. 2008). Some papers reported possible technical improvements that would increase the accessible volumes to large volumes up to $350 \times 350 \times 200 \mu\text{m}^3$ (Reddy and Saggau 2005) or 1mm axial at low magnification (Duemani Reddy et al. 2008). The highest volume available for random access scanning till date was reported in our work, comprising $700 \times 700 \times 1,400 \mu\text{m}^3$ (Katona et al. 2012).

V. AIMS

I. Our previous results showed that interneurons have dendritic functional compartments that appear as a result of synaptic stimulation. Consequently, my first aims were to characterize their interactions:

- Is there linear or supralinear summation for their joint activation locally on the dendrites and globally, on the soma?
- Is there a time window for these interactions that is critical for coincidence detection?
- Is there a distance dependence of any interactions?

II. Next, combined electrophysiology and 3D two-photon imaging and uncaging were used to characterize patterns of excitatory inputs on CA1 interneuron dendrites:

- Do interneuron dendrites show similar supralinear responses to pyramidal cells for different patterns of dendritic inputs?
- What is the input-output function for the synchronous activation of different numbers of clustered inputs?
- By using a custom-made recording chamber, can we attain spontaneous responses of similar nature to the evoked ones?

III. Since our experiments so far suggested that dendritic spikes are present on interneuron dendrites, I set out to identify its properties:

- What ion channels play a role in the generation of dSpikes?
- The appearance of the voltage waveform suggested an NMDA-spike. Can we confirm that using pharmacology?
- Do VGCCs and Na_v play a role in its generation?
- How do NMDA-spikes propagate in interneuron dendrites?
- How do they relate to bAPs?

IV. Finally, to understand more the properties of the examined interneuron dendrites, we wished to examine the role nAChRs play on bAPs and their effect on LTP.

VI. METHODS

VI.1. Slice Preparation and Electrophysiology

Acute hippocampal slices were prepared from 16-20 day old Wistar rats using isoflurane anesthesia followed by swift decapitation, in accordance with the Hungarian Act of Animal Care and Experimentation (1998; XXVIII, section 243/1998.). Horizontal (300-400 μm) brain slices were cut with a vibratome and stored at room temperature in artificial cerebrospinal fluid (ACSF) (in mM: 126 NaCl, 2.5 KCl, 2 CaCl₂, 2 MgCl₂, 1.25 NaH₂PO₄, 26 NaHCO₃ and 10 glucose) as previously described (Rozsa et al. 2004; Rozsa et al. 2008; Katona et al. 2011).

Hippocampal CA1 pyramidal cells were visualized using 900 nm infrared lateral illumination (Rozsa et al. 2008). Current-clamp recordings were made at 23 °C and 33 °C (MultiClamp 700B, Digidata 1440; Molecular Devices, Sunnyvale, CA, USA; Chamber heater: Luigs & Neumann GmbH, Ratingen, Germany; in-line heater: Supertech Ltd., Pécs, Hungary). For whole cell current-clamp recordings, borosilicate glass electrodes (6–9 M Ω) were used filled with (in mM): 125 K-gluconate, 20 KCl, 10 HEPES, 10 Di-Tris-salt phosphocreatine, 0.3 Na-GTP, 4 Mg-ATP, 10 NaCl, and 0.1 Oregon Green BAPTA-1 (OGB-1, Invitrogen). In fast propagation speed measurements 0.2 Fluo-5F pentapotassium salt (Fluo-5F, Invitrogen) and 0.2 Alexa 594 (Invitrogen) was used instead of OGB-1. For extracellular current-clamp recordings glass electrodes (6–9 M Ω) were filled with ACSF or with ACSF containing 1M NaCl. All chemicals and drugs were purchased from Sigma unless otherwise noted. Cells with a resting membrane potential more negative than –50 mV were accepted.

Focal synaptic stimulation was performed as described earlier (Rozsa et al. 2004; Rozsa et al. 2008; Katona et al. 2011). Briefly, 6-9 M Ω glass electrodes filled with ACSF were placed at a distance of 10-15 μm from the dendrite (stimulation: 0.1 ms, 10-50 V, 10 ms pulse interval; 1-3 stimuli, Supertech Ltd., Pécs, Hungary). Stimulation of the Schaffer collaterals was performed with an increased voltage of 100V, using the same protocol as for focal electrical stimulation. Backpropagating APs were induced by somatic current injections (200–400 pA, 5 ms; 1-3 bAPs were evoked at 50 Hz). All evoked EPSPs were verified for synaptic delay.

VI.2. Dual Superfusion Chamber

In order to maintain network activity close to the physiological values, we adapted and modified a novel submerged slice chamber (Hajos et al. 2009; Hajos and Mody 2009). The higher flow rate ($> 8 \text{ ml / min}$) and the thicker slices ($450 \text{ }\mu\text{m}$ to $600 \text{ }\mu\text{m}$) allowed the upkeep of near-physiological network conditions, as shown previously (**Fig. 11**). Imaging was made possible by modifying a bubble trap to hinder any bubbles from entering under the objective. Our oxygen measurements also confirmed the better oxygenation of slices at an increased slice depth (Chiovini et al. 2010).

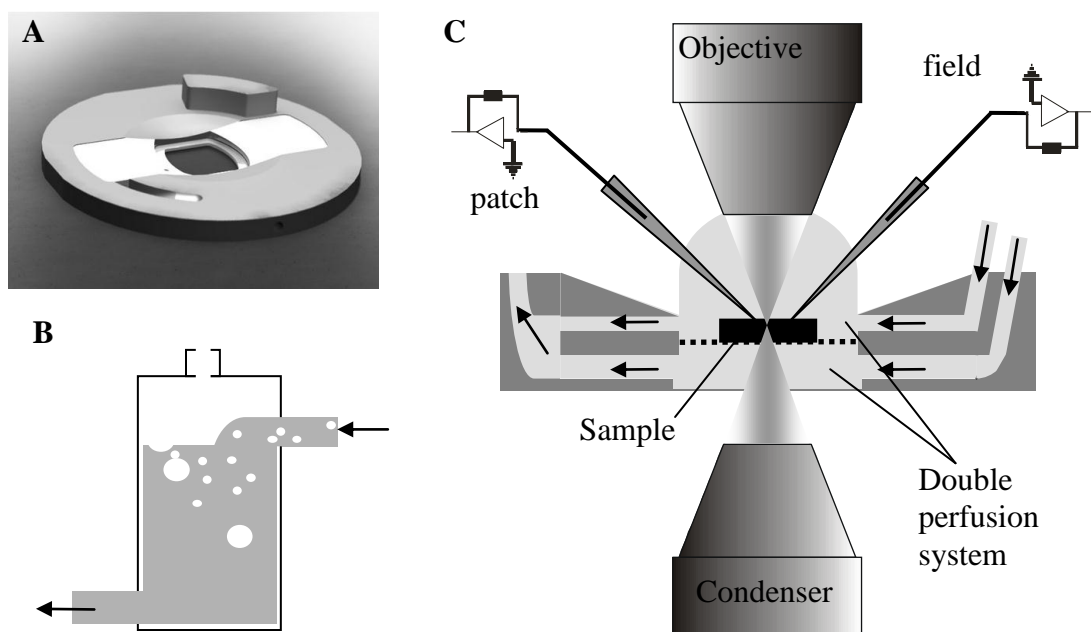


Figure 11 – Dual-superfusion submerged brain slice chamber.

A) Computer-aided design of the chamber. **B)** Scheme of bubble trap. **C)** Scheme for sample placement, stimulation and optical and electrophysiological recording. Arrows depict the direction of perfusion fluid flow. *Source: (Chiovini et al. 2010)*

VI.3. Roller Coaster Scanning

Despite considerable technological advances over the last years, functional imaging of multiple dendritic spines (or more than 16 points in 3D) “simultaneously”, that is, in the time scale of the millisecond, remains problematic (Göbel et al. 2007; Rozsa et al. 2007; Vucinic and Sejnowski 2007; Duemani Reddy et al. 2008). To address these shortcomings, a new imaging technique has been developed by combining Multiple-Line scanning (Lorincz et al. 2007) with a rapid, non-linear, piezo-based z -scanning strategy that is relatively simple. The general strategy consists in restricting the measurement to points located on a 3D trajectory that crosses locations of interest (for example dendrites and spines) in a given volume. This results in an increase in the product of the signal collection efficiency (signal/pixel) and measuring speed (repetition rate of the measurement). In this approach, galvanometric scanners are able to follow the x and y projection coordinates of the 3D trajectory up to scanning speeds of a few milliseconds (\sim kHz range scanning). However, scanning in the axial direction is more challenging. Fast z -drive by piezo-positioners has been proposed previously (Göbel et al. 2007), resulting in a 10 Hz z -scanning speed over a range of 250 μ m.

Speeding up the driving frequency of the piezo-positioner leads naturally to a drastic drop in amplitude of the – ideally sinusoid – movement (Katona et al. 2011), as a consequence of the increasing presence of nonlinear components. The z -movement therefore differs increasingly from a sinusoid and compensating for the deviation gets increasingly complicated. However, when exploring the non-linear regime of a high force cylindrically symmetric piezo actuator, we encountered resonances at 150 Hz and at 690 Hz in the objective movement without servo feedback. After a initial period of 50-100 cycles, the position of the objective reaches a steady-state nonlinear response function $z(t)$ at a mean position. At this point, one can take the measured shape of the $z(t)$ function and calculate the xy drive signal for each time point to be sent to the galvanometric mirrors, such that the $xy(t)$ position together with $z(t)$ yield the desired 3D-trajectory, yielding Roller Coaster Scanning. This procedure is exemplified in **Fig. 12**. The Roller Coaster Scanning method is ideal for rapid scanning extensive and continuous dendritic segments with high spatial resolution. Even the fine details of the spatial and temporal structure of small individual physiological events and their

different compound responses could be measured simultaneously. Its shortcoming is the relatively limited scanning range, *i.e.*, in the order of only a few tens of micron (25 μ m and 15 μ m, at 150Hz and 690Hz, respectively).

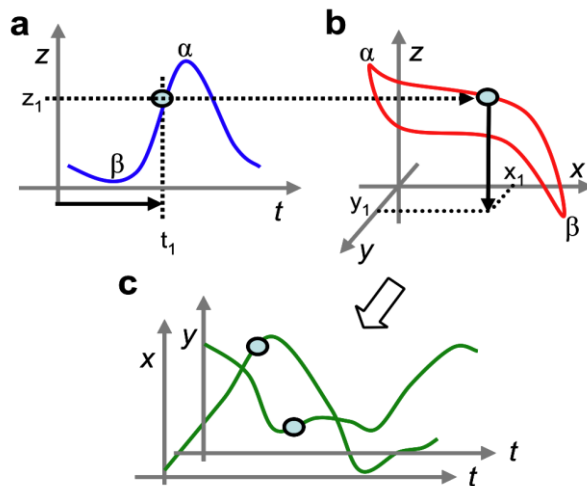


Figure 12 – Roller Coaster Scanning Method. **A)** After 50-100 cycles of the nonlinear drive (warm-up period) the nonlinear position response of the objective reached a steady-state periodic response function $z(t)$, the amplitude of which was set to be larger than the required z -scanning range. **B)** A part of this response function (typically one full period) was projected to the selected 3D trajectory.

C) The $x(t)$ and $y(t)$ input signals of the digital servo of the scanner motors were determined as the x and y coordinate projections of the 3D trajectory (x_1, y_1). The descending and ascending phase of the oscillation could cover different parts of the selected 3D trajectory as illustrated in b, The selected 3D trajectory was the result of an interpolation algorithm which was based on user-selected points on the image z -stack of the chosen dendritic region. Due to the typical shape of the trajectories, the technique goes under the name of “Roller Coaster Scanning”. *Source: (Katona et al. 2011)*

VI.4. Calcium Imaging

Two-photon imaging started 15-20 min after attaining the whole-cell configuration on a two-photon laser-scanning system (**Fig. 13**; modified from Femto2D, Femtonics Ltd., Budapest) using femtosecond lasers (800-840 nm), Mai Tai HP, SpectraPhysics, Mountain View, CA).

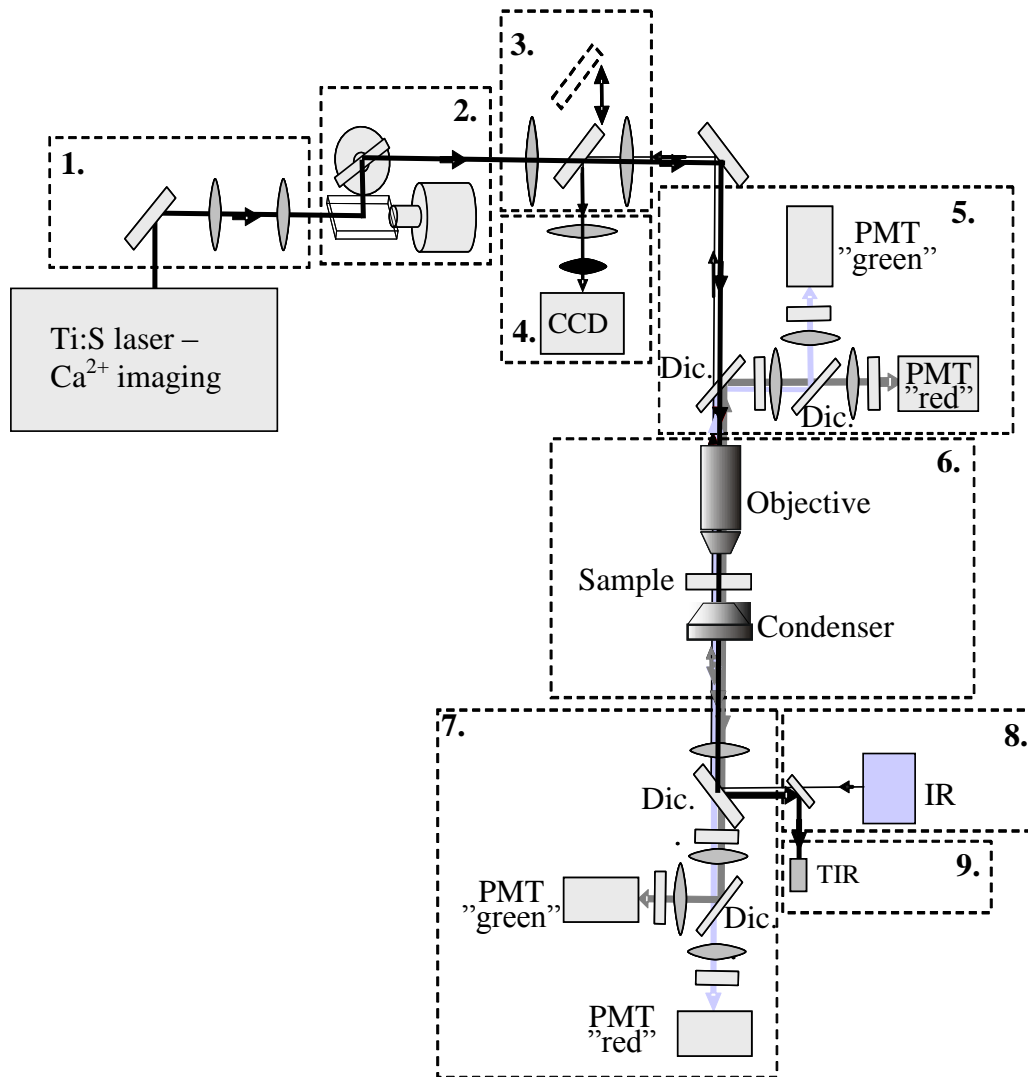


Figure 13 – Schematic drawing showing the optical design and modular nature of the 2P microscope used.

Modules: 1 - Dispersion compensation. 2 – Laser beam positioning. 3 – CCD/2P switcher. 4 – CCD camera. 5 – Upper detectors (*PMT* – photomultiplier; *Dic.* - dichroic mirror). 6 – Perfusion chamber and focusing. 7 – Lower detectors. 8 – Infrared lamp (*IR*). 9 – Transmission infrared detector (*TIR*). *Dic.*: Dichroic mirror.

Source: (Chiovini et al. 2010)

The spatially normalized and projected Ca^{2+} response (defined as 3D Ca^{2+} response) was calculated from the raw 3D line-scan, $F(d,t)$ by applying the $\Delta F/F = (F(d,t) - F_0(d)) / F_0(d)$ formula where d and t denote distance along the curve and time respectively, and $F_0(d)$ denotes the average background-corrected prestimulus

fluorescence as a function of distance along the curve. All 3D Ca^{2+} responses are color coded (colors from yellow to red show increasing Ca^{2+} responses, 0–63 % $\Delta F/F$), and projected as a function of d and t . In the experiments calculating the nonlinearity of summation following bAPs and the role of dye saturation in input-output functions the relative fluorescence value was transformed to Ca^{2+} concentration using a method described previously to eliminate the nonlinear effect of dye saturation (Tamas et al. 2003; Rozsa et al. 2004; Rozsa et al. 2008)

$$\frac{\Delta Ca}{K_D} = \frac{f_{\max}}{f} (1 - R_f^{-1}) \frac{\delta f}{(\delta f_{\max} - \delta f) \delta f_{\max}} \quad [1]$$

(equation 5 from (Maravall et al. 2000)), where δf denotes $\Delta F/F$, $R_f (= f_{\max}/f_{\min})$ is the dynamic range of the dye and K_D is the affinity of the indicator (OGB-1: 206 nM).

In order to increase the signal-to-noise ratio of the measurement dealing with dSpike lateral spread, experiments were also repeated at 25 °C. Measurement speed at 32 °C was increased to 700 Hz in these measurements. Roller Coaster Scanning was used at resonance frequencies of 120 to 200 Hz in other measurements.

At the end of each experiment, a series of images across the depth of the volume encompassing the imaged neuron was taken.

VI.5. Calculating Supralinearity

For the somatic recordings, we calculated the summation ratio in percentage (%SR) using the formula $\%SR = (2S - S1)/S2 * 100$, where 2S is the two stimuli given within a certain interstimulus interval (ISI), while S1 and S2 are the responses after the first and second stimuli respectively (S2 evoked with more than 2s delay after S1). When imaging the Calcium signals, the stimulation-evoked Calcium compartment borderlines were used to determine the locations (L1, L2) and to calculate the supralinearity of the two separate compartments activated synchronously or with a given interstimulus interval as follows. The sum of the two inputs was calculated at location L1 as the arithmetic sum of the values recorded after the first ($S1_{L1}$) and second stimulus ($S2_{L1}$) at location L1 ($SUM_{L1} = S1_{L1} + S2_{L1}$). This arithmetic sum would mean linear summation at L1. The integration values (Int) were calculated by comparing the arithmetic sum to the coupled activation of the two inputs (2S), as follows:

$\text{Int}=2S_{L1}/\text{SUM}_{L1}$ or $\% \text{Int}=2S_{L1}/\text{SUM}_{L1} * 100$. The same calculation was performed for the second location, L2.

VI.6. Two-Photon Uncaging

After achieving whole-cell mode and filling the interneurons with 60 μM OGB-1, the bath solution was exchanged to ACSF containing 4-Methoxy-7-Nitroindoliny (MNI)-caged L-glutamate (2.5 mM; Tocris) or 4-Methoxy-7-Nitroindoliny (MNI)-caged L-glutamate trifluoroacetate (2.5 mM; Femtonics Ltd., Budapest, Hungary). Photolysis of caged glutamate was performed with 720 nm ultrafast, pulsed laser light (Mai Tai HP Deep See, SpectraPhysics, Mountain View, CA). The intensity of the uncaging laser beam was controlled with an electro-optical modulator (Model 350-80 LA, Conoptics). Dispersion compensation was set to have maximal response at the depth of uncaging (50-80 μm from surface). The uncaging laser beam was coupled into the 3D imaging optical pathway with a dichroic mirror (custom laser combiner, z750bcm; Chroma Technology Corp, Rockingham, USA). Three dimensional imaging was limited to $< 7 \mu\text{m}$ z-scanning ranges and the imaging laser wavelength was set to 840-860 nm in uncaging experiments. Chromatic aberration was compensated for at the focal plane. Radial and axial beam alignment errors were held below 100 nm and 300 nm respectively. Three dimensional imaging was interleaved with two-photon glutamate uncaging periods when galvanometers jumped to the maximum of 38 selected locations ($< 60 \mu\text{s}$ jump time) and returned back to the 3D trajectory thereafter. The position of uncaging sites was finely adjusted according to images taken. Photolysis of caged glutamate was performed either in “clustered” ($0.8 \pm 0.1 \mu\text{m}$ distance between inputs) or “distributed” ($2.3 \pm 0.16 \mu\text{m}$ distance between inputs) patterns along the dendrite. We set the single spot uncaging time and laser intensity to reproduce uEPSPs and mEPSPs induced by the local application of high osmolar external solution (Losonczy and Magee 2006) at similar distances from the soma (amplitude of unitary gluEPSP: $0.56 \pm 0.09 \text{ mV}$, mEPSPs: 0.58 ± 0.1 , uEPSP: 0.55 ± 0.12 ; exposure time 0.2-0.5 ms/input). Uncaging sites were gradually, but randomly omitted one after the other until only one (“unitary”) site remained. Uncaging with the maximum number of locations was repeated at the end of the experiments, and measurements with different initial and final maximum values were excluded.

In experiments investigating the role of NMDA receptors, the bath solution was changed to ACSF containing MNI-glutamate and the selective NMDA-receptor antagonist D,L-AP5 (60 μ M; Sigma-Aldrich) while the same clustered uncaging pattern series was repeated. Similarly, the roles of Nav and VGCCs were investigated by repeating the same clustered uncaging pattern in the presence of TTX (1 μ M; Tocris) and VGCC channel blockers (Mibefradil, 50 μ M, Nimodipine, 20 μ M, omega-Conotoxin GVIA 5 μ M; Tocris), respectively.

Functional mapping of postsynaptic elements was carried out according to (Matsuzaki et al. 2001). Uncaging laser light was shined briefly (0.4-2ms) three times (10 Hz) onto each pixel (0.3 x 0.3 - 0.5 x 0.5 μ m). During the uncaging stimulus, the scanner was performing a spiral pattern within the pixel. Small drifts of the sample (on the order of 0.1-0.2 μ m) during the mapping were compensated manually according to regularly taken background images. Cells were kept voltage-clamped at -70 mV. Uncaging-evoked EPSCs were visually inspected to avoid contamination with spontaneous EPSCs and averaged. A color coded map was constructed of the peak of the EPSCs. Precise alignment of the maps with the background images was helped by the smoothed images formed of the fluorescence intensity measured during the uncaging events. Smoothed images have been refined by two cycles of doubling resolution using linear interpolation.

VI.7. Investigating nAChR Effects

In the study dealing with the nature and effect of nAChRs, the following drugs were applied throughout the experiments unless otherwise stated in order to inhibit synaptic transmission and muscarinic ACh receptors during ACh application: atropine (1 μ M), bicuculline (20 μ M), DL-2-amino-5-phosphonopentanoic acid (AP5, 40 μ M), and 6,7-nitroquinoxaline-2,3-dione (DNQX, 10 μ M), or 6-cyano-7-nitroquinoxaline-2,3-dione (CNQX, 10 μ M). Other blockers, cyclopiazonic acid (CPA; 30 μ M), methyllycaconitine (MLA; 10 nM), tetrodotoxin (TTX, 1 μ M), mecamylamine (10 μ M), as well as also nicotinic AChR agonists, acetylcholine chloride (1 mM) and choline chloride (10 mM) were injected using a continuous-flow, motion artifact free, rapid perfusion system (DAD). The tip of the pipette was directed to the region of interest. In

our continuous-flow system we could change solutions in the 100 μm capillary of the manifold (ALA Scientific Instruments) without changing the flow speed and pressure, thus avoiding pressure transients (Lorincz et al. 2007). The advantage of this method compared to bath application is rapid drug delivery, so the effects of the drugs on the Ca^{2+} transient can be readily distinguished from the cell loading artifact. The measured parameters (amplitude, decay time constant of the Ca^{2+} transients) appeared as sharp changes as a function of time.

VI.8. Histology

Visualization of biocytin and light microscopy was performed as described earlier (Tamas et al. 2003). Three-dimensional light microscopic reconstructions were carried out using NeuroLucida (MicroBrightfield, Colchester, VT) with a 100x objective. Morphological characteristics were confirmed by anatomical reconstruction and image stacks were collected at the end of recordings.

Of the recorded cells (all with cell bodies located in the str. radiatum), ten interneurons were identified based on their axonal and dendritic arborization. Cells have been classified as previously (Hajos and Mody 1997). In four cases, the axonal arbor was restricted to the str. radiatum (radiatum cells), in five cases the axon also ramified in the strata pyramidale and oriens (trilaminar cells) in addition to the str. radiatum, and in one instance, the axon was located only in the str. lacunosum-moleculare (R-LM cell). Thus, all intracellularly labeled interneurons belonged to the functional category of dendrite-targeting inhibitory cells, since their axon branched predominantly in the layers where the dendrites of CA1 pyramidal cells are located.

VI.9. Data Analysis and Statistics

Measurement control, real-time data acquisition and analysis were performed with a MATLAB based program (MES, Femtonics Ltd., Budapest) and by custom-written software. For cluster analysis, from each EPSP we subtracted the average monocomponent EPSPs (averaged for each given cell) and integrated the difference in the first 0 to 175 ms interval after stimulus onset. We plotted the normalized integral value as a function of the normalized peak of the corresponding Ca^{2+} -transient. During normalization we defined unity as an average of the three largest responses of the given cell. We used these two normalized measures used for agglomerative clustering of

Euclidean distances by using the Ward method. The gap statistic method was used to determine the number of clusters (Tibshirani et al. 2001). Cluster analysis was developed and performed by Gergely Katona and Dr. Balázs J. Rózsa, after consulting Dr. Zoltán Nusser. The gap statistic calculation was implemented as a macro within Statistica software (version 8; StatSoft). Statistical comparisons were performed by using Student's paired t test. If not otherwise indicated, data are presented as means \pm SEM.

VII. RESULTS

VII.1. Synaptic Integration Between Dendritic Computational Subunits

VII.1.1. Electrical Stimulation

Excitatory postsynaptic potentials (EPSPs) were evoked by exciting local axons arriving onto interneuron dendrites at two separate regions. Two stimulation pipettes were placed juxtaposed to the dendrites filled with ACSF and followed by infrared scanning gradient contrast (Wimmer et al. 2004). In contrast to pyramidal neurons, stratum radiatum/ lacunosum moleculare interneurons in the CA1 region of the hippocampus are mostly aspiny (Yuste and Denk 1995; Goldberg et al. 2003a) with an approximately 10-fold less synaptic input density (Gulyas et al. 1999; Megias et al. 2001; Takacs et al. 2011). Therefore, in case the stimulation did not evoke local Ca^{2+} and somatic voltage responses, pipettes were repositioned close to the dendrites with the help of a robotic manipulator based on the two-photon image of the dendrites (Polsky et al. 2004) (**Fig. 14**). Synaptic stimulation was always monitored by the appearance of the synaptic delay. The single focal electrical stimulation at the L1 and L2 locations – selected on dendritic regions with our dendritic branch points – evoked separate Ca^{2+} responses at the dendritic regions (Ca^{2+} compartments) that could be examined by placing free line scans that followed the curvature of the dendrites (*red patterned line* on **Fig. 14B**).

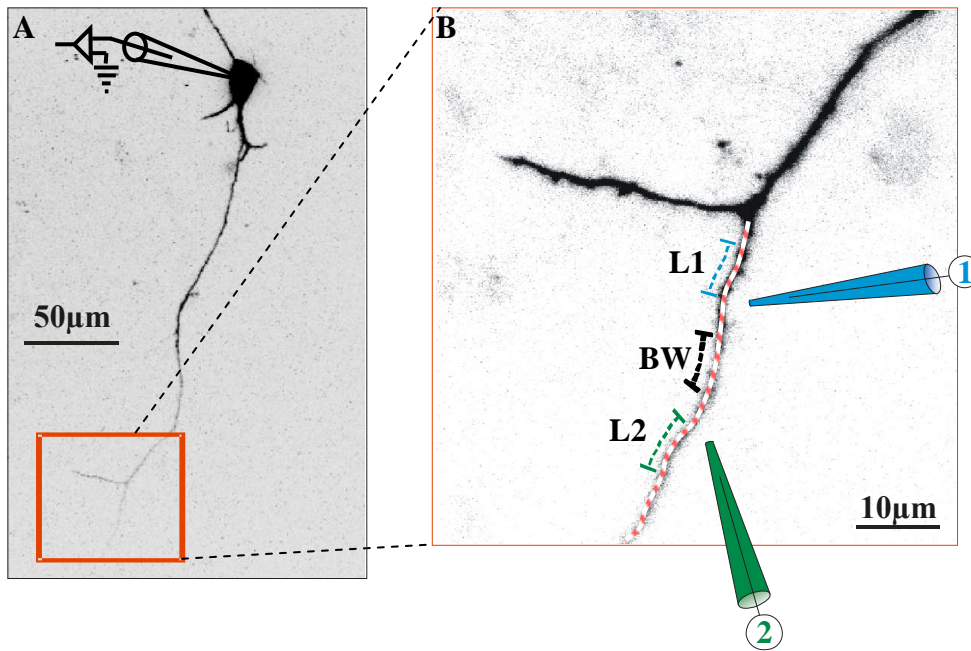


Figure 14 – Experimental setup for focal electrical stimulation.

A) Inverted maximal z-projection image of a CA1 interneuron filled with OGB-1 (60 μM) through the patch pipette. *Red squared region* shows region of interest. **B)** Enlarged view on ROI from **A**. The two stimulation pipettes placed near the dendrite are shown with *blue* and *green* for Stimulator1 and Stimulator2, respectively. The stimulated dendritic locations (location 1 & 2; L1 and L2) are depicted with dotted lines, with the in-between region (BW). *Red patterned line* shows the path of the laser beam for Ca^{2+} imaging.

The acquired Ca^{2+} traces were normalized real-time to their background fluorescence values (**Fig. 15A**) and allowed the proper separation of single stimulation evoked Ca^{2+} responses. This was feasible as by the fast line scanning mode, with a temporal (line scan frequency ranged from 165Hz to 333Hz) and a spatial resolution (characteristic of 2P microscopy) that made the separation of Ca^{2+} entry sites possible (**Fig. 15A**). In this way, we could determine the exact location of the EPSP that was recorded simultaneously at the soma.

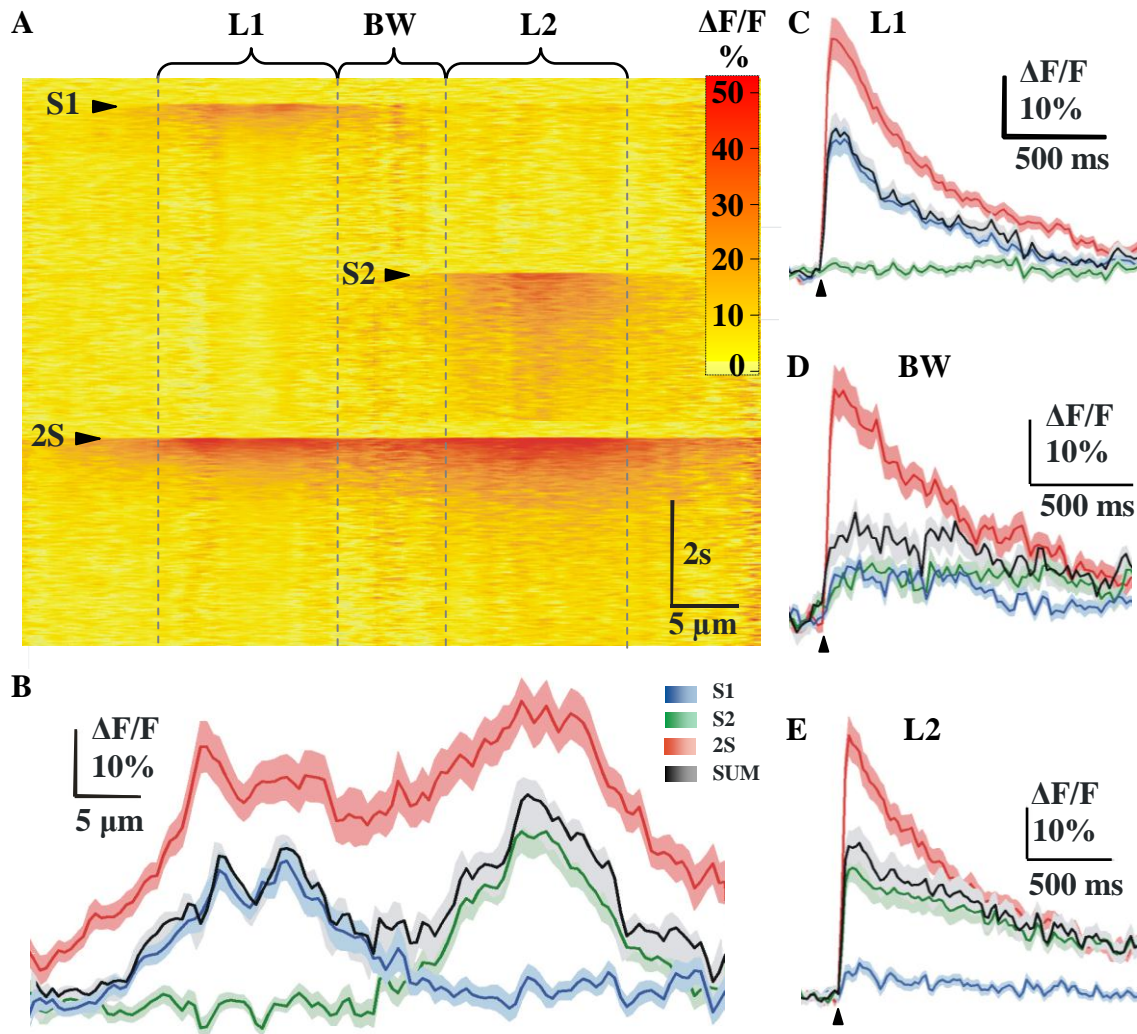


Figure 15 – Representative measurement for Ca^{2+} imaging of focal electric stimulation evoked events.

A) A representative normalized Ca^{2+} signals for the first (S1), second (S2) and dual (2S) stimulations. *Dashed grey lines:* boundaries for L1, BW and L2 locations are shown for the Ca^{2+} traces in C-E. **B)** The spatial extent of Ca^{2+} responses (mean \pm SEM) for the different stimulation protocols and for the arithmetic sum of the Ca-responses for S1 and S2. **C-E)** Ca^{2+} transients (mean \pm SEM) at different locations (L1, BW and L2) show that the two stimulations elicited in synchrony cause the supralinear summation of response. *Black arrowheads:* stimulation.

At the double stimulation, the Ca^{2+} responses showed supralinear summation at each region when compared to the arithmetic sum of single stimulus values. Supralinearity in local Ca^{2+} peak and area at L1 location was: $\text{Ca}_{\text{max}}=133.25\pm 6.64\%$, $\text{Ca}_{\text{area}}=145.28\pm 10.52\%$ (N=15/9 locations/cells; **Fig. 15C, 16A**), at location L2: $\text{Ca}_{\text{max}}=127.48\pm 9.7\%$, $\text{Ca}_{\text{area}}=122.74\pm 8.83\%$, (N=12/9 locations/cells; **Fig. 15E, 16C**). In most of the cases, the locations were distinct enough to exactly determine the measure of supralinearity between the L1 and L2 locations (BW; $\text{Ca}_{\text{max}}=140.95\pm 10.82\%$, $\text{Ca}_{\text{area}}=158.73\pm 11.49\%$, N=7/6 locations/cells; **Fig. 15D, 16B**).

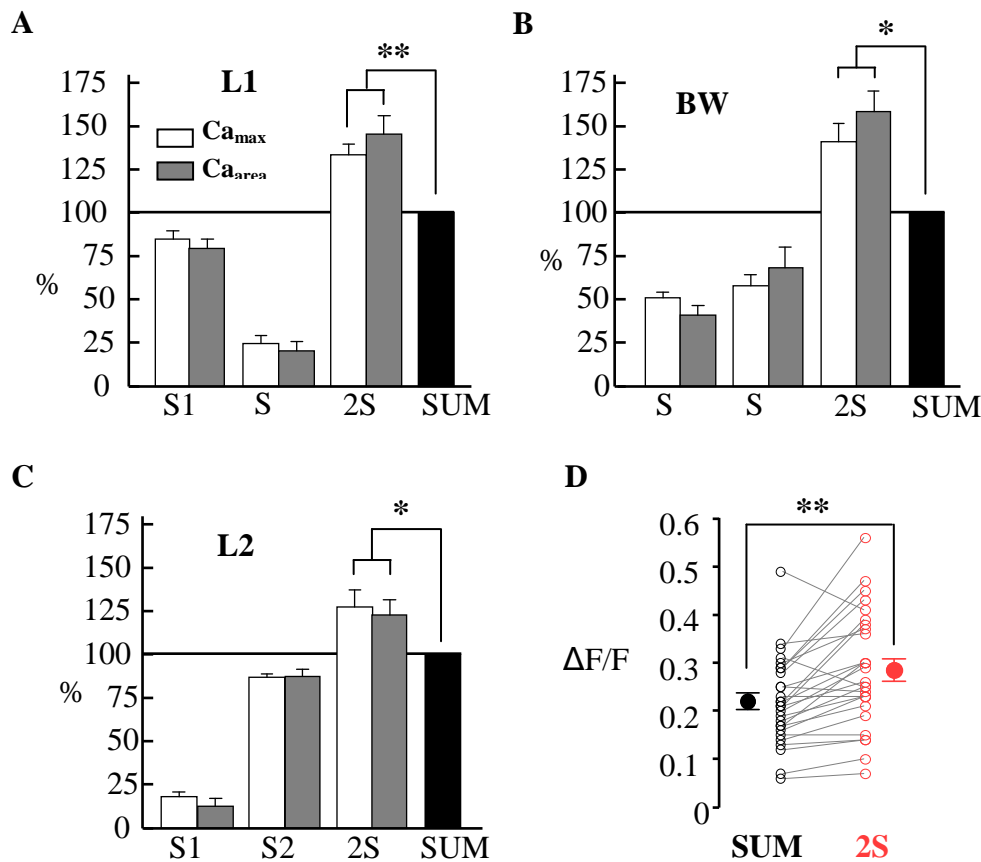


Figure 16 – Supralinear summation in synchronous dendritic Ca^{2+} events.

A-C) Average calcium transient amplitudes and areas in percentage of the calculated sum for L1 (n=15/9 locations/cells), BW (n=7/6 locations/cells) and L2 (n=12/9 locations/cells), where signal integration was calculated for the given location (eg. $\text{Int}_{\text{L1}}=\text{L1}_{\text{S1}}+\text{L1}_{\text{S2}}$). **D)** Data for pooled Ca^{2+} amplitudes (n=27/9 locations/cells, * $p<0.05$; ** $p<0.001$).

Since Ca^{2+} imaging was simultaneously performed with whole-cell current clamp recording, the recorded somatic EPSPs (**Fig. 17B**) could also be compared when single or double locations were stimulated. When comparing the arithmetic sum of separate single stimuli with the double stimulation (2S) evoked EPSPs (see **Fig. 17A** for 2S protocol), the double stimulation showed summation with a similar amplitude to Ca^{2+} events ($\text{EPSP}_{\text{max}}=141.72\pm 16.97\%$, $\text{EPSP}_{\text{area}}=141.67\pm 12.47\%$, $N=9$ cells, $p<0.05$; **Fig. 17C**).

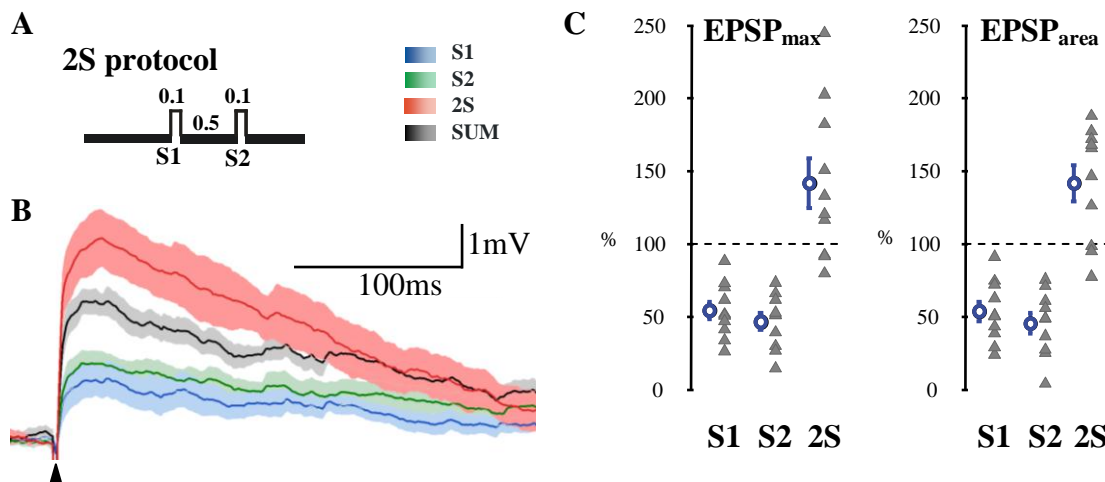


Figure 17 – Focal electrical stimulation evoked EPSPs show supralinear summation.

A) Double stimulus protocol: 0.5ms delay was introduced between the two focal stimulations to avoid non-physiological, electrical summation of stimulus signals. **B)** Focal electrical stimulation evoked EPSPs (Mean \pm SEM) in relation to the arithmetic sum. **C)** Summary graph showing mean EPSP maxima (left panel) and EPSP areas (right panel) for the recorded and imaged cells ($N=9$ cells) in percentage of the calculated sum (SUM). Double stimulation showed significant supralinearity ($p<0.05$). *Black arrowhead*: stimulation.

VII.1.2. Two-Photon Photoactivation of Glutamate

To validate our results on signal integration, I turned to the noninvasive method of focal two-photon glutamate photoactivation (Matsuzaki et al. 2001). I selected regions of interneuron dendrites and photoactivated glutamate at distinct clusters of points placed adjacent to the dendrite (Fig. 18).

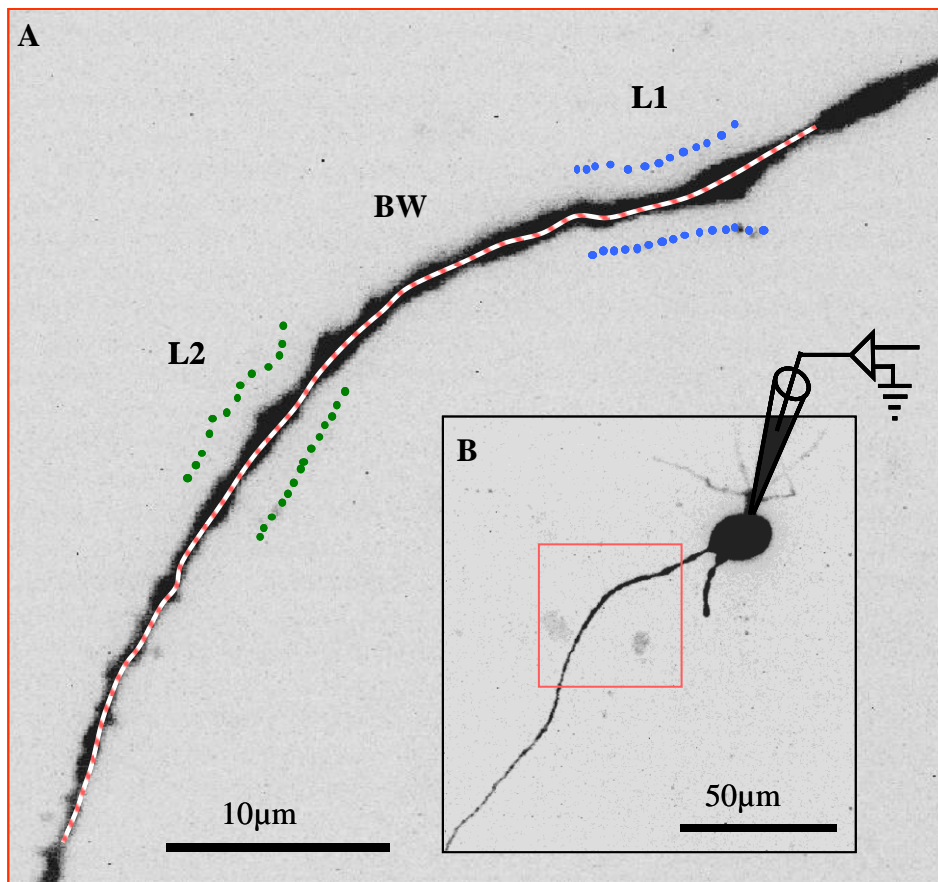


Figure 18 – Experimental setup for 2P photoactivation.

A) Enlarged view of a CA1 interneuron dendrite filled with OGB-1 (60 μ M) through the patch pipette. Photoactivation of glutamate was performed at L1 (*blue*) and L2 (*green*) points, but not between (BW). *Red patterned line* shows the path of the laser beam for Ca^{2+} imaging. **B)** Inverted maximal z-projection image of the recorded and imaged interneuron. *Red squared region* shows ROI with dendrite on A.

Ca²⁺-transients appeared at the stimulated regions only (L1 & L2; **Fig. 19A, C**) and showed little or no overlapping with the unstimulated sites in-between (BW; **Fig. 19B**). When the two clusters were stimulated near-synchronously (1ms ISI), the Ca²⁺ signals recorded by two-photon imaging showed significant supralinear summation when compared to the arithmetic sum of the two sites (%Control; Ca_{max}=120.37±4.31, Ca_{area}=123.36±4.81; N=56/14 locations/cells; $P < 10^{-7}$; **Fig. 20A**). Simultaneously recorded uncaging-evoked EPSPs (uEPSPs; **Fig. 19D**) at the soma also showed significant supralinearity in their summation ratio (SR=(2S-S1)/S2*100; uEPSP_{max}=110.08±4.16, uEPSP_{area}=125.88±7.25; N=14 cells; $P < 0.05$; **Fig. 20B**).

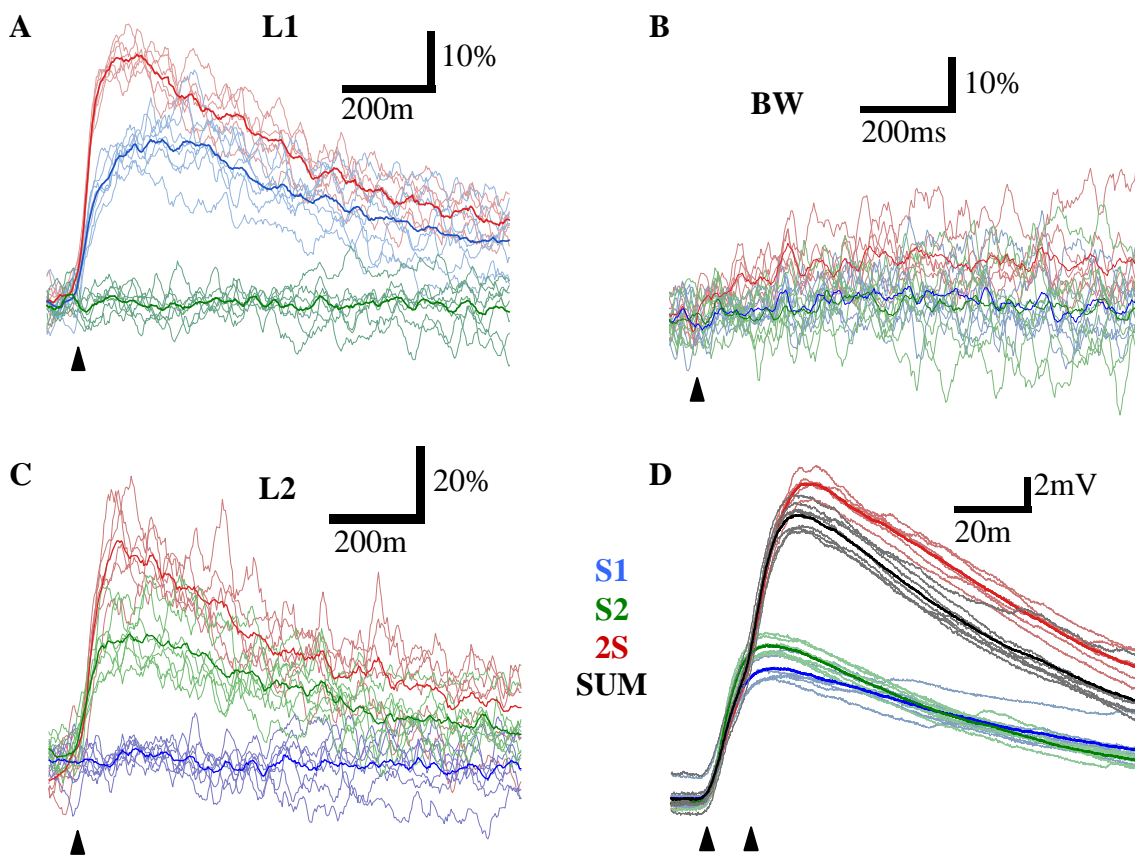


Figure 19 – Supralinear signal integration by synchronous photoactivation of two input clusters – representative traces.

A-C) Uncaging-evoked Ca²⁺ signals for dendritic regions L1 (A), L2 (C) and in between (BW; B) in a representative cell shown on **Figure 18**. **D)** Uncaging-evoked EPSPs (uEPSPs) recorded at the soma (*thin lines*: single traces; *thick lines*: averages; *blue* and *green* traces: stimulation of single clusters only; *red* traces: uncaging at both clusters). *Black arrowhead*: stimulation. SUM: arithmetic sum.

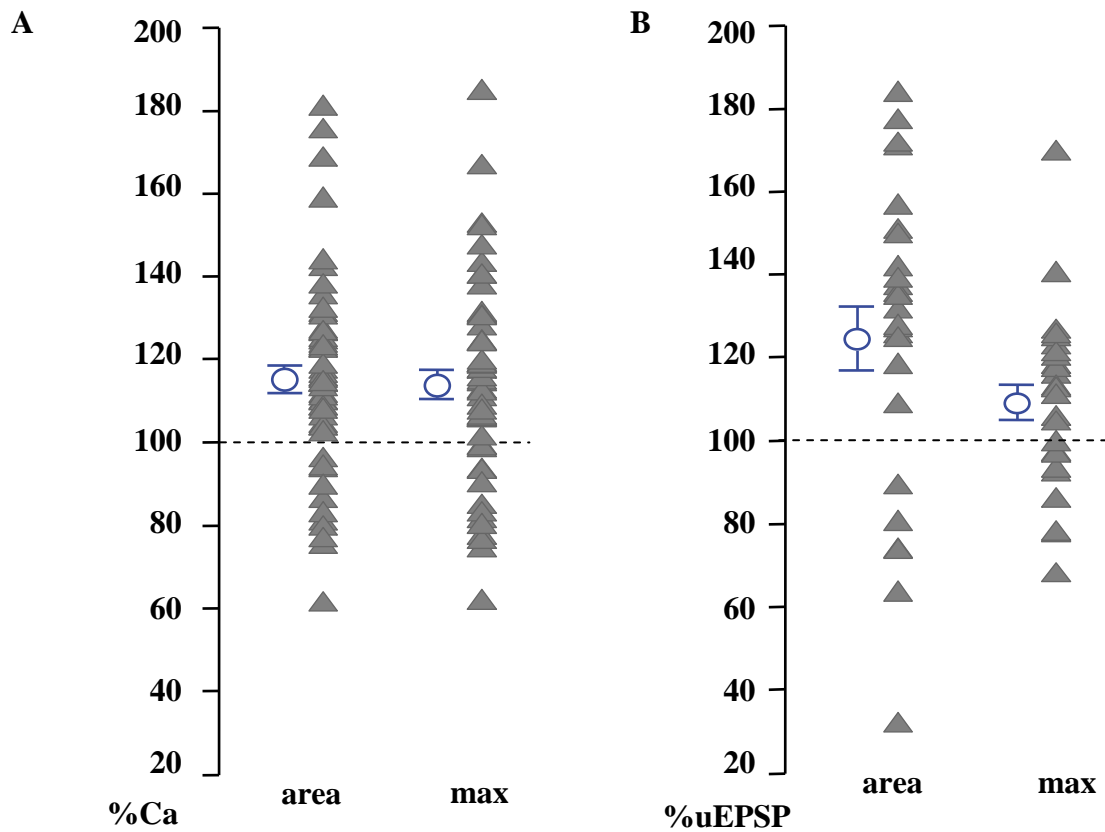


Figure 20 – Near-synchronous photoactivation of two input clusters evokes supralinear signal integration.

A-B) The area and maxima for the near-synchronous activation of two clusters of both Ca^{2+} -signals (A; $N=56/14$ locations/cells) and somatically recorded uEPSPs (B; $N=14$ cells) show significant (A: Ca^{2+} $P < 10^{-7}$; B: uEPSP $P < 0.05$) supralinear summation when compared to the arithmetic sum of the two clusters photoactivated separately. Triangles show single values for regions (A) or cells (B), while blue empty circles show mean \pm SEM. $\%Ca = [2S/(S1+S2)*100]$; $\%uEPSP$: summation ratio [$SR=(2S-S1)/S2*100$].

VII.1.3. Coincidence Detection in CA1 Interneuron Dendrites

In the above mentioned studies, we stimulated the two separate input locations with a distinct, but negligible latency: 0.5 ms interstimulus interval (ISI), both for focal electrical stimulation and for 2P glutamate photoactivation. These latency values are interpreted by the dendrite as synchronous excitation with regards to signal integration (Markram et al. 1997; Hausser et al. 2000; Stuart and Hausser 2001; London and Hausser 2005; Losonczy and Magee 2006; Calixto et al. 2008).

Nevertheless, the question arises: what is the coincidence detection rate for differently timed dual input stimulation? To answer this question, we used 2P photoactivation of Glutamate as applied above, but introduced a defined time delay in stimulating the second cluster (**Fig. 21**).

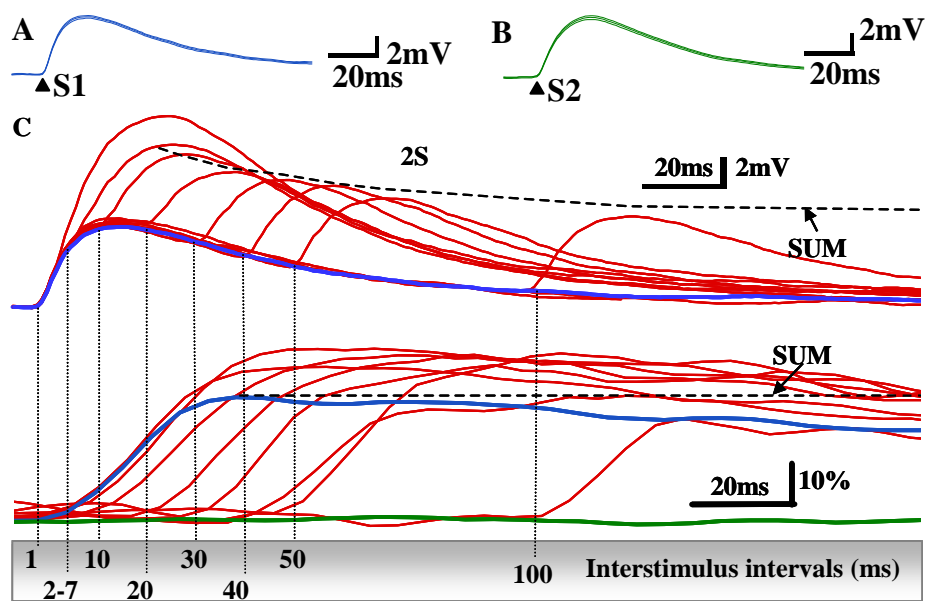


Figure 21 – Timing of coincidence detection in dendrites of interneurons.

A-B) Somatic uEPSPs (mean \pm SEM) evoked by Glutamate photoactivation for the first stimulus (S1), followed by the second stimulus (S2). **C)** Representative traces for the integration of somatic uEPSPs (*top*) and dendritic Ca^{2+} -traces of one of the locations (L1, *bottom*) for the given interstimulus intervals (ISIs; *Blue*: S1; *Green*: S2; *Red*: double stimulus, 2S). S1 induced a Ca^{2+} -trace at L1 (*blue trace*), whereas S2 applied to a different location gave no Ca^{2+} -response at L1 (*green trace*). *SUM*: S1 + S2. *Black arrowhead*: stimulus.

We increased the delay between stimuli in the range of 1 to 100 ms (interstimulus interval in ms: ISI = 1; 2-7;10; 20; 30; 40; 50; 100). The uEPSPs recorded at the soma showed supralinearity in their amplitude only for the synchronous inputs with 1ms ISI, but supralinearity was present in a wider temporal window of 1-10ms for the uEPSP areas (**Fig. 22A**). Furthermore, the simultaneously imaged active areas showed supralinear increase for both the amplitude and area for their Ca^{2+} -traces (**Fig. 22B-C**). Further values for uEPSP and Ca^{2+} amplitudes and areas from all uncaging experiments are given in **Table 1** & **Table 2**.

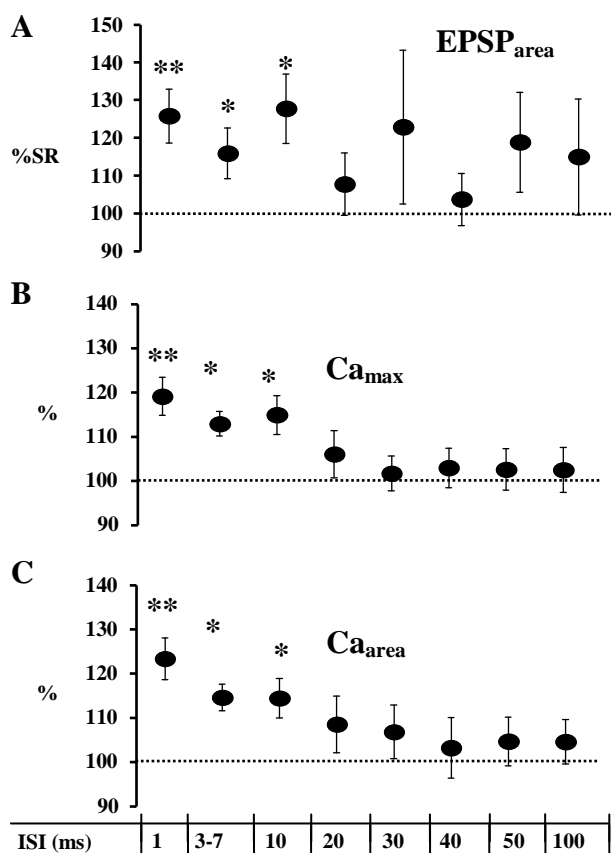


Figure 22 – Coincidence detection of CA1 interneuron dendrites.

A) Statistics for the timing-dependent supralinearity of uEPSP areas [$\%SR=(2S-S1)/S2*100$] shows supralinearity of near-synchronously activated clusters of inputs. **B-C)** Ca^{2+} -transient maxima (**B**) and areas (**C**) with ISIs of 1-100ms [$\%=2S/(S1+S2)*100$] show similar supralinearity range of 1-10ms as uEPSPs. * $P < 0.05$. ** $P < 0.01$; see Table 1 for complete statistical analysis.

Uncaging-evoked EPSP (uEPSP) areas for given interstimulus intervals (ISIs)

	ISI (ms)	1	3-7	10	20	30	40	50	100	250
Range	Mean	125,88	115,96	127,78	107,77	122,95	103,71	118,90	115,02	111,78
	SEM	7,25	6,84	9,85	8,77	21,62	7,38	14,03	16,47	14,85
	min	31,19	65,56	84,40	74,19	78,05	84,66	69,35	57,61	78,16
	max	183,17	190,05	175,48	158,53	232,72	154,41	190,24	193,48	173,94
t-test	P =	<u>0,0003</u>	<u>0,0108</u>	<u>0,0046</u>	0,181	0,138	0,301	0,086	0,173	0,203

uEPSP amplitudes for the same ISIs

	ISI (ms)	1	3-7	10	20	30	40	50	100	250
Range	Mean	110,08	100,86	103,40	96,18	100,44	94,97	105,47	108,15	103,29
	SEM	4,16	3,92	7,37	3,52	4,67	3,61	4,60	7,44	5,95
	min	66,02	72,76	81,36	73,83	65,99	78,67	68,16	78,15	68,09
	max	320,76	162,17	143,21	170,88	145,59	160,65	139,73	142,18	136,18
t-test	P =	<u>0,0085</u>	0,4121	0,315	0,133	0,460	0,080	0,113	0,131	0,280

Locations	n=	27	6	8	9	9	9	9	8	6
Cells	N=	14	5	7	8	8	8	8	7	5

Table 1 – Signal integration of inputs with different intersimulus intervals.

Table shows values for the summation somatically recorded uEPSP areas and maxima for two uncaging-evoked events, separated by a defined intersimulus interval (ISI). Values are in %Summation Ratio [%SR=(2S-S1)/S2*100].

Areas of dendritic Ca²⁺-traces imaged synchronously with uEPSPs

	ISI (ms)	1	3-7	10	20	30	40	50	100	250
Range	Mean	123,36	114,62	114,47	108,49	106,85	103,21	104,66	104,60	95,39
	SEM	4,81	3,06	4,61	6,65	6,24	7,03	5,68	5,18	4,18
	min	65,36	82,99	90,41	68,39	78,59	75,34	62,63	73,14	64,97
	max	320,76	178,73	148,81	196,36	192,30	196,80	145,59	135,73	113,56
t-test	P =	0,000002	0,000003	0,0014	0,099	0,133	0,321	0,202	0,183	0,131

Amplitudes of dendritic Ca²⁺-traces imaged synchronously with uEPSPs

	ISI (ms)	1	3-7	10	20	30	40	50	100	250
Range	Mean	120,37	114,13	116,16	107,26	102,93	104,18	103,83	103,72	96,96
	SEM	4,31	2,80	4,53	5,51	4,07	4,64	4,78	5,25	5,50
	min	66,02	72,76	81,36	73,83	65,99	78,67	68,16	78,15	68,09
	max	320,76	162,17	143,21	170,88	145,59	160,65	139,73	142,18	136,18
t-test	P =	0,000003	0,000001	0,0005	0,092	0,232	0,180	0,208	0,235	0,284

Locations	n=	56	14	16	18	18	18	18	15	11
Cells	N=	14	5	7	8	8	8	8	7	5

Table 2 – Signal integration of inputs with different intersimulus intervals.

Local Ca trace areas and maxima for the different interstimulus intervals (ISIs).

Values are in % [$\% = 2S / (S1 + S2) * 100$].

VII.1.4. Distance Dependence of Signal Integration in CA1 Interneurons

Previous studies have pointed out that the activated input sites play a different role in signal processing, integration and propagation in the function of distance from the soma (Tamas et al. 2002; Poirazi et al. 2003b; Losonczy and Magee 2006; Sjoström et al. 2008; Katz et al. 2009; Larkum et al. 2009). The focal activation of inputs allowed the analysis of not just the somatic distance dependence of signal integration, but also the effect of intercluster distance and the distance from bifurcations. However, our results neither show any significant difference for the somatic distance of input sites, nor for the interlocation distances (Fig. 23).

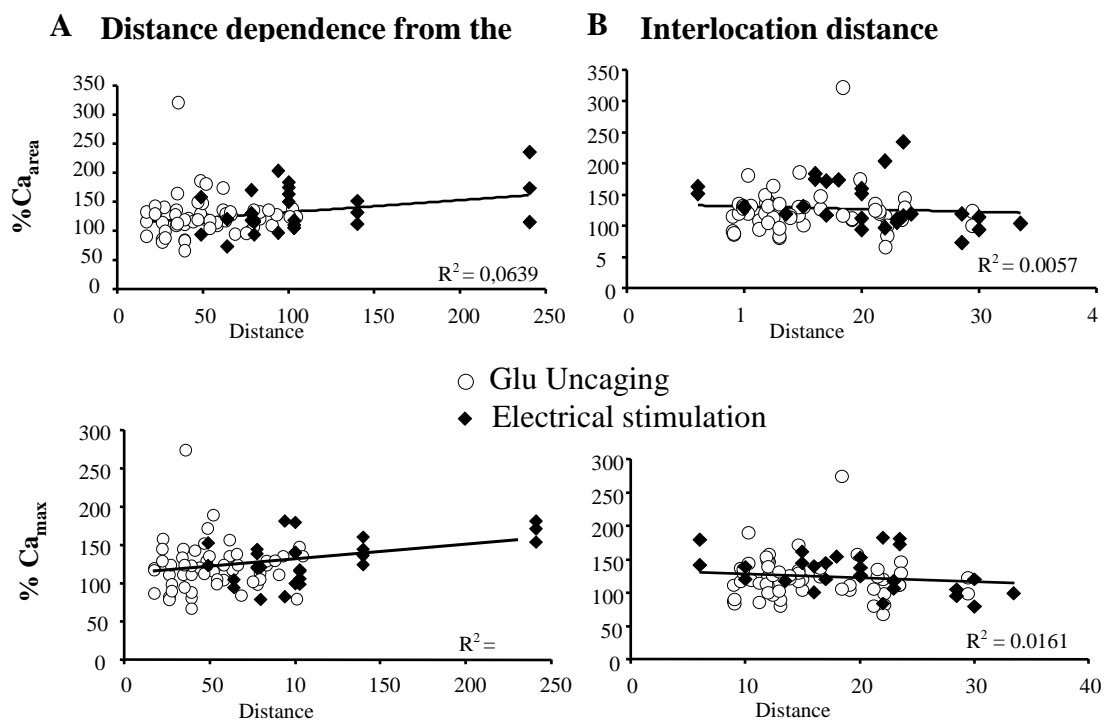


Figure 23 – Dendrites of CA1 interneurons show no distance-dependent signal integration.

Dendritic signal integration values after double stimulation in percent of arithmetic mean, depicted in the function of distance from the soma (A) or the distance between separate activated locations (B). Top row: Calcium areas; bottom row: Calcium maxima.

VII.1.5. Spatial Characteristics of Dendritic Signal Integration in CA1

Interneurons

The focal glutamate uncaging experiments described above showed supralinear signal integration between two locations on the dendrites of interneurons. The stimulation protocol consisted two separate clusters of inputs at two distinct locations. Next, our aim was to see how the spatial distribution of inputs affects signal integration at one given location. For this purpose, interneuron synapses were functionally mapped by glutamate uncaging as it has been shown previously for pyramidal cells (Matsuzaki et al. 2001) (**Fig. 24**).

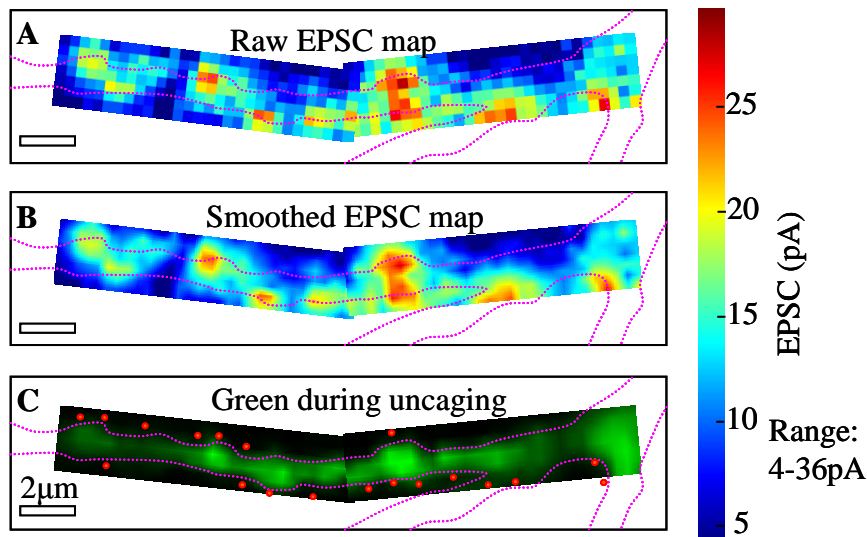


Figure 24 – Mapping of synaptic locations in CA1 str. rad. interneurons.

A) Representative example for functional mapping of synaptic locations by two-photon glutamate uncaging in experiments in. Images of two measurement series formed using the EPSC amplitudes evoked by uncaging at distinct points, performed in two narrow boxes. **B)** Smoothed glutamate sensitivity map by linear interpolation. **C)** Smoothed image formed of the green fluorescence intensity measured during the uncaging events validating the precision of the uncaging locations. Dendrite is outlined with *dashed magenta lines*. *Red dots* show the sites selected for further studies. *Colorbar* shows EPSC amplitude.

Here, we chose a single dendritic branch and used two-photon glutamate uncaging. We measured the summation of dendritic 3D Ca^{2+} -responses and

simultaneously recorded somatic EPSPs evoked by multisite photostimulation (gluEPSP). The clustered input patterns used had a density of $0.8 \pm 0.1 \mu\text{m}/\text{input}$, corresponding to the reported $0.7\text{-}1.3 \mu\text{m}/\text{synapse}$ density (Gulyas et al. 1999), and covered $18.1 \pm 2.6 \mu\text{m}$ dendritic segments (**Fig. 25A**). Clusters were located $76 \pm 9 \mu\text{m}$ from the soma on randomly chosen dendritic segments. The single spot uncaging time and laser intensity were set to reproduce unitary EPSPs and high-osmolar ACSF induced mEPSPs evoked at the same distance from the soma (see Materials and Methods).

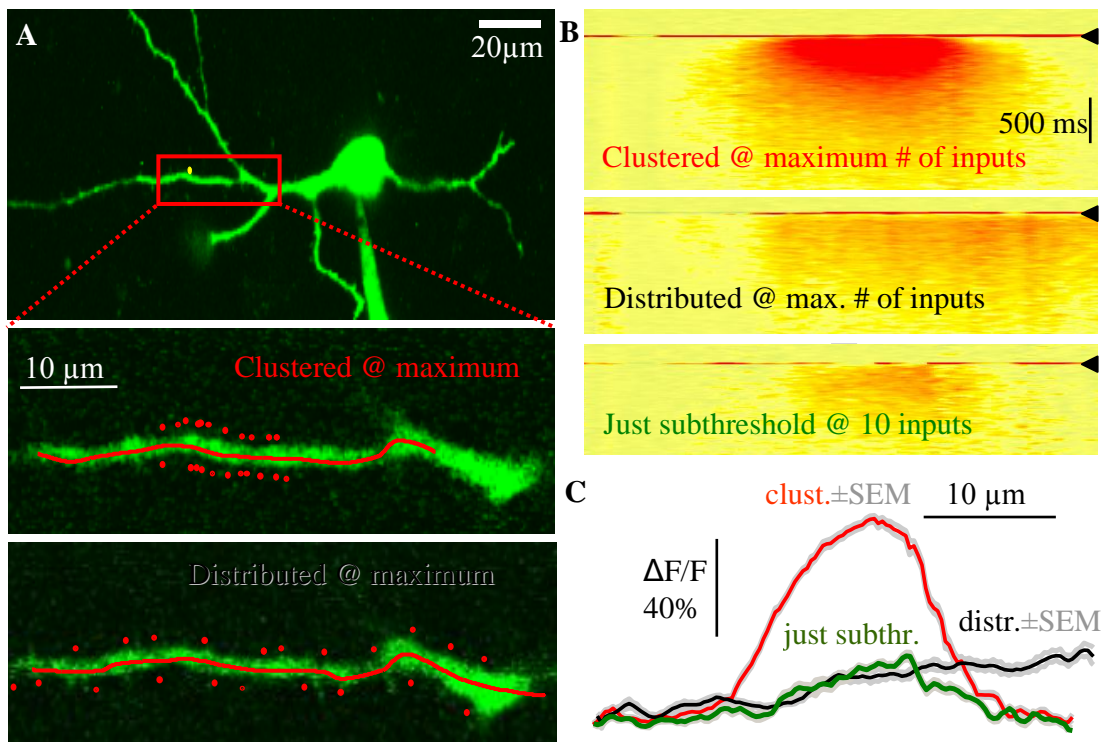


Figure 25 – Spatial characteristics of responses.

A) *Top*, Maximum intensity image stack projection. *Bottom*, Single scan images showing the maximal 22 locations used for two-photon glutamate uncaging for the clustered and distributed input patterns. **B)** Representative uncaging-evoked 3D Ca^{2+} -responses when the maximum number of inputs was activated for clustered (*top*) and distributed input patterns (*middle*). *Bottom*, Just subthreshold clustered inputs induced small responses with narrower distribution. **(C)** Spatial distribution of the peak 3D Ca^{2+} -responses in B. *Gray traces* show mean \pm s.e.m.

Such clustered input patterns always induced 3D Ca^{2+} responses that increased in a nonlinear fashion as a function of input numbers with a sharp jump-like increase occurring at one particular input number (threshold = 9.8 ± 1.4 inputs; range 5-18; $n=12$ cells; **Fig. 26A**), after which they continued to increase at a slower rate with each extra input (**Fig. 26A**). The corresponding somatic voltage response mirrored the Ca^{2+} -responses, as a step-like increase of the EPSP amplitude occurred at the same threshold input number (**Fig. 26B**), after which the amplitude continued to increase at a slower rate. The occurrence of nonlinearity was also reflected by a sudden increase in the late component of the first derivate of EPSPs ($\delta V/\delta t$; **Fig. 26B Inset**).

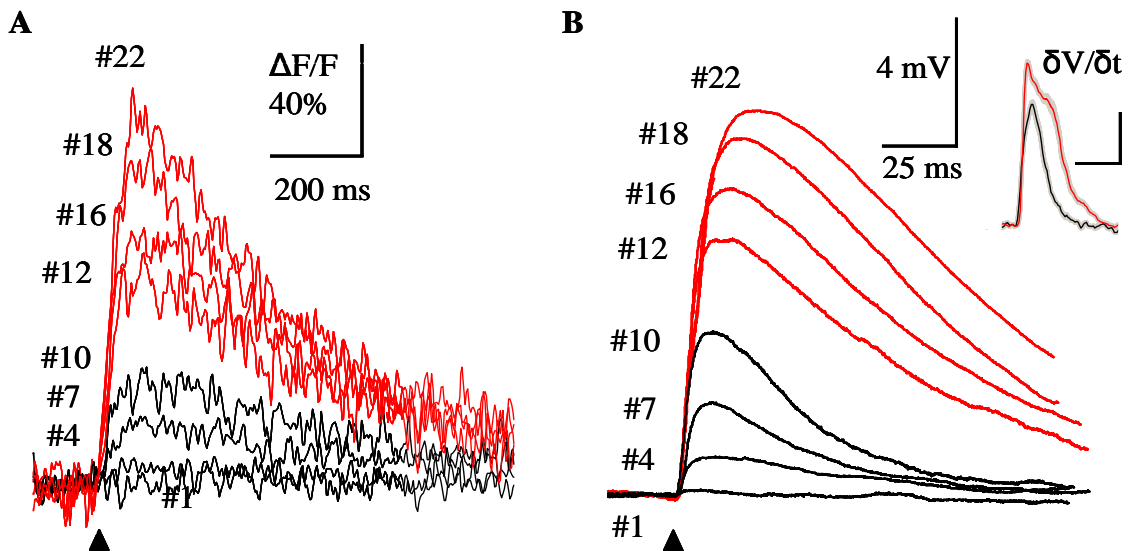


Figure 26 – Gradual increase of stimulated input numbers.

A) Ca^{2+} -transients derived at the peak of the 3D Ca^{2+} -responses produced by the clustered uncaging pattern at a progressively increasing number of inputs. **B)** Somatic recorded gluEPSPs associated with the 3D Ca^{2+} -responses in **(A)**. *Inset*, Averaged first derivate of near threshold gluEPSPs (subthreshold: *black trace*; suprathreshold: *red trace*). Scale bars: 0.5 mV/ms, 10 ms.

The nonlinear response pattern could well be followed on multiple cells (**Fig. 27A, C**). We plotted the normalized Ca^{2+} -responses aligned to the threshold of the nonlinear, step like increase for the clustered inputs, and a sigmoid-shaped input-output curve began to emerge (**Fig. 27B**). The same pattern could be observed for the somatically recorded EPSPs when plotting the responses in the function of stimulated

site number (**Fig. 27D**). The EPSP responses could be aligned to the threshold values determined from the Ca^{2+} -traces, and produced a similar sigmoid input-output curve.

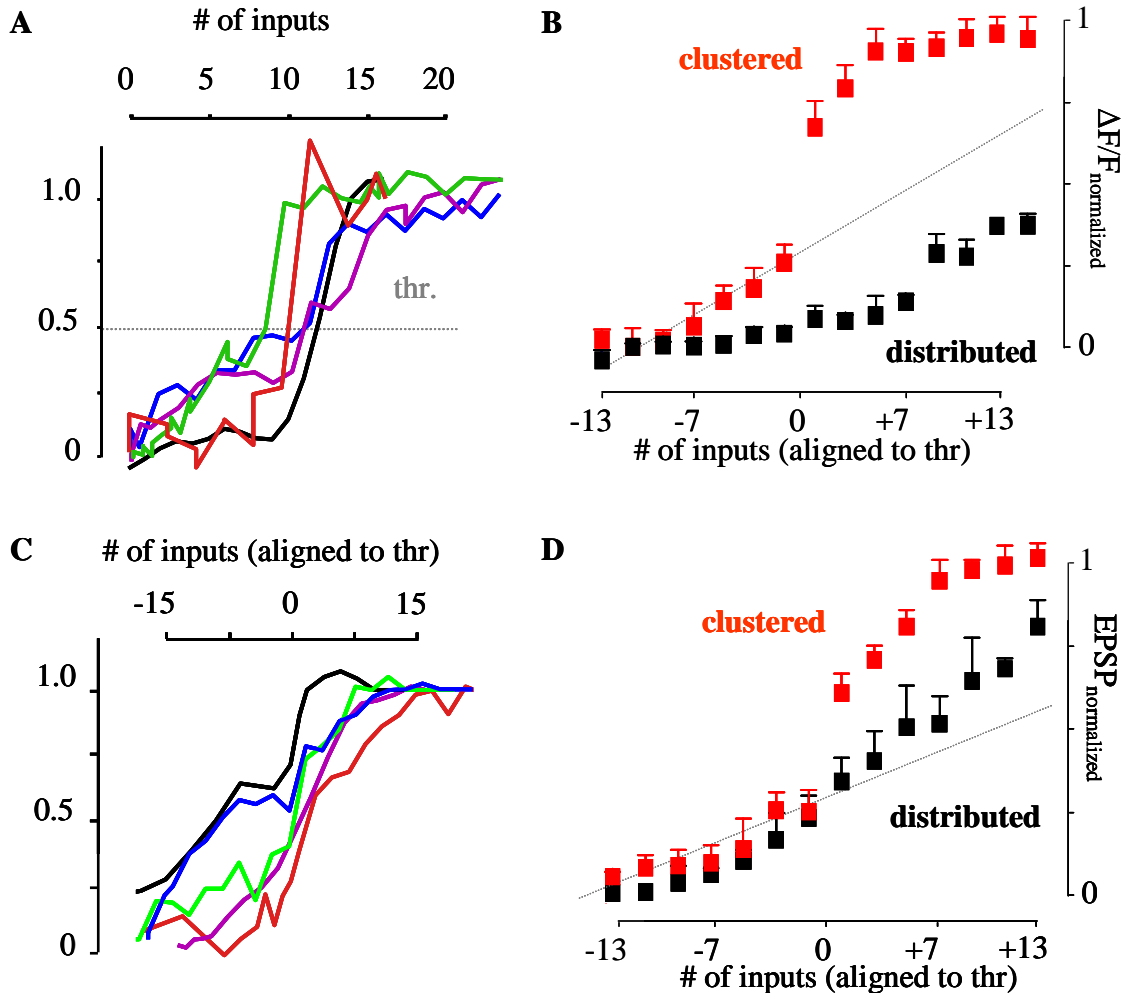


Figure 27 – Nonlinear increase of responses follows linear increase of stimulated input numbers.

A) Representative peak 3D Ca^{2+} -responses following normalization versus number of inputs (*clustered*) in individual cells. *thr*: threshold level of nonlinear increase. **B)** Summary plot of the threshold- (*thr*) aligned, normalized peak 3D Ca^{2+} -responses versus relative number of inputs for clustered (mean \pm s.e.m., n=14 cells), distributed input patterns. *Gray dotted line* shows linear fit to subthreshold values. **C-D)** Same as in **(A-B)**, respectively, but for the simultaneously recorded gluEPSPs. During alignment the same threshold values, determined for the Ca^{2+} -responses in **(B)**, were consequently used for the corresponding somatic voltage responses.

Is the tight clustering of inputs necessary for their nonlinear interactions, or can they be spread across long dendritic segments? To answer this question, we repeated the above experiments with distributed input patterns (**Fig. 25A**). In contrast to the sharp sigmoid input-output relation produced by clustered inputs, distributed inputs produced transients and voltage traces of lesser amplitude. When gradually increasing the number of inputs stimulated by the local two-photon photoactivation of glutamate, this resulted in a slowly increasing, more linear input-output relationship (**Fig. 27**). The linear increase was evident when considering both Ca^{2+} -transients (**Fig. 27B**) and somatic voltage traces (**Fig. 27D**). Here, voltage traces lacked the “depolarizing shoulder” – an increase in the decay after the peak of the voltage trace –, which was characteristic for the spatially clustered and temporally synchronized input pattern activation (**Fig. 26B**). The depolarizing shoulder gave a waveform vastly similar to dendritic regenerative events – dendritic spikes (dSpikes) – shown previously in pyramidal cell dendrites (Schiller et al. 2000; Losonczy and Magee 2006; Losonczy et al. 2008; Larkum et al. 2009).

The summarized plot of our data depicts seven characteristics in which the EPSPs below threshold were significantly different from the dSpikes above the determined threshold (**Fig. 28**).

Therefore, our data show that in contrast to pyramidal cells (Losonczy and Magee 2006; Losonczy et al. 2008), differently distributed input patterns are not equivalent within the same dendritic branch. That is, individual branches in interneurons do not function as single integrative compartments, but rather a spatial clustering of inputs below the level of individual dendritic branches (computational subunits) is required.

These data show two components of the Ca^{2+} - and simultaneously recorded membrane transient summation produced by clustered inputs. The first is a relatively smaller, linear summation of the inputs reproduced by distributed input patterns, onto which a second, step-like increase was superimposed as a consequence of the nonlinear spatial interaction of the inputs generating dSpikes (**Fig. 27B, D**).

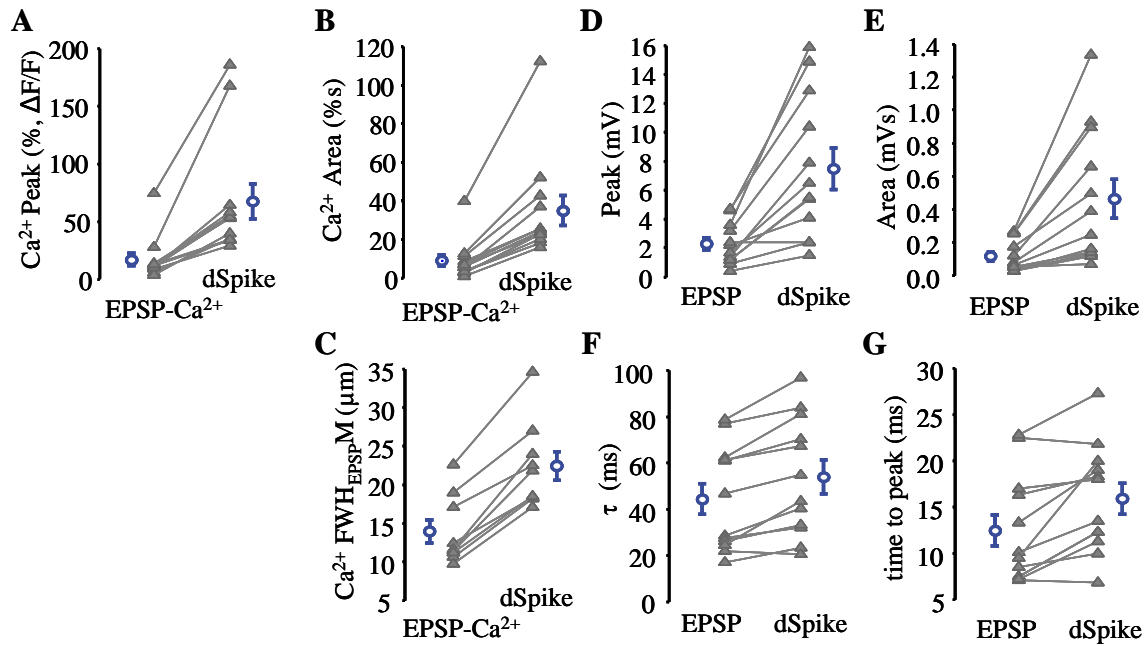


Figure 28 – Uncaging-evoked responses point to two distinct response types.

Uncaging-evoked EPSP (from threshold–8 to threshold+4) and dSpike (from threshold+4 to threshold+8) responses differed in **A**) amplitude (EPSP- Ca_{peak} : 17.1 ± 5.5 % , dSpike $_{\text{peak}}$: 67.5 ± 15.1 % , $p = 0.0007$), **B**) area (EPSP- Ca_{area} : 8.9 ± 3.0 %•s, dSpike $_{\text{area}}$: 34.9 ± 7.7 %•s, $p = 0.0002$), and **C**) the full width at half EPSP maximum (EPSP- $\text{CaFWH}_{\text{EPSPM}}$: 12.3 ± 1.2 μm , dSpike $\text{FWH}_{\text{EPSPM}}$: 19.9 ± 1.5 μm , $p = 0.00002$) of the 3D Ca^{2+} -response, as well as **D**) the peak (EPSP $_{\text{peak}}$: 2.3 ± 0.4 mV, dSpike $_{\text{peak}}$: 7.5 ± 1.4 mV, $p = 0.0007$) **E**) the area (EPSP $_{\text{area}}$: 0.12 ± 0.03 mVs, dSpike $_{\text{area}}$: 0.46 ± 0.12 mVs, $p = 0.003$), **F**) decay time constant ($\tau_{\text{EPSP-Ca}}$: 44.4 ± 6.5 ms, τ_{dSpike} : 53.9 ± 7.4 ms, $p = 0.0003$) and **G**) time to peak of the EPSPs (t_{EPSP} : 12.4 ± 1.7 ms, t_{dSpike} : 15.9 ± 1.7 ms, $p = 0.003$) were significantly larger for the dSpike cluster (12 cells). Individual cells in *grey*, mean \pm s.e.m in *blue*.

VII.2. Active Dendrites in CA1 Str. Rad. Interneurons

The spatial and temporal coincidence detection in dendrites is usually manifested in the appearance of regenerative dendritic action potentials - dendritic spikes (Sjostrom et al. 2008). The above results led us to explore whether the nonlinear signal integration in dendrites of CA1 str. rad – LM interneurons peak in dendritic spikes. To investigate, we first used stimulation of the Shaffer collaterals from region CA3 to induce EPSPs in RAD-LM interneuron dendrites (**Fig. 29A**). The use of 2P imaging allowed the identification of the input sites, and whole-cell patch clamped EPSPs could be recorded at the soma. To compare the stimulation-evoked and spontaneous EPSPs, we took advantage of a newly developed submerged recording chamber with double superfusion for increased oxygenation of the sample. Rat brain slices used were 450- to 600- μm -thick to have a more preserved network of axons. The higher oxygenation lead to increased spontaneous activity similar to that observed under *in vivo* conditions (**Fig. 29B**).

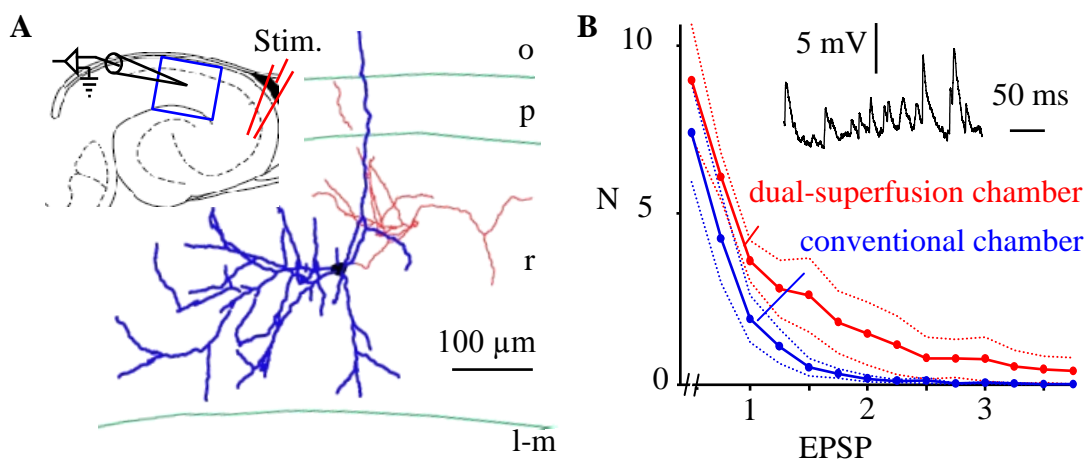


Figure 29 – Recording in a dual-superfusion slice chamber.

A) Scheme showing the measurement protocol for Shaffer collateral stimulation (*inset*) with one of the reconstructed neurons (*blue*: dendrites; *red*: axons). **B)** Amplitude distributions of EPSPs recorded from CA1 interneurons (30 s/cell) in conventional (*blue*, $n = 9$ cells) and dual-superfusion slice chamber (*red*, $n = 11$ cells) were significantly different (Kolmogorov–Smirnov test, $P < 0.001$). Note the high incidence of EPSPs on the representative voltage trace (*inset*).

Input sites for spontaneously occurring excitatory potentials were identified after scanning arbitrary regions on a dendritic tree of an OGB-1 filled CA1 RAD-LM interneuron (**Fig. 30A**) by systematically scanning the dendritic tree until we found an input site.

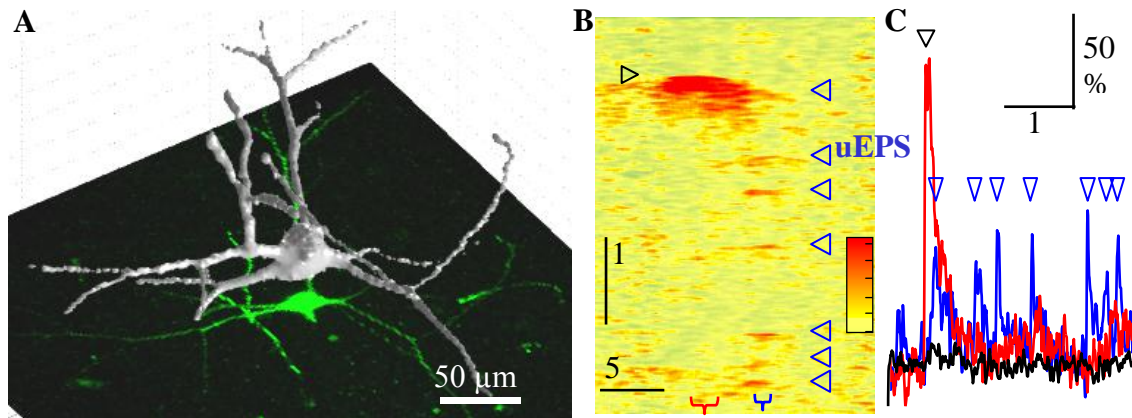


Figure 30 – Spontaneous dendritic Ca^{2+} -responses.

A) Maximum intensity projection and surface rendered view of a CA1 interneuron.

B) Dendritic Ca^{2+} -trace for presumable spontaneous dendritic spikes (*black empty arrowhead*) and a barrage of spontaneous EPSPs (*blue empty arrowheads*). Color bar: 0–63% $\Delta\text{F}/\text{F}$.

C) Corresponding Ca^{2+} -transients.

In the first group, 3D Ca^{2+} responses (spatially normalized and projected Ca^{2+} transients measured along the 3D trajectory) were relatively small ($22 \pm 2\% \Delta\text{F}/\text{F}$; $n = 9$ cells) and had a narrow spatial distribution ($5.2 \pm 0.9 \mu\text{m}$), consistent with properties characteristic of a single or few inputs (group noted as excitatory postsynaptic potential (EPSP)- Ca^{2+} and EPSP in **Fig. 31**) (Goldberg et al. 2003a; Goldberg et al. 2003b; Rozsa et al. 2004; Topolnik et al. 2009). Here, very restricted 3D Ca^{2+} responses were also revealed (FWHM, $2.60 \pm 0.48 \mu\text{m}$; decay time constant, $63.9 \pm 6 \text{ ms}$; rise time, $6.13 \pm 1.13 \text{ ms}$; noted as unitary EPSP (uEPSP)- Ca^{2+} on **Fig. 31**). EPSPs of small, possibly unitary amplitude accompanied uEPSP- Ca^{2+} s (uEPSP, $0.55 \pm 0.12 \text{ mV}$; $n = 8$ cells; **Fig. 31D**). In contrast to EPSP- Ca^{2+} , the second group consisted of 3D Ca^{2+} responses that were larger ($51 \pm 8\% \Delta\text{F}/\text{F}$; $P = 0.005$; $n = 9$ cells), and had a broader spatial distribution ($13.6 \pm 2.4 \mu\text{m}$; $P = 0.003$), in agreement with properties characteristic of

local dSpikes (**Fig. 31**) (Schiller et al. 2000; Antic et al. 2010). The decay time of postsynaptic potentials underlying dSpikes was more prolonged compared with EPSPs (EPSP, 22.8 ± 5.8 ms; dSpikes, 79.7 ± 23.8 ms; $P = 0.02$) and area increased by $314 \pm 57\%$ ($P = 0.007$; $n = 9$; **Fig 31B**), more than expected from the amplitude difference (EPSP, 2.2 ± 0.7 mV; range, 0.77–7.97 mV; dSpikes, 4.9 ± 1.5 mV; range, 1.59–15.37 mV; amplitude increased by $267 \pm 59\%$; $P = 0.02$; $n = 9$).

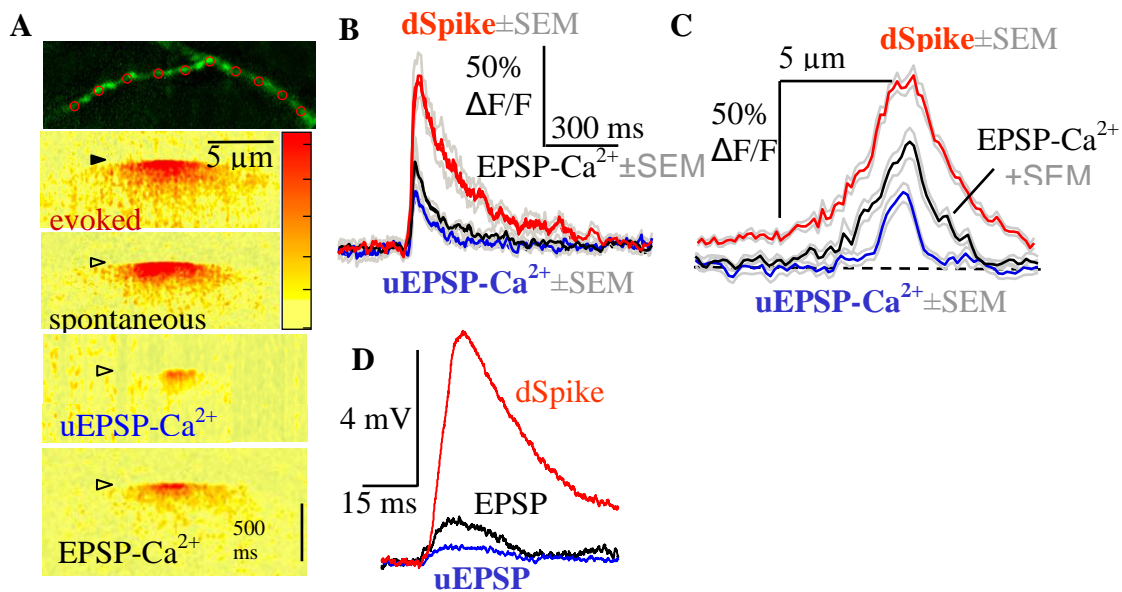


Figure 31 – Evoked and spontaneous dendritic responses.

A) A representative dendritic segment of the interneuron depicted on **Figure 30A** and the spontaneous and evoked dendritic Ca^{2+} -responses recorded. Color bar: 0–63% $\Delta\text{F}/\text{F}$. **B)** Ca^{2+} transients (average of five to seven traces) derived at the peak of the 3D Ca^{2+} -responses in A. **C)** Spatial distribution of peak 3D Ca^{2+} -responses in A. **D)** Corresponding somatic membrane voltage. *Gray traces* show mean \pm SEM.

Next, our aim was to underline that larger events were correctly identified as dSpikes by evoking responses using focal electrical stimulation. We first induced EPSPs (8.9 ± 1.9 mV) in a conventional recording chamber while imaging thin second- and third order dendrites (0.8 ± 0.06 μm in diameter) in 3D (**Fig. 32A**). Low stimulation intensities induced relatively stable and small amplitude 3D Ca^{2+} responses, which were accompanied by rapid membrane potential transients similar to the spontaneous EPSPs

detailed earlier (**Fig. 32B-D**). When we increased the stimulation intensity, the type of evoked responses greatly depended on stimulation intensity (**Fig. 32C**): higher stimuli in some cases induced dSpike-like responses, with an elongated decay time both 3D Ca^{2+} -traces and somatic voltage traces.

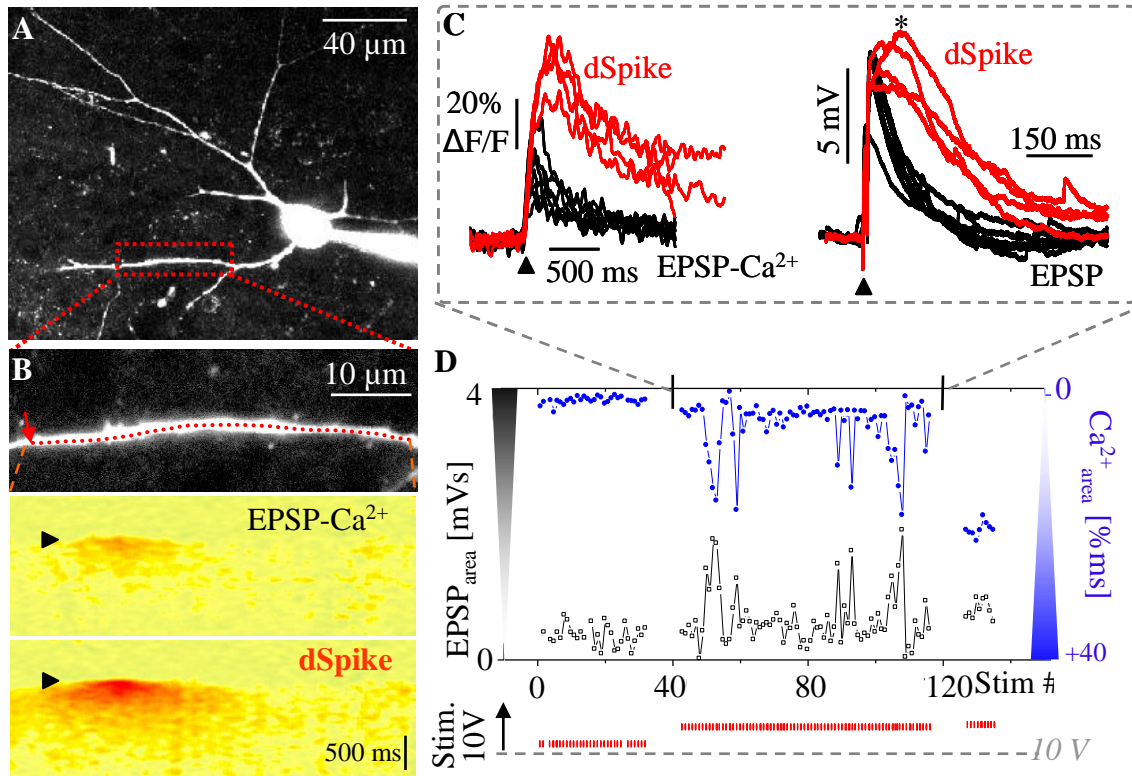


Figure 32 – Evoked dendritic responses.

A) Maximum intensity image stack projection of a CA1 interneuron. **B)** Near AP threshold 3D Ca^{2+} responses induced by focal synaptic stimulation showing two characteristic states, EPSP- Ca^{2+} and dSpike. **C)** Successive Ca^{2+} -transients derived at the peak of the 3D Ca^{2+} -responses in **B** show that responses alternated between the two states (EPSP- Ca^{2+} and dSpike). (*Right*) Corresponding membrane potentials. *Asterisk* marks the depolarizing shoulders. **D)** Magnitude of Ca^{2+} and voltage responses at subthreshold, near AP threshold and at suprathreshold stimulus intensities. *Gray dashed lines* indicate the interval of the alternating responses shown in **C**. (*Bottom*) Peak voltage of stimulus pulses.

The separation of the different groups was not always evident from the simple analysis or visual observation. On **Figure 33**, traces are presented that could hardly be put in any of the groups by simple visual observation or by analyzing the amplitudes or decay times of the somatic voltage traces.

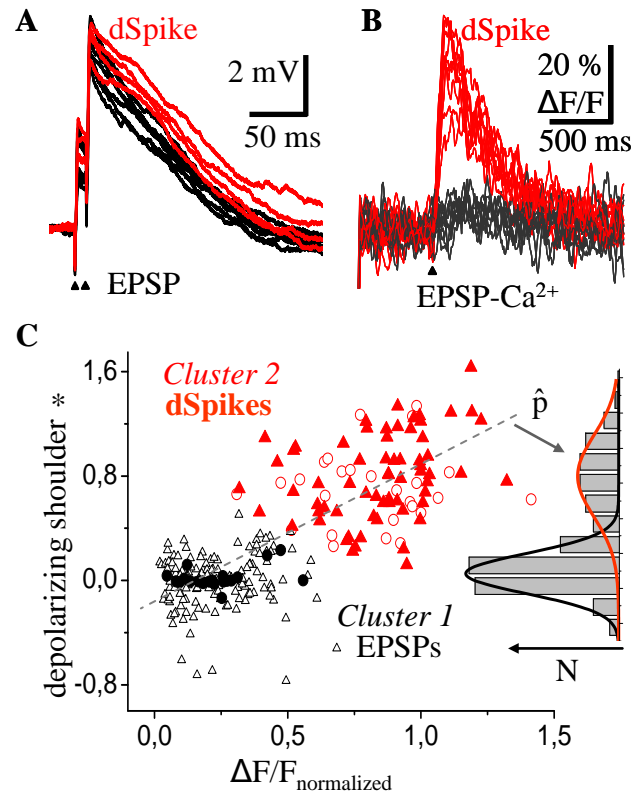


Figure 33 – Separation of the responses.

A-B) Somatic membrane potentials and corresponding Ca^{2+} -transients of dSpikes (red traces) and EPSPs (black traces) as in **Fig. 32C**, but from a different cell. In this representative example dSpikes are clearly different with Ca^{2+} -imaging, but are barely distinguishable in the somatic recording, showing that the simultaneous analysis of Ca^{2+} -transients and voltage traces were required for dSpike separation. **C)** Method of dSpike separation for spontaneous (measured in double perfusion chamber) and evoked responses. The average of monocomponent EPSPs was subtracted from individual EPSPs, the results were integrated, normalized (depolarizing shoulder) and plotted against normalized peak 3D Ca^{2+} -responses ($n = 19$ cells). Analysis yielded two clusters of EPSPs and dSpikes both for spontaneous and evoked responses: (triangles: evoked, circles: spontaneous). *Right:* Histogram shows the projection to linear-fitted axis.

Here, the increased “depolarizing shoulder” characteristic of dSpikes that is usually observable in the decaying phase of the traces is barely visible (**Fig. 33A**), though the separation of different groups is readily applicable based on the dendritic Ca^{2+} -imaging (**Fig. 33B**). Nevertheless, the separation of the two groups was confirmed through cluster analysis (cluster1: EPSPs, cluster2: dSpikes; **Fig. 33C**). The average 3D Ca^{2+} -response amplitudes and EPSP areas determined for the two clusters in individual cells were significantly different (EPSP- $\text{Ca}^{2+}_{\text{peak}}$: 18.0 ± 3.2 % $\Delta\text{F}/\text{F}$, dSpike $_{\text{peak}}$: 53.8 ± 8.1 % $\Delta\text{F}/\text{F}$, $p = 0.0001$; EPSP $_{\text{area}}$: 0.57 ± 0.12 mVs, dSpike $_{\text{area}}$: 1.06 ± 0.18 mVs, $p < 10^{-4}$, $n = 19$ cells; **Fig. 33C**). Further investigation revealed that the cluster of dSpikes showed significantly larger values in five additional parameters ($n = 19$ cells; **Fig. 34**). Namely, in amplitude (EPSP- Ca_{peak} : 18.0 ± 3.2 % , dSpike $_{\text{peak}}$: 53.8 ± 8.2 % , $p = 0.0001$), area (EPSP- Ca_{area} : 13.5 ± 2.3 %•s, dSpike $_{\text{area}}$: 45.6 ± 8.1 %•s, $p = 0.0001$) and full width at half EPSP maximum (EPSP- $\text{Ca}^{2+}\text{FWH}_{\text{EPSPM}}$: 8.1 ± 0.9 μm , dSpike $\text{FWH}_{\text{EPSPM}}$: 19.0 ± 2.6 , $p = 0.001$) of the 3D Ca^{2+} -response, as well as the area (EPSP $_{\text{area}}$: 0.57 ± 0.12 mVs, dSpike $_{\text{area}}$: 1.06 ± 0.18 mVs, $p = 0.0001$), time to peak (t_{EPSP} : 5.3 ± 0.9 ms, t_{dSpike} : 19.1 ± 4.0 ms, $p = 0.002$), decay time constant ($\tau_{\text{EPSP-Ca}}$: 79.3 ± 4.2 ms, τ_{dSpike} : 123.5 ± 12.8 ms, $p = 0.001$) and peak of EPSPs (EPSP $_{\text{peak}}$: 8.9 ± 1.9 mV, dSpike $_{\text{peak}}$: 11.7 ± 2.1 mV, $p = 0.0004$) were significantly larger for the dSpike cluster ($n = 19$ cells).

The cluster analysis method repeated on the spontaneous responses recorded in the dual-perfusion slice chamber (**Fig. 11**) confirmed the presence of the previously identified groups (dSpikes and EPSPs, **Fig. 34C** and **Fig. 34D**). Similarly to the evoked events, we found a significant difference in the seven parameters for spontaneous dSpikes compared to spontaneous single or few input-evoked events ($n=9$ cells). Namely, spontaneous EPSP and dSpike responses differed in amplitude (EPSP- Ca_{peak} : 22.3 ± 2.5 % , dSpike $_{\text{peak}}$: 50.7 ± 7.9 % , $p = 0.005$), area (EPSP- Ca_{area} : 6.0 ± 1.6 %•s, dSpike $_{\text{area}}$: 16.1 ± 3.9 %•s, $p = 0.02$), and the full width at half EPSP maximum (EPSP- $\text{Ca}^{2+}\text{FWH}_{\text{EPSPM}}$: 5.2 ± 0.9 μm , dSpike $\text{FWH}_{\text{EPSPM}}$: 13.6 ± 2.4 μm , $p = 0.003$) of the 3D Ca^{2+} -response, as well as the area (EPSP $_{\text{area}}$: 0.09 ± 0.04 mVs, dSpike $_{\text{area}}$: 0.51 ± 0.25 mVs, $p < 0.05$), time to peak (t_{EPSP} : 3.0 ± 0.2 ms, t_{dSpike} : 17.5 ± 5.2 ms, $p = 0.03$), decay time constant ($\tau_{\text{EPSP-Ca}}$: 22.8 ± 5.8 ms, τ_{dSpike} : 79.7 ± 23.8 ms, $p = 0.02$) and peak of the EPSPs (EPSP $_{\text{peak}}$: 2.2 ± 0.7 mV, dSpike $_{\text{peak}}$: 4.9 ± 1.5 mV, $p = 0.02$) were significantly larger for the dSpike cluster ($n=9$ cells).

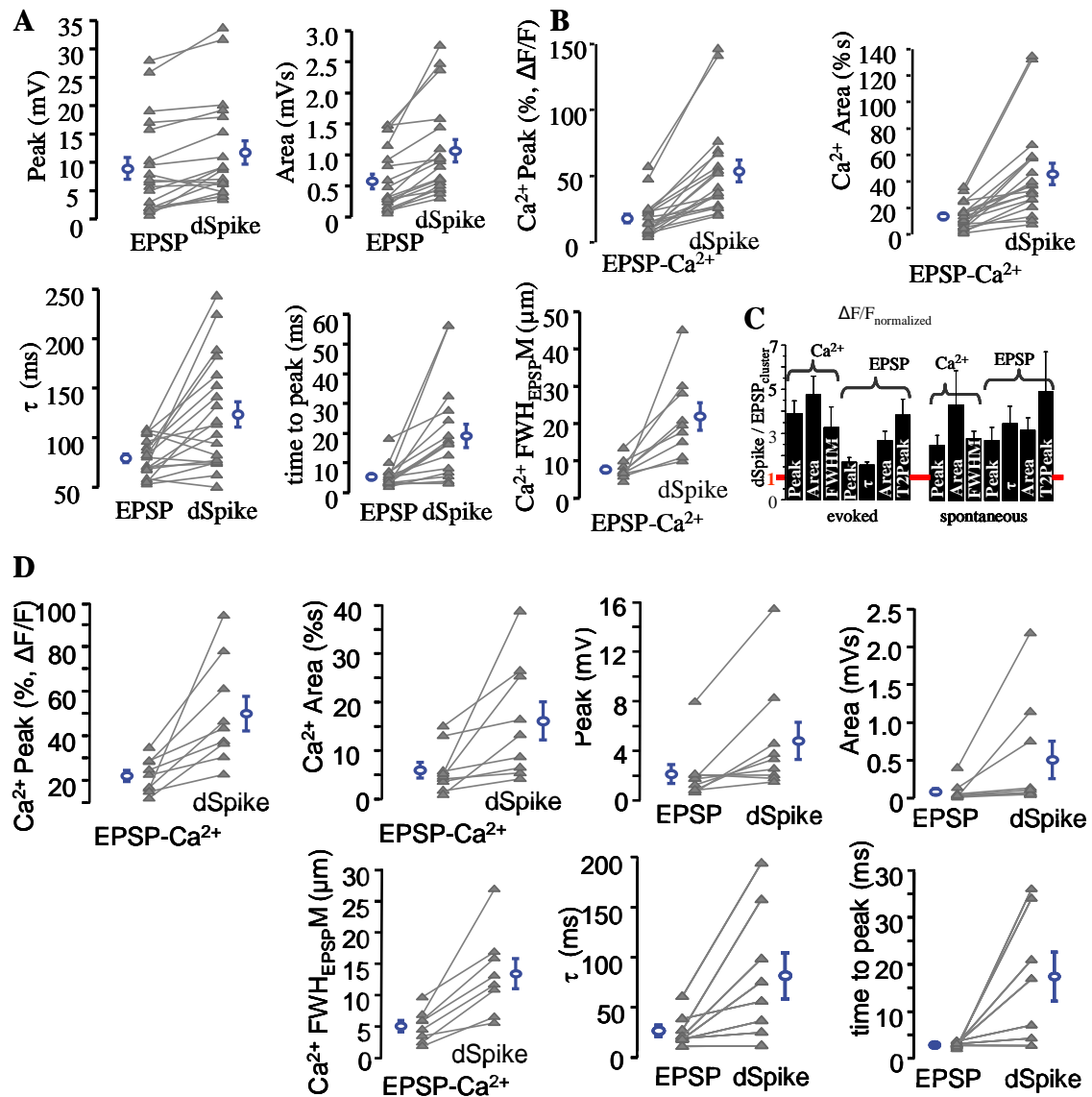


Figure 34 – Characteristics of spontaneous and evoked EPSPs and dSpikes.

A-B) When grouped by cluster analysis, evoked dSpike and EPSP responses differed significantly in seven parameters. **C)** Ratio of parameters characterizing the two clusters for evoked (*left*) and spontaneous (*right*) events (*FWHM* - full width at half maximum; τ - decay time constant; *T2Peak*: time to peak). **D)** Spontaneous EPSP and dSpike characteristics. Individual cells in grey, mean \pm s.e.m. in blue. See main text for corresponding data.

VII.3. Channels Taking Part in Synaptic Processing

VII.3.1. N-methyl-D-aspartate Receptors (NMDAR)

Based on the waveforms of both somatic voltage traces and dendritic Ca^{2+} -transients, we presumed that the responses with a “depolarizing shoulder” and increased decay times were dendritic spikes.

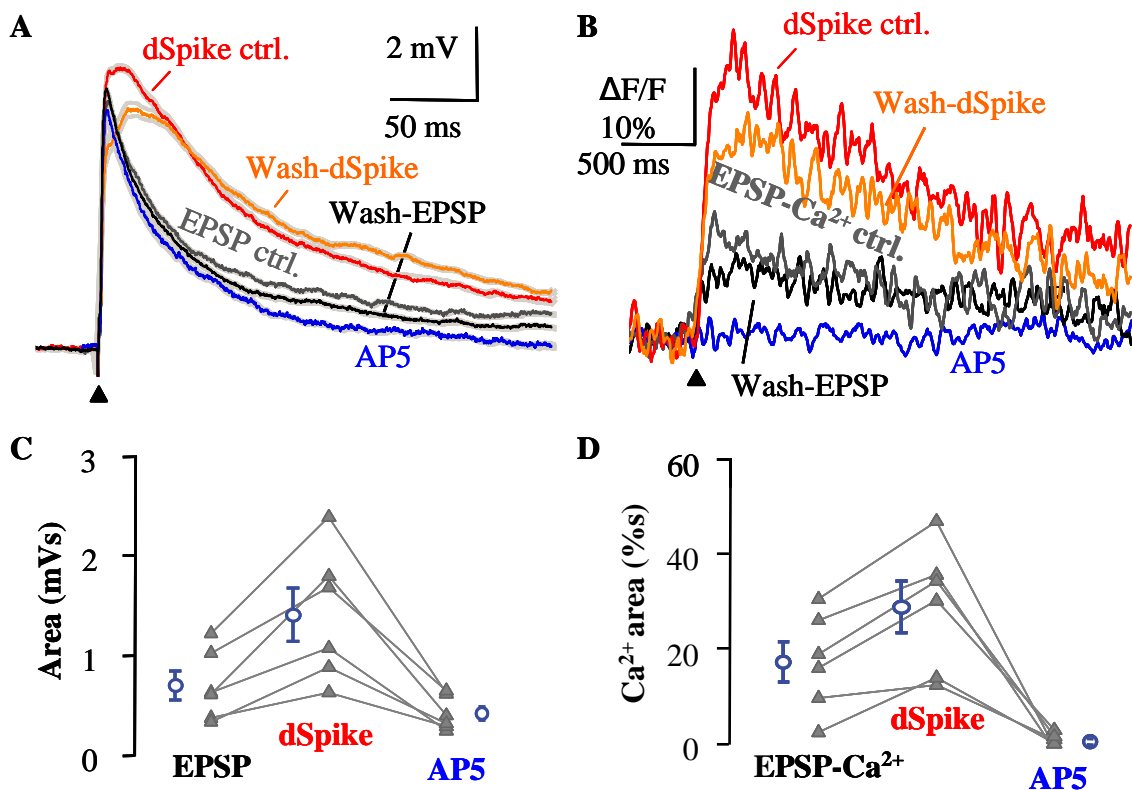


Figure 35 – Dendritic spikes in interneurons are NMDA-spikes.

A-B) Somatic membrane potentials (**A**) and corresponding Ca^{2+} transients (**B**) prior to (*red* and *dark gray* traces are averages of the two clusters), in the presence of the NMDA receptor antagonist AP5 ($60\ \mu\text{M}$; *blue* trace) and after washout (*orange* and *black* traces). *Gray* traces show mean \pm s.e.m. Note that dSpikes occur in control and wash-out, but disappeared in AP5. **C)** Area of somatic voltage traces in control conditions (EPSPs and dSpikes) and in the presence of AP5 ($60\ \mu\text{M}$) ($n = 6$ cells). **D)** area of corresponding 3D Ca^{2+} responses. *Grey triangles*: individual cells; *blue circles* with error bars: mean \pm s.e.m. of pooled data. EPSPs, dSpikes and responses in the presence of NMDAR blockade were significantly different ($p < 0.05$)

To characterize these dSpikes in a more detailed manner, we turned to pharmacology. Based on previous data (Schiller et al. 2000; Maccaferri and Dingledine 2002), we hypothesized that both features are due to the activation of N-methyl-D-aspartate (NMDA) receptors. To verify this, we used the NMDAR antagonist AP5 (60 μM) while applying focal electrical stimulation. The antagonist completely eradicated the depolarizing shoulder on somatic voltage traces, leaving only a response that resembled AMPA-receptor responses (**Fig. 35A, C**). At the same time, the dendritic Ca^{2+} -imaging showed that AP5 caused a complete loss of Ca^{2+} -signals at the dendrites (**Fig. 35B, D**). Returning to control conditions by wash-out of the drug AP5 and wash-in of normal ACSF yielded similar responses to control, where the dendritic spikes reappeared on both the voltage (**Fig. 35A, C**) and Ca^{2+} -traces (**Fig. 35B, D**).

To underline the involvement of NMDA-receptors in dSpike generation, we again turned to two-photon photoactivation of Glutamate. Here, we applied uncaging laser pulses at clustered points along the interneuron dendrite (**Fig. 25A**) as a control measurement, and then we added AP5 (60 μM) in the bath. The process helped us to examine how the dSpikes evoked by the activation of a cluster of inputs is affected by the block of NMDA-receptors (**Fig. 36**).

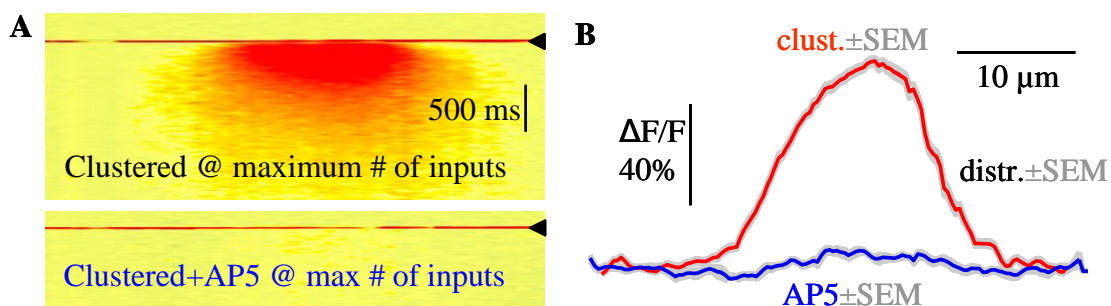


Figure 36 – NMDA-receptors are involved in dSpike generation.

A) Ca^{2+} -transient recorded at an interneuron dendrite after photoactivation of Glutamate at a cluster of input sites. *Bottom*, same activated cluster of inputs shows no Ca^{2+} -responses after adding the NMDA-receptor antagonist AP5 (60 μM) to the bath. *Black arrowhead*: stimulation by uncaging of DNI-Glutamate. **B)** Spatial distribution of the Ca^{2+} -responses recorded in (**A**).

We first activated a high number of inputs in a clustered manner (see **Fig. 25** for the measurement protocol). As shown on **Figure 36**, the application of the NMDA-receptor antagonist AP5 almost completely abolished the dendritic Ca^{2+} -responses. We then compared the clustered results along with the data received when we aligned the same number of uncaging points as used in the clustered arrangement in a distributed manner, increasing the inter-input distance. The analysis showed that the effect of AP5 was more prominent than the spatial unclustering of inputs (**Fig. 37**). When comparing the Ca^{2+} -responses, the inputs placed in a large number but in a distributed manner showed a well-defined and easily observable Ca^{2+} -response. The decrease could be observed even on the single measurement Ca^{2+} -traces, and showed obviously on the averaged responses. On the other hand, the wash-in of AP5 gave a minor, barely observable Ca^{2+} -response (**Fig. 37A**).

As before, the somatic voltage traces recorded simultaneously with the dendritic Ca^{2+} -responses showed a depolarizing shoulder for the clustered inputs (**Fig. 37B**), which disappeared for the distributed input pattern. Nevertheless, the application of AP5 could further decrease the full width at half maximum of the responses, even when compared with the distributed input pattern responses ($p < 0.01$; **Fig. 37C**). Though the tendency for the decrease is clear even to the naked eye, the normalization of the values to the increased full width at half maximum of the clustered input pattern arising from the characteristic depolarizing shoulder of the dSpikes showed a clear decrease when simply distributing the activation of inputs or by the application of AP5 (**Fig. 37C**).

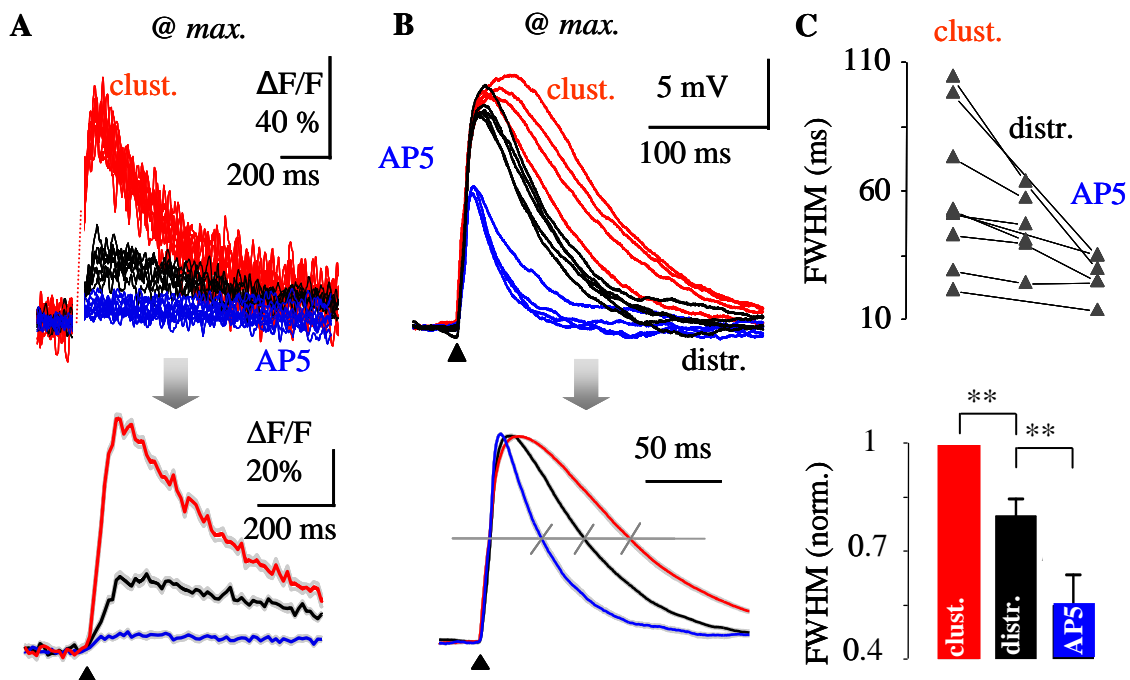


Figure 37 – Involvement of NMDA-receptors in supralinear signal integration.

Uncaging evoked responses in the interneuron shown in **Figure 25**. **A) Top**, Single uncaging-evoked Ca²⁺-transients at the maximum input number for clustered (*red*) and distributed (*black*) input patterns. AP5 decreased responses for clustered inputs (*blue*). **Bottom**, Corresponding average Ca²⁺-transients. *Gray traces* show mean \pm s.e.m. **B) Top**, Somatically recorded gluEPSPs associated with the Ca²⁺-transients in (**A**). **Bottom**, Corresponding averaged and normalized gluEPSPs. *Gray lines* indicate different half-width. **C) Top**, Half-width of normalized EPSPs in individual cells. **Bottom**, Relative difference of gluEPSP half-width when compared to the clustered input pattern induced responses. Bar graphs show mean \pm s.e.m. *Black arrowhead*: two-photon uncaging stimulus. ** $p < 0.01$

We have proven above that gradually increasing the number of activated inputs in a cluster causes supralinear summation of both Ca²⁺- and somatic voltage responses (**Fig. 27**). To examine the possible mechanism of such an increase, we designed a protocol based on our results with the NMDA-receptor antagonist AP5 (**Fig. 38**; **Fig. 37**). Blockade of NMDA-receptors reduced the 3D Ca²⁺-transients produced by clustered inputs by a factor of ~ 9 (**Fig. 37**) and switched the summation from sigmoid to linear (**Fig. 38A**). Corresponding EPSPs were more moderately (factor of ~ 2 -3)

reduced in amplitude and their decay time constants were shorter (**Fig. 37B**), analogous to the results of the previous experiments using focal electric stimulation (**Fig. 35A**).

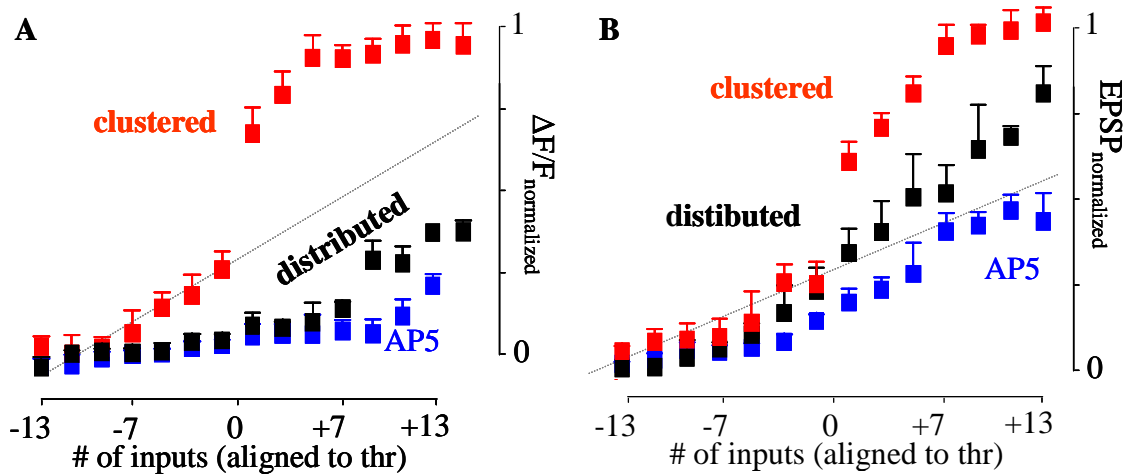


Figure 38 – Involvement of NMDA-receptors in the supralinear signal integration.

A) Summary plot of the threshold- (*thr*) aligned, normalized peak 3D Ca²⁺-responses versus relative number of inputs for clustered (mean±s.e.m., n=14 cells) input patterns and for clustered inputs in the presence of AP5 (n=6 cells). *Gray dotted line* shows linear fit to subthreshold values. **B)** Same as **(A)**, but for the simultaneously recorded gluEPSPs. During alignment the same threshold values, determined for the Ca²⁺-responses in **(A)**, were consequently used for the corresponding somatic voltage responses.

The input-output function of EPSPs has also switched from sigmoid to linear. Ca²⁺- (and simultaneously recorded membrane transient) amplitudes were significantly different in control conditions and in the presence of NMDA-receptor blockade even down to threshold minus 7 inputs, showing a non-zero contribution of NMDA receptors below threshold ($p < 0.05$, $n = 6$; **Fig. 38**).

Next, we wished to gather further evidence that by changing the milieu for NMDA-channel activation, the responses that we deemed as dSpikes are changed as well. It is well-described that the heteromeric NMDA-receptors are cation channels allowing the inward flow of Ca²⁺ and Na⁺ and the outward flow of K⁺ (Purves 2008). As an internal regulation mechanism, Magnesium ions are well-known to inhibit NMDA

receptors by blocking the pore of the channel (Nowak et al. 1984; Paoletti and Neyton 2007). When the neuron gets depolarized, the Mg^{2+} -block is released and NMDA-receptors can be unblocked. The release of the Mg^{2+} -block plays a significant role in synaptic plasticity processes such as long term potentiation by allowing the second messenger Ca^{2+} to enter the dendrite or spine (Murphy et al. 1997). To see whether the unblocking of NMDA-receptors affect the nature of the dSpikes we found, we used Mg^{2+} -free ACSF while applying focal electrical stimulation.

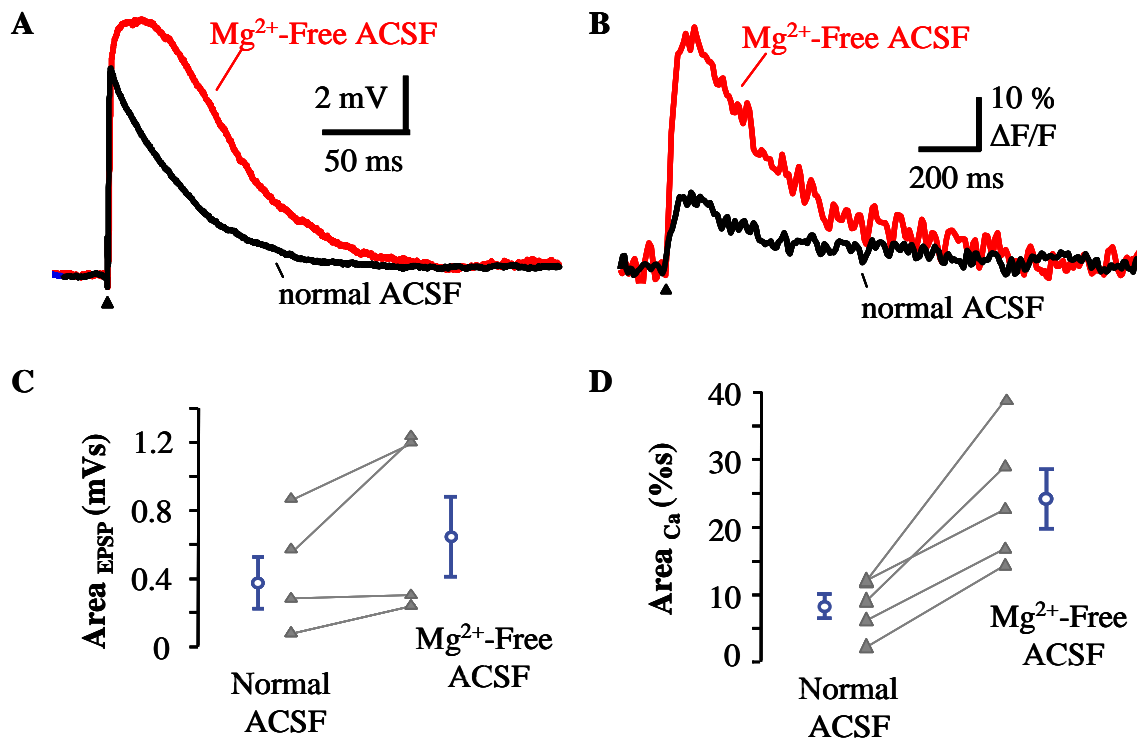


Figure 39 – Effects of Mg^{2+} -removal.

A-B) Somatic membrane transients (**A**) and corresponding Ca^{2+} transients (**B**) in the presence of Mg^{2+} -free ACSF and normal ACSF. **C-D)** Areas of somatic membrane potential traces (**C**) and Ca^{2+} -responses (**D**) averaged for normal and Mg^{2+} -free ACSF were significantly different ($p < 0.05$). Individual cells in grey, mean \pm s.e.m. in blue.

Here, the Mg^{2+} -block of the receptors is naturally released as the wash-in of Mg^{2+} -free ACSF occurs, and the complete effect of the channels can be monitored. As expected from our previous results, the removal of Mg^{2+} provided somatic voltage

responses with an extremely elongated depolarizing shoulder (**Fig. 39A, C**), showing significant difference from control responses ($p < 0.05$, t-test). At the same time, the corresponding Ca^{2+} -responses recorded at the focal stimulation site on the dendrite showed increased area when compared to control ($p < 0.05$, t-test; **Fig. 39B,D**). These data bear great resemblance to those we observed when scanning for spontaneous responses (compare dSpike traces of **Fig. 35A** to **Fig. 39A**).

According to the above mentioned evidence, our data suggest that CA1 interneuron dendrites display similar dSpikes to those observed in pyramidal cell dendrites (Schiller et al. 2000; Poirazi et al. 2003b; Losonczy and Magee 2006). Our pharmacological data suggest that the observed dendritic regenerative events are NMDA-spikes.

VII.3.2. Voltage-Gated Calcium Channels (VGCCs)

The dendritic responses recorded in pyramidal cells or interneurons many times point to the role of Ca^{2+} -permeable membrane channels, such as NMDA-receptors (Schiller et al. 2000; Maccaferri and Dingledine 2002), Ca^{2+} -permeable AMPA receptors (Matsuzaki et al. 2001; Goldberg et al. 2003b) and different types of voltage-gated Calcium channels (Losonczy and Magee 2006). The data mentioned above point to the role of NMDA-receptors that seemed to override any other type of Ca^{2+} -influx in magnitude: simply by blocking NMDA-receptors the Ca^{2+} -responses decreased to a minimal level. Nevertheless, these results did not show the exact activation sequence of channels. A possible case for the sequence of channel activation would be that – according to channel kinetics – Ca^{2+} -permeable AMPA receptors would open first, giving a trigger for other channels. Next, NMDA-receptors would open, along with VGCCs (Siegel 2006; Purves 2008). Since the blockade of NMDA-receptors diminished signals to a linear range, GluR2-containing AMPA-receptors could not have served as the source of the increased Ca^{2+} -influx. As a consequence, we turned to examine the role of VGCCs.

We used a cocktail of different blockers to affect all VGCC types that could modify signal integration properties in the dendrites of hippocampal CA1 interneurons. The blocking of the part of the Ca_v2 subfamily (N-, P/Q-type) was accomplished by

Mibefradil (50 μM), the Ca_v1 subfamily of (L-type) VGCCs was blocked by Nimodipine (20 μM), while $\text{Ca}_v2.2$ (N-type) VGCCs were blocked by ω -Conotoxin GVIA (5 μM). After applying the same stimulus protocol as for that of the studies on the NMDA-receptor function in signal integration, we used a gradual increase of activated synaptic site numbers to determine how the blockage of VGCCs affects signal integration. Our results show that – in contrast to NMDA receptor blockage –, the cocktail of VGCC blockers shifted the threshold and decreased peak amplitudes only slightly above the threshold for both the dendritic Ca^{2+} -responses (**Fig. 28B**) and the corresponding somatic voltage traces (**Fig. 28B**; see **Figure 38** for comparison). Subthreshold responses were not significantly different ($p>0.2$).

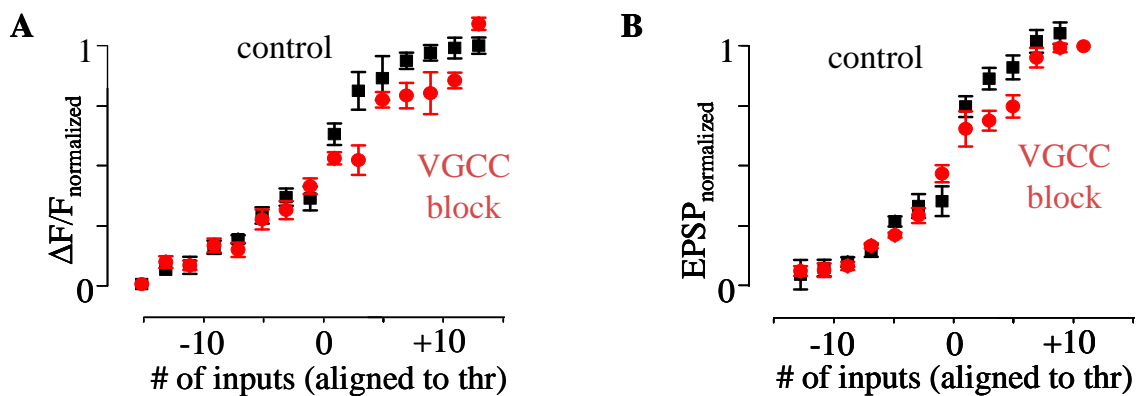


Figure 40 – VGCCs in signal integration of CA1 interneurons.

A) Summary plot of the threshold- (thr) aligned, normalized peak 3D Ca^{2+} -responses versus relative number of clustered inputs (mean \pm s.e.m., $n=5$ cells) in *control* conditions (*black squares*) and in the presence of a cocktail of voltage-gated Ca^{2+} channel blockers (*VGCC block: red circles*; Mibefradil, 50 μM , Nimodipine, 20 μM , ω -Conotoxin GVIA 5 μM). **B)** Same as **(A)**, but for peak somatic voltage responses.

VII.3.3. Voltage-Dependent Sodium Channels (Na_v)

Our aforementioned data showed that the regenerative events we observed in hippocampal CA1 interneuron dendrites were possibly NMDA-spikes, as AP5 decreased both the Ca^{2+} - and somatic voltage the responses to the linear regime. Furthermore, even by using blockage of VGCCs, the supralinearity of the responses remained nearly unaffected. However, we still could not determine whether the active

propagation of the signals was simply due to the NMDA-receptors, or was it contaminated by the activation and boosting provided by the voltage-dependent Sodium channels located on the dendrites. There are a number of studies dealing with Nav density on different types of interneuron dendrites, for example on fast-spiking PV+ cells (Hu et al. 2010) or on hippocampal oriens-alveus interneurons (Martina et al. 2000). Similarly, there are many pieces of evidence showing that pyramidal cell dendrites do contain these channels in an abundance that allows for the initiation of a Na-spike (Losonczy and Magee 2006; Losonczy et al. 2008).

Based on our result and on the well-described features of dendritic Na-spikes (Larkum and Zhu 2002; Ariav et al. 2003), we wished to clarify whether the dSpikes we observed were purely NMDA-spikes or mixed spikes that contained both NMDA-receptor and Nav-channel components. We chose to again use two-photon glutamate uncaging in conjunction with pharmacology. Our protocol was the same as used above (**Fig. 25**, **Fig. 26**), with the difference that the gradual increase of activated input site numbers as a control was followed by the same gradual increase in the presence of the Sodium channel blocker 1 μ M TTX (**Fig. 41**). In contrast to the NMDAR blockage, TTX induced only minor changes in the input-output relationship of the cells. Namely, the blockage of Nav-channels caused only a negligible shift and decrease in the sigmoid input-output curve for both the Ca²⁺-responses (**Fig. 41A**) and the somatic voltage traces (**Fig. 41B**).

These results prove that 1) the interneurons display a dendritic spike that is purely NMDA-receptor by origin; and 2) that the local, active propagation of the dSpike observed in interneurons is not mediated by Nav-channels.

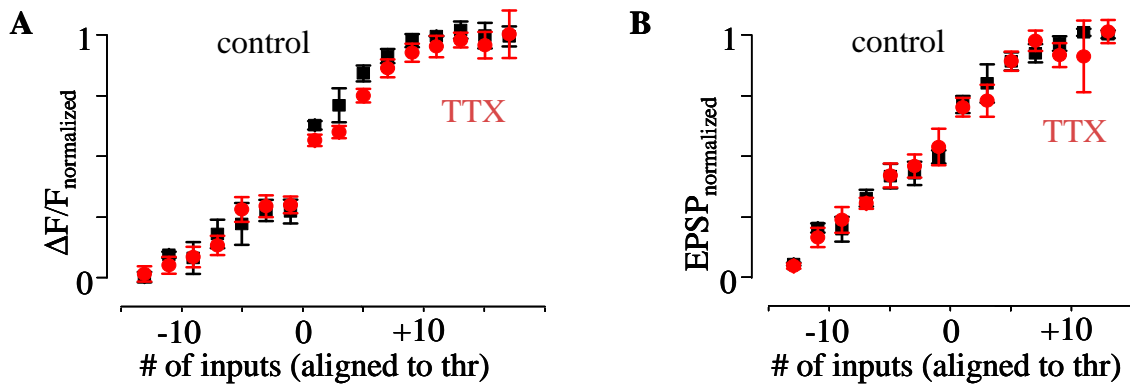


Figure 41 – Na_V -channels in signal integration of CA1 interneurons.

A) Summary plot of the threshold- (*thr*) aligned, normalized peak 3D Ca^{2+} -responses versus relative number of clustered inputs (mean \pm s.e.m., $n=5$ cells) in *control* (*black squares*) conditions and in the presence of tetrodotoxin (*TTX*, *red circles*, 1 μ M). **B)** Same as (A), but for the peak somatic voltage responses.

VII.3.4. Nicotinic Acetylcholine Receptors (nAChRs)

The experiments described above were all aimed at synaptic receptors. Our further experiments were aimed at the precisely timed activation of dendritic $\alpha 7$ -nAChRs to clarify whether these boost the induction of long-term potentiation (LTP) by excitatory postsynaptic potentials (EPSPs) and synaptically triggered dendritic Ca^{2+} transients.

We aimed to test whether we can induce LTP by pairing synaptic inputs (500 ms, 100 Hz, focal stimulation) with bAPs (500 ms, 100 pA, somatic depolarization), along with the stimulation of nAChRs by application of Ach (1 mM, for 200 ms). The muscarinic receptor antagonist atropine (1 μ M) was also present during these experiments to exclude the effects of muscarinic receptors. In these experiments we used high resistance (8–10 M Ω) patch pipettes during somatic recording in order to reduce the effect of dialysis on interneuron's plasticity, because the plasticity of interneurons seems to be sensitive to dialysis (Lamsa et al. 2005). We placed the stimulation electrode close (~ 15 μ m) to the dendrites and imaged long dendritic segments (typically > 30 μ m) using our new scanning techniques in order to find activated synaptic inputs. Both focal Schaffer collateral stimulation and somatic depolarization were set to start just prior to the peak of the ACh-induced depolarization.

The development of long-term plasticity was monitored by recording dendritic Ca^{2+} transients and somatic EPSPs following low-frequency synaptic stimulation (0.033 Hz, two stimuli at 100 Hz, 10–20 V). We placed free linescans along the dendrites to find active inputs, to measure their spatiotemporal distribution and to exclude the simultaneous activation of additional neighboring dendritic segments (Lorincz et al., 2007). The amplitudes of Ca^{2+} transients (**Fig. 42B, D**) and EPSPs (**Fig.42C, E**) increased after LTP induction.

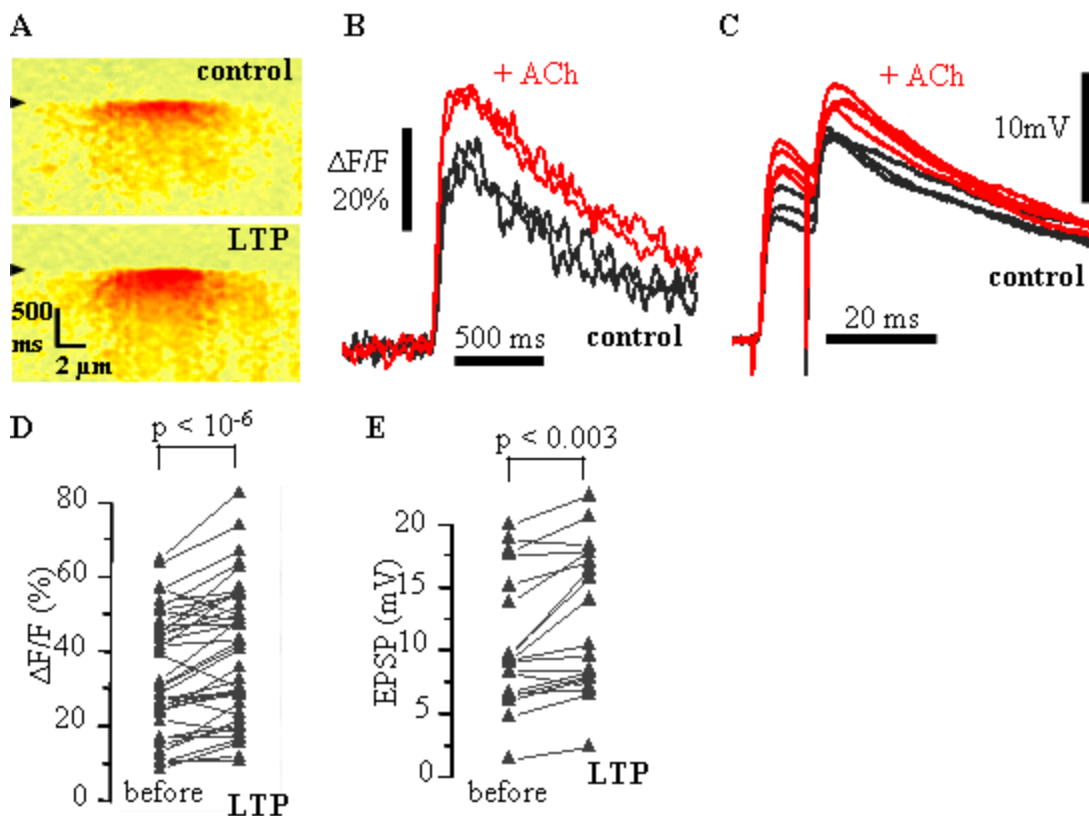


Figure 42 – Acetylcholine induces LTP

A) Normalized Ca^{2+} responses induced by focal synaptic stimulation with somatically evoked bAPs alone (control, *top*) and after added nAChR activation (LTP, *bottom*). **B-C)** Representative Ca^{2+} traces (**B**) and simultaneously measured somatic voltage traces (**C**) under control condition (*black*) and after LTP induction (*red*). **D)** Amplitudes of Ca^{2+} response for the synaptic stimulation coupled with somatically induced APs without (*before*) and with nAChR-activation (*LTP*). **E)** Same as (**D**), but for EPSP amplitudes. P values from t-tests.

We tested whether synaptic stimulation with a stronger postsynaptic depolarization, but without nAChR activation, would produce similar levels of LTP. When the same focal synaptic stimulation was paired with twice as large somatic depolarization, LTP could not be induced. Previous studies have shown that presynaptic nAChRs can bidirectionally regulate synaptic transmission (Maggi et al. 2004). Therefore, we addressed the synaptic locus of ACh-induced LTP by examining the coefficient of variation (CV) and paired-pulse ratio (PPR) of EPSP amplitudes. CV (control: 0.209 ± 0.053 ; LTP: 0.208 ± 0.033 , $P = 0.98$) and PPR (control: 1.29 ± 0.16 ; LTP: 1.11 ± 0.12 , $P = 0.08$; $n = 20$ cells) did not change significantly, suggesting that the synaptic locus of LTP in our experiments is mostly postsynaptic.

VII.4. Dendritic Spike Propagation

Our previous data showed that interneurons display actively propagating regenerative events on their dendrites, and they are NMDA-receptor dependent – most probably NMDA-spikes. Since the above mentioned experiments involving TTX proved that Na_v -channels do not play an active role in the propagation of these dendritic spikes, our further aim was to characterize the exact nature of their propagation.

Here, we used focal electrical stimulation to evoke EPSPs and dSpikes (**Fig. 43**). We have noticed in our previous experiments that the Ca^{2+} -traces of dSpikes depicted a significantly wider spatial width than those of the EPSP responses (**Fig. 25C**). To analyze this phenomenon, we plotted both EPSP- Ca^{2+} and dSpike- Ca^{2+} -transients at equal distances from the point of origin of the Ca^{2+} -responses. Then, we determined the half maximal values for both EPSP- Ca^{2+} and dSpike- Ca^{2+} -responses (**Fig. 43B, C**). When plotting the received half-maximum points over the Ca^{2+} -transients from equal distances of the starting point of the events, a sharply decreasing curve appeared for EPSPs, while the same analysis gave a curve with a plateau-like shoulder for dSpikes. Even these preliminary data showed a marked difference in propagation values of the EPSPs and the dSpikes we observed.

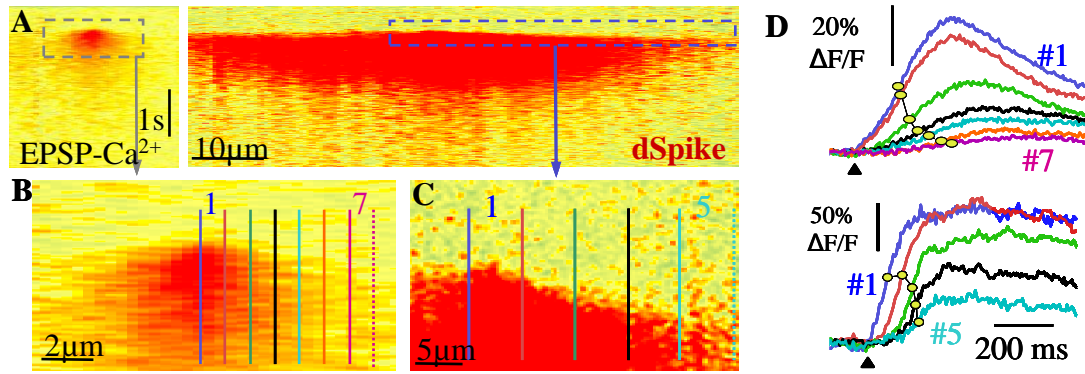


Figure 43 – Dendritic NMDA-spike propagation.

A) Synaptic stimulation induced 3D Ca^{2+} -responses. **B-C)** Magnified view of the responses in **(A)**. **D)** Ca^{2+} transients derived from the indicated color coded regions from **(B)** in *top*, and from **(C)** in the *bottom* panel. *Yellow dots* show onset latency times measured at the half-maximum of responses. *Black arrowheads*: stimulation.

To receive the propagation speed, we plotted the latency for the onset of events in the function of distance (**Fig. 44A**). EPSP- Ca^{2+} propagation was well characterized by a parabolic fit, suggesting a determining role of diffusion (Goldberg et al. 2003a; Rozsa et al. 2004), while dSpike latency showed an exponential increase on this spatial scale, resulting in an average propagation speed approximately 10 fold higher for dSpikes than for EPSPs. The high propagation speed could most likely be contributed to active events, in this case, possibly the active involvement of NMDA-receptors.

As propagation speed is well-known to be temperature-dependent, the major difference we received between EPSP and dSpike propagation could be due to the lower temperatures commonly used in *in vitro* experiments (25 °C). Therefore, we repeated our measurements at a more physiological temperature (32 °C). Although increasing the temperature markedly increased the propagation speed of EPSP- Ca^{2+} , the difference between dSpike and EPSP propagation was still significant ($p < 0.05$; **Fig. 44B**).

These results prove that the previously described events are active processes, and further underline that hippocampal CA1 interneurons display dSpikes.

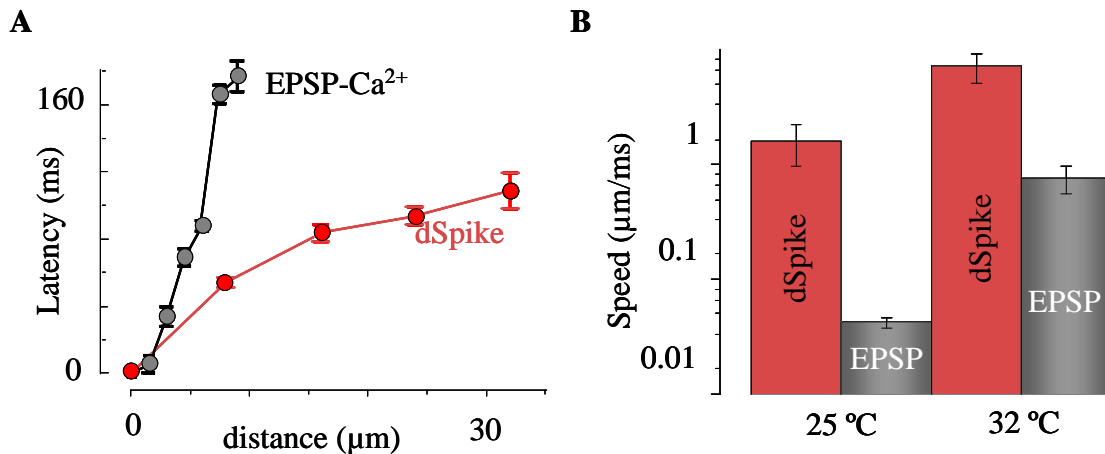


Figure 44 – NMDA-spike propagation is faster than EPSPs.

A) Onset latency times of the Ca²⁺-transients as a function of distance after subtraction of the shortest latency times revealed ~10-fold higher average propagation speed for dSpikes. **B)** dSpike-Ca²⁺ propagation speed was an order of magnitude higher both at 32 °C (n = 6) and 25 °C (n = 6) as compared to EPSP-Ca²⁺s.

VII.5. Action Potential Backpropagation in Interneuron Dendrites

In our previous results, we have dealt with events connected to synaptic mechanisms: we focally stimulated input sites and observed how the different responses act when activated singularly or in concert. Besides the synchronous or asynchronous stimulation, we also examined the spatial distribution and its effect on signal integration in interneuron dendrites. Though the synaptic machinery with its functional and structural implications is one of the most well-studied processes considering dendritic phenomena, besides the local regenerative dendritic action potentials the axon potential initiated at the soma or axon initial segment (Kole and Stuart 2012) can also affect synaptic signals (Stuart and Sakmann 1994; Helmchen et al. 1999; Larkum et al. 1999a; Golding et al. 2001; Rozsa et al. 2004; Kampa et al. 2006; Rozsa et al. 2008). The backpropagating action potential (bAP) can modulate local dendritic events such as synaptic plasticity (Markram et al. 1997; Murphy et al. 1997; Golding et al. 2002; Gullledge et al. 2005; Gordon et al. 2006; Kampa et al. 2006). Therefore, next we wished to examine whether there is any relation between the local regenerative activity

and the global neuronal action potential, and then to study another characteristic of the global action potential in CA1 interneuron dendrites.

VII.5.1. Dendritic NMDA-Spikes and bAPs in Interneurons

Previous studies have shown that there can be marked points of increased significance on the dendrites (Milojkovic et al. 2005a; Fitzpatrick et al. 2009). The structural features of these spots were obvious from anatomical studies: the dendrites can show bulges and thinner segments (Stuart et al. 2007; Katz et al. 2009). The dendritic segments that show increased responses are called *hot spots*, while those that show decrease are called *cold spots* (Frick et al. 2001; Job and Eberwine 2001; Fitzpatrick et al. 2009). Our aim was to examine whether the above described NMDA-receptor mediated dSpikes can be connected to any such regions with functionally increased significance. Functional significance can arise from the coupling of local events to global phenomena; therefore, we chose to examine the relation of local dSpikes to the bAP-induced Ca^{2+} -influx. We applied focal electrical stimulation to induce EPSPs and dSpikes, and in some cases used stimulation high enough to evoke somatic action potentials. At the same time, we recorded dendritic Ca^{2+} -responses, and were able to correlate those with the somatically recorded voltage traces (**Fig. 45**).

Following the above mentioned protocol, we could determine that without somatic action potentials, dSpikes induced localized 3D Ca^{2+} responses (falling below 40 nM within $15.7 \pm 1.9 \mu\text{m}$, $n = 9$ cells; see also **Fig. 36**). When somatic action potentials were induced, spatial analysis of the Ca^{2+} -responses have shown that the dSpike-induced synaptic responses (*suprathreshold-dSpike*) gave rise to 3D Ca^{2+} responses invading the entire imaged segment of the dendrites (distant segment showed 250 ± 62 nM; **Fig. 45B**).

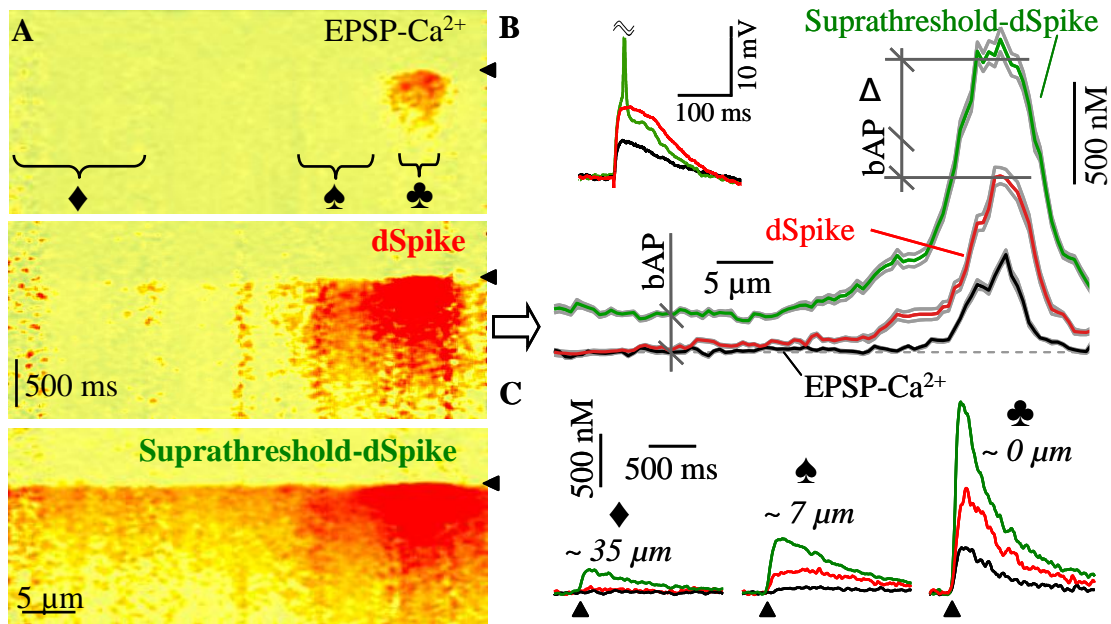


Figure 45 – Initiation Phase of Somatically Suprathreshold dSpikes.

A) 3D Ca²⁺ responses induced by focal synaptic stimulation show subthreshold dSpikes (*dSpike*) alternating with suprathreshold responses (*Suprathreshold dSpike*) at near-threshold stimulus intensities. A subthreshold EPSP-Ca²⁺ is shown for comparison (*EPSP-Ca²⁺*). B) Spatial distribution of peak [Ca²⁺]_i calculated from (A). Here we estimated Ca²⁺ levels from the 3D Ca²⁺ responses to minimize dye saturation effects. *Gray traces* show mean ± s.e.m. *Inset*, Corresponding somatic membrane voltage. C) Peak [Ca²⁺]_i in time at selected regions indicated in (A). *Black arrowhead* indicates time of stimulation.

Our further aim was to analyze the measure of the Ca²⁺-influx at the origin of the dSpike to see whether the increase follows a linear characteristic when dSpikes are accompanied by a somatic spike. The spatial analyses have already revealed that dSpike-Ca²⁺ alone exceeds bAP-Ca²⁺ (bAP-Ca²⁺: 252 ± 30 nM, dSpike: 620 ± 134 nM, N = 6 cells). Moreover, bAPs in themselves show lower Ca²⁺-responses than those of dSpikes followed by somatic spikes (**Fig. 45B**). When we looked at dSpikes that were occasionally followed by bAPs, the temporal analyses showed that the suprathreshold-dSpikes gave significantly higher Ca²⁺-transients than the arithmetic sum of the dSpike-Ca²⁺ and the bAP-Ca²⁺ (suprathreshold-dSpike: 1385 ± 215 nM, p < 0.006; n = 6 cells; **Fig. 46C**). Our data show that dSpikes and bAPs can summate supralinearly, serving as

yet another means of dendritic logical processing by way of difference in dendritic signal integration.

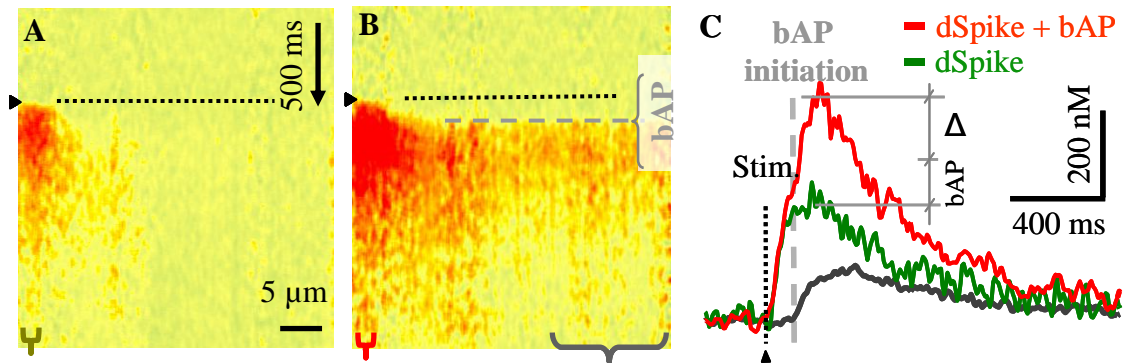


Figure 46 – Initiation Phase of Somatically Suprathreshold dSpikes.

A) dSpikes-induced 3D Ca^{2+} response after focal synaptic stimulation. **B)** Occasionally, these dSpikes were transformed after some delay into a more generalized suprathreshold response (*gray dashed line*). **C)** Color-coded Ca^{2+} transients derived from the marked regions of 3D Ca^{2+} responses in **(A)** and **(B)**. A large supralinear $[\text{Ca}^{2+}]_i$ increase occurred (*empty triangle*) when the generalized response started (*gray dashed line*). *Black dotted lines and black arrowheads*: time of stimulation.

These results indicate that similarly to the somatically subthreshold dSpikes, synaptic inputs-driven postsynaptic firing is also associated with locally increased Ca^{2+} gain at the location of inputs in CA1 interneuron dendrites. As a result, when dSpikes are coupled with bAPs, the local Ca^{2+} signal is amplified, and might serve as a basis for synaptic plasticity processes such as long term potentiation or depression.

VII.5.2. Nicotinic Effects on bAPs

In order to study coincidence between $\alpha 7$ -nAChR activation and bAPs, we performed current injections into the soma of interneurons to induce APs during rapid ACh injection with different time delays (**Fig. 47A, B**). The amplitudes of the five bAP-evoked Ca^{2+} -transients were dependent on the relative timing between AP arrival and the onset of ACh application. When bAPs arrived at the onset of ACh application (0.1–0.3 s; **Fig. 47A**, red trace), the amplitude of the bAP-evoked Ca^{2+} transients was

facilitated (by $25.0 \pm 1.5\%$, $P < 0.0001$; $n = 211/11$ measurements/cells; **Fig. 47A–D**, red points and traces). Eliciting bAPs later (1–3 s; **Fig. 47A**, blue trace) resulted in depressed Ca^{2+} transient amplitudes ($84.3 \pm 1.6\%$ of the control, $P < 0.0001$; $n = 131/11$ measurements / cells; **Fig. 47A–D**, blue points and traces). The distribution of relative amplitudes could be well separated (**Fig. 47C**).

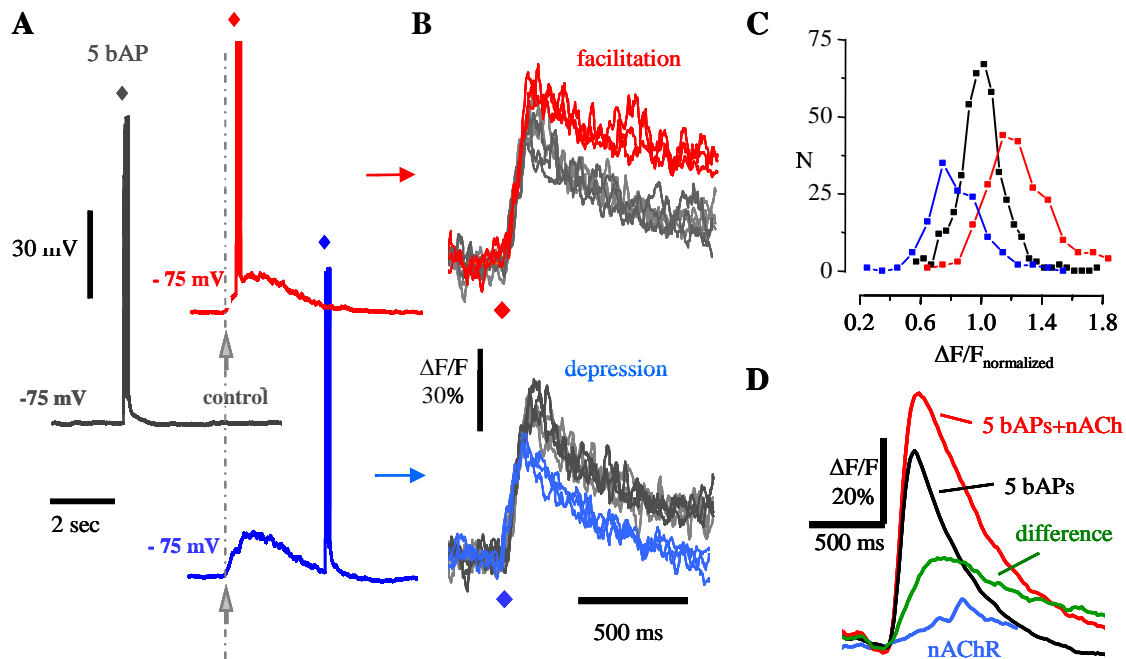


Figure 47 – Timing-dependent summation of $\alpha 7$ -nAChR- and bAP-induced dendritic Ca^{2+} transients.

A) Current clamp recordings showing coincidence of the $\alpha 7$ -nAChR- (gray arrows) and 5bAP- (diamonds) elicited membrane potential transients at different latencies. **B)** bAP-induced individual Ca^{2+} traces increase (“facilitation”) when bAPs are elicited at the onset (A, red trace) of $\alpha 7$ -nAChR activation and decrease (“depression”) when they arrive at the tail (A, blue trace). Control traces: gray. **C)** The distribution of normalized amplitudes of facilitation (0.1 - 0.3 s) was shifted to higher values (red) compared to control (black) responses, and an opposite shift was observable in the case of depression (1 – 3 s; blue; pooled data, $N = 11$ cells). **D)** Averaged dendritic Ca^{2+} transients in the case of facilitation. The green trace indicating the difference between the bAP-induced Ca^{2+} transients measured with (red) and without (black) rapid ACh injection exceeded the Ca^{2+} transients evoked by rapid ACh injection alone (blue), indicating supralinear summation.

These findings suggest that the interaction between $\alpha 7$ -nAChRs and bAPs depends on the timing of the two events. In order to study the properties of summation during facilitation, we subtracted the mean of the control curves (**Fig. 46D**, in *black*, mean of $n = 3$ – 5 curves per cell) from the mean of the facilitated transients (**Fig. 46D**, *red*) and plotted the peak of the difference against the peak amplitude of the $\alpha 7$ -nAChR-induced Ca^{2+} transient for each cell (**Fig. 46D**). The mean magnitude of the sublinearity of depression was $6.6 \pm 1.1\%$ ($\Delta F/F$, $P < 0.0001$). The magnitude of the supralinearity of facilitation (**Fig. 46D**) was $24.1 \pm 4.9\%$ ($\Delta F/F$, $P < 0.00001$). The magnitude of non-linearity is relatively large when compared with the amplitude of the bAP-induced transients (facilitation: $45.0 \pm 5.2\%$; depression: $14.4 \pm 2.2\%$; the amplitude of the bAP-induced transients was $48.3 \pm 4.4\%$, $\Delta F/F$). Similar results were obtained with choline. We could also reproduce these results using a low-affinity indicator (OGB-5N), excluding the possibility of perturbation of Ca^{2+} signaling by high-affinity OGB-1.

VIII. DISCUSSION

VIII.1. Novel Imaging Methods Applied in Search of Dendritic Phenomena

The results presented above rely on the newly developed two-photon imaging methods, but how does the two 3D imaging strategy of Roller Coaster Scanning and random access acousto-optical scanning (Rozsa et al. 2007; Vucinic and Sejnowski 2007; Duemani Reddy et al. 2008) perform, compared to each other?

A general problem with the AOD-based 3D scanning is that when good spatial resolution needs to be maintained, the measurement is limited to a small number of points (~ 40 points/ms). In this case, in fact, deflectors with large apertures are needed to maintain large number of grating lines in the aperture during operation. Switching time on the other hand is determined by the time the (new) acoustic waves propagate through the entire crystal, which can be as long as ~ 25 μ s. If a dendritic segment has to be scanned “continuously” (i.e., at high spatial sampling rate of one point every 0.1 μ m), with the above switching times, the dendritic segment scannable per ms is limited to a few μ m only (in our case ~ 4 μ m/ms). An additional shortcoming of the long switching times typical of random-access scanning is the reduction of SNR, because a large percentage of the total measurement time is wasted during switching. Indeed, typical switching times (10-35 μ s) are considerably longer than the minimum pixel dwell time used in two-photon microscopes with moving mirrors (~ 1 -4 μ s).

In contrast, Roller Coaster Scanning provides a continuous measurement at high resolution along long neuronal processes and does not go on the expenses of pixel dwell time. In practice, currently available galvanometric scanners limit this value to a few hundred μ m/ms, but this still provides about two orders of magnitude higher resolution for the measurement of contiguous structures than acousto-optical scanners, because switching time is equal to zero and pixel dwell time is technically not limited (although typically above 0.1 μ s). This yielded the high spatial sampling power required to show how the NMDA-spikes propagate (**Fig. 43-44**).

Up to recently, AOD-based techniques also place a limitation on either the spatial resolution or on the field of view (AOD: $\sim 200 \times 200$ points resolution and ~ 200 μ m x

200 μm field of view as opposed to Roller Coaster scanning: 2200 x 2200 points resolution and 650 μm x 650 μm field of view). With our improvements to AOD-scanning, these limitations have been lifted, yielding a similar field of view to Roller Coaster scanning of 760 x 760 μm^2 (Katona et al. 2012).

Finally, the optical pathway of the Roller Coaster microscope is simple and does not contain any material beyond the objective that introduces angular, linear dispersion or laser intensity loss, therefore: i) experiments requiring high energy pulses like two-photon uncaging, bleaching, ablation or *in vivo* imaging of deep tissue (Helmchen and Denk 2005) are achievable, ii) the excellent spatial resolution characteristics of two-photon microscopy are preserved, and iii) the combination of Roller Coaster Scanning with new optical methods such as high resolution imaging techniques is possible (Willig et al. 2006; Ding et al. 2009).

To sum up, Roller Coaster Scanning was essential in achieving the presented results. Firstly, the high spatial sampling gave us the means to clearly define the borders of different dendritic events at the first place. The separation of Calcium signals ranging from unitary EPSPs to dSpikes was only possible because of the long dendritic segments imaged with high spatial resolution. This has led us to search for separate populations of events using cluster analysis, where the preliminary results were supported by the analysis. Secondly, these segments could have only been imaged by scanning in three dimensions, with the retained characteristics of two-photon imaging, since the following the tortuous dendrites could only have been done by the brute force approach, using many times more patched cells to find the dendrites lying long enough in one plane. Thirdly, the increase in the z-range allowed us to scan and identify the spontaneous responses, which gave us the final confirmation that the events we could evoke were clearly observable without any major stimulus or perturbation to the naïve network.

VIII.2. Cable Theory and Compensatory Mechanisms for Signal Loss

Dendritic signal processing has long been studied to understand how neurons transform their inputs to output (Rall 1969a; Rall 1969b; Kandel et al. 1977; London and Häusser 2005). The simple passive propagation of inputs on dendritic „cables” is still valid for the explanation of many of the electrophysiological properties of synaptic

signal processing. This leads to many consequences. For example, it is well-known that the main integrator zone for the output of an average principal cell lies at the axon initial segment (Kole and Stuart 2012). On the other hand, there are numerous axons giving synapses on very distant areas of the dendritic arbor (Gulyas et al. 1999; Takacs et al. 2011). The properties described by Cable Theory would suggest that signals arriving onto these distant synapses are wasted because of the attenuating effect of the passive propagation of signals (Stuart and Spruston 1998). Though Ockham's razor states that the simplest solutions are the true ones, here one has to assume that the simplest of all explanations for propagation might not give proper explanation for such a huge waste of energy and effort in the neuronal network. To overcome the signal loss arising from passive dendritic properties, there are compensatory mechanisms that help distant synapses to subdue the passive attenuation. One of these is the changing morphology of the synapses: the farther a synapse is from the soma, the larger it is (Magee and Cook 2000; London and Segev 2001; Smith et al. 2003). On the other hand, this 'synaptic scaling' can also be observed on the ion channel level, where the more distant synapses show higher AMPA receptor densities (Smith et al. 2003).

Our results on the lack of distance-dependence of for supralinear dendritic integration suggest that interneurons might be devoid of such synaptic scaling. On the other hand, our measurements have been conducted in the near vicinity of the somata, ~75 μm away from the soma on average. Further studies would be needed to justify the lack of synaptic scaling by observing synchronous events at or near the terminal ends or tips of dendrites. Furthermore, the channel densities of VGCCs, NMDARs, AMPARs or HCNs will have to be defined on CA1 str. rad. interneurons, similarly to NaV in hippocampal oriens-alveus PV+ interneurons (Martina et al. 2000).

On the other hand, these compensatory mechanisms do have their limitations, since very distant synapses would have to be enormous in size with an extremely high number of synapses, which again is unfeasible and its cost per benefit ratio is definitely tipped towards the highly expensive side. Another way to compensate for the signal loss is to surpass Cable Theory and include either points of high responsiveness also called 'hot spots' (Frick et al. 2001; Fitzpatrick et al. 2009), or to have an amplification mechanism that overrides passive propagation (Stuart and Sakmann 1994; Hausser et al. 2000; Oakley et al. 2001b; Vetter et al. 2001; Sjostrom et al. 2008). This amplification

mechanism could help the distant synaptic signals reach the soma or help the action potentials to affect the synapses (Stuart et al. 1997), the latter mechanism being crucial in synaptic plasticity (Markram et al. 1997; Sjöström et al. 2008).

VIII.3. Compartmentalization in Dendritic Processes

The notion of 'hot spots' or selected, distinct areas brings forth one of the most important aspects of signal amplification: compartmentalization. The initiation and saltatory propagation of the action potential provides us a wonderful example of how efficient compartmentalization can be: without the axon initial segment and the nodes of Ranvier and their high ion channel density it would be much harder to evoke and then to maintain APs on a long distance (Purves 2008; Kole and Stuart 2012). The same is true for signal amplification on pyramidal neurons, but here the compartment is the morphologically and electrotonically isolated dendritic spine (Yuste and Denk 1995), where the neck of the spine is considered to be a high electronic resistance gate that keeps the synaptic signals and Calcium influx localized (Svoboda et al. 1996; Sabatini and Svoboda 2000; Yuste et al. 2000; Sabatini et al. 2001; Araya et al. 2006). There is no such morphological compartmentalization in aspiny interneurons, but still, functional compartments are present (Goldberg et al. 2003a; Goldberg et al. 2003b; Rozsa et al. 2004).

The results I presented in this work also show that functional compartments exist in hippocampal interneuron dendrites, thus supplying the basics for amplification. The double stimulation of two of these dendritic compartments on interneurons resulted in supralinear signals. These results would lead us to the direction that these functional compartments do their tasks similarly to pyramidal cell spines, because in our studies both compartments were situated on single dendritic branches. There is ample evidence that single branches function as computational subunits on pyramidal cells (Losonczy and Magee 2006; Nevian et al. 2007; Losonczy et al. 2008; Makara et al. 2009).

Furthermore, when I examined the time window for the supralinear activation of separate compartments, I saw a brief, 10 ms range for supralinearity. This brief time window suggests that CA1 str. rad. interneurons are coincidence detectors, but the range for summing inputs is more blurred than that of the hippocampal str. oriens-alveus PV+ interneurons (Hu et al. 2010), but is similar to pyramidal cells (Stuart and Häusser

2001). The range for coincidence detection puts the CA1 str. rad. interneurons in a position to accept and amplify signals that are more sparsely arriving, thus creating a broader range for the physiological control of their targets. Since the CA1 str. rad. interneurons are either interneuron-targeting or dendrite-targeting cells (Somogyi and Klausberger 2005; Klausberger and Somogyi 2008), any amplification in their inputs can lead to a significant modulation of the network responses under physiological conditions such as hippocampal sharp wave oscillations (Kamondi et al. 1998).

VIII.4. Dendritic Signal Amplification

But how is the amplification produced? In our quest for the answer, we followed single functional compartments of interneuron dendrites. Firstly, we showed that the spatial distribution of inputs is important on hippocampal interneurons, in fact. When activating the same number of inputs in a clustered or a distributed manner on a single dendritic branch, we received surprising results: clustered inputs gave supralinear input-output curves, while distributed inputs show linear summation. This was surprising in the light of previous results on pyramidal cells, where oblique dendrites were shown to produce similar responses for clustered or distributed inputs (Losonczy and Magee 2006). What's more, whole branches could be characterized as 'weak' or 'strong', and there have been no computational subunits below the branch level (Losonczy et al. 2008). Furthermore, previous studies dealt with interneurons as global, single-layer integrator units consisting of linearly, slightly sublinearly integrating dendrites, faithful postsynaptic information relay was assumed (Tamas et al. 2002; Jia et al. 2010; Varga et al. 2011).

Next, we set out to characterize the supralinearity in single functional compartments. According to previous results, we suspected the appearance of dendritic regenerative events – dendritic spikes – on interneuron dendrites (Llinas et al. 1968; Larkum et al. 1999a; Schiller et al. 2000)

VIII.5. Dendritic Spikes

Dendritic spikes are intensively studied events, since they may enhance the computational complexity of neurons (Schiller et al. 2000; Poirazi et al. 2003b; Polsky et al. 2004; Losonczy and Magee 2006; Losonczy et al. 2008; Larkum et al. 2009). Although thoroughly investigated in principal cells, the occurrence of these events in

interneurons has not been shown, despite the major role interneurons play in oscillations and pattern generation (Klausberger and Somogyi 2008).

Our work shows that clustered input patterns can produce strongly supralinear dendritic integration in radiatum interneurons even though they have more simple, aspiny dendrites. This could lead to the enhancement of clustered distal inputs by taking advantage of local dendritic NMDA spikes, and therefore distal inputs might overcome dendritic signal attenuation and reach the axo-somatic integration region (Nevian et al. 2007).

Several pieces of evidence indicate that the local events in our experiments are dendritic spikes. Firstly, the magnitude of the 3D Ca^{2+} responses induced by clustered synaptic pattern of two-photon glutamate uncaging followed a sigmoid shape as a function of input number, with a step-like increase at a given input number (threshold). Here, the simultaneously recorded somatic membrane parameters such as amplitude, width and $\delta V/\delta t$ of gluEPSPs also showed a step-like jump. Secondly, the threshold value of the input-output curve measured in both Ca^{2+} response and corresponding membrane potential was the same. Thirdly, spatially distributed, less interacting inputs were unable to produce a sigmoid input-output relationship. Similarly, near-threshold focal electric stimulation also produced alternating, all-or-none responses resembling the supra- and just subthreshold uncaging-evoked transients. Spatial distributions of dSpikes Ca^{2+} -transients induced either by focal stimulation or uncaging were shown to be wider when compared to subthreshold responses, and neighboring dendritic areas in proximity to the input sites showed all-or-none Ca^{2+} responses at threshold. Furthermore, local spike generation was reflected in a ~10-fold increase in lateral propagation speed.

Our results indicate that these dSpikes are NMDA spikes as local spike-related Ca^{2+} responses induced by focal synaptic stimulation or uncaging were reduced close to background fluorescence levels in the presence of the NMDAR antagonist AP5, and simultaneously recorded voltage responses lost their characteristic NMDA “shoulder” component (Maccaferri and Dingledine 2002). In addition, blockade of NMDARs converted both Ca^{2+} and somatic voltage response input-output curves from sigmoid to linear, with a much smaller gain. dSpikes are likely to be initiated by a baseline NMDAR activity readily detectable during subthreshold synaptic activation. In contrast

to pyramidal cells, the contribution of Na^+ channels and VGCCs to dSpikes was negligible (Schiller et al. 2000; Larkum et al. 2009).

VIII.6. Spontaneously Occurring NMDA-Spikes

Physiological network activity in a dual superfusion-chamber produced spontaneous dSpikes which could be reproduced by clustered suprathreshold glutamate uncaging. These data suggest that NMDA spikes could be one of the major players *in vivo* during coincidence detection in neurons. In pyramidal cells, distributed inputs had the same (or even larger) efficiency in local spike generation when compared to clustered inputs (Losonczy and Magee 2006) in good agreement with both two- (Poirazi et al. 2003b; Katz et al. 2009) and three-layer models (Larkum et al. 2009) of synaptic integration considering individual branches as single integration compartments (**Fig. 48**) (Polsky et al. 2004; Losonczy et al. 2008; Larkum et al. 2009).

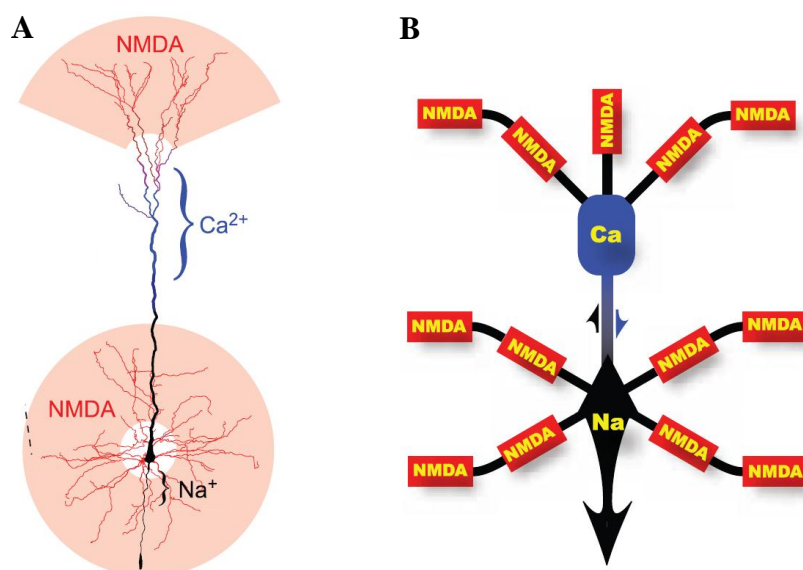


Figure 48 – Dendritic spike initiation zones of pyramidal cells

A) Reconstructed pyramidal neuron showing the regions of the dendritic tree where NMDA (red), Ca^{2+} (blue), and Na^+ (black) electrogenesis can be initiated. **B)** Schematic representation of the important subcompartments of a typical L5 pyramidal neuron showing the relationship of multiple local sites for NMDA spikes to the Ca^{2+} and Na^+ initiation zones, which can signal each other through active propagation along the main apical trunk (arrows). *Source: (Larkum et al. 2009)*

In contrast, spontaneous and evoked dSpikes in interneurons were localized to small dendritic segments within individual dendritic branches (spatial half width of dSpike was $\sim 14 \mu\text{m}$, average dendritic branch length for comparison: $78 \pm 15 \mu\text{m}$, range 30-176 μm). The number of convergent inputs arriving to a particular dendritic segment capable of initiating dSpikes was estimated to be ~ 9 ($\sim \text{Peak}_{\text{dSpikes}}/\text{Peak}_{\text{uEPSPs}}$). The inflection point of the sigmoid input-output curves suggested a similar threshold value, 9.8 inputs, a number smaller to that reported for pyramidal neurons (Losonczy and Magee 2006). Furthermore, when we set a compartmental model using one of our reconstructed interneurons as a morphological basis, the temporally and spatially clustered activation of ~ 10 NMDA synapses was able to reproduce dSpikes. This represents approximately 10 % of all excitatory terminals arriving onto a single segment of an interneuron's dendrite (Gulyas et al. 1999; Takacs et al. 2011). The one-to-one relationship between dendritic subunits and thin dendritic branches described in pyramidal cells is therefore further refined in interneurons by active and dynamic dendritic segment subregions. The finer arithmetic structure of interneuron dendritic shafts may increase their computational power, and may partially compensate for their shorter and smaller dendritic arborization and less number of spines. Our laboratory along with others has previously found a similar strategy for enhanced dendritic signal compartmentalization in interneurons by an increased Ca^{2+} buffering and extrusion capacity (Goldberg et al. 2003a; Rozsa et al. 2004). Interestingly, recent *in vivo* data showed a similar fine structure of dendritic organization of sensory inputs in anesthetized mice (Jia et al. 2010; Varga et al. 2011), although based on the observed small response amplitudes authors argue against dendritic spikes.

Our observations of local dSpikes in thin dendrites of interneurons were facilitated by more factors. We have used a new recording chamber with dual superfusion to maintain physiologically relevant network activities through better oxygen supply (Hajos et al. 2009; Chiovini et al. 2010). We developed Roller Coaster Scanning applicable both *in vitro* and *in vivo*, increasing access rate to imaging long continuous dendritic segments. This second feature, with the preserved high spatial and temporal resolution, allowed us to precisely localize the sites and properties of

spontaneous (and evoked) individual inputs, as well as their spatially and temporally patterned combinations during integration.

Our data suggest a new principle as to how interneurons integrate synaptic information. The interactions of spatially clustered and synchronized excitatory inputs are enhanced by the involvement of NMDA receptors in generating the regenerative dendritic spikes (Lei and McBain 2002; Maccaferri and Dingledine 2002; Larkum and Nevian 2008) and might provide a framework for interactions leading to synaptic plasticity in interneuron dendrites (Lamsa et al. 2005; Lamsa et al. 2007; Sjostrom et al. 2008).

VIII.7. nAChRs and Dendritic Function in Hippocampal Interneurons

During the last decade, a number of studies have revealed the functional importance of bAPs in neurons of the central nervous system (Stuart et al. 1999; Waters et al. 2005). Specifically, the increase in volume-averaged dendritic Ca^{2+} concentration induced by bAPs underlines their role in different types of synaptic plasticity. For instance, a coincidence of bAPs with synaptic activity initiated long-term changes (LTP) in the efficiency of excitatory and inhibitory synaptic transmission (Magee and Johnston 1997; Markram et al. 1997; Holmgren and Zilberter 2001). This mechanism (and LTD) has recently been found to also occur in interneurons (Lei and McBain 2002; Lei and McBain 2004; Lamsa et al. 2005; Pelkey et al. 2006), validating the importance of postsynaptic depolarization- and bAP-induced calcium signaling. Although the interaction of bAPs with synaptic stimulation is well characterized, much less is known about its relationship with nonsynaptic transmission (for interneurons, see Martina et al. 2000; Rozsa et al. 2004). Our results demonstrate for the first time a timing-dependent interaction between bAPs and the activation of nonsynaptic $\alpha 7$ -nAChRs that affects Ca^{2+} transients.

The amplitude of the bAP-evoked Ca^{2+} transients was dependent on the timing between AP arrival and the onset of activation of $\alpha 7$ -nAChRs. When bAPs arrived during the rising phase of ACh induced depolarization (0.1 - 0.3 s; Fig. 6), the amplitudes of the bAP-evoked Ca^{2+} transients were boosted. Eliciting bAPs later (1 - 3 s) resulted in depressed amplitudes. Depth-dependent dampening of the spatiotemporal

profile of ACh and the added calcium buffer capacity possibly elongated the time window of the modulation.

The effects of the calcium permeable $\alpha 7$ -nAChRs on bAPs and synaptic transmission suggest that $\alpha 7$ -nAChRs might be involved in the regulation of dendritic integration and dendritic spikes.

VIII.8. $\alpha 7$ -nAChRs and Plasticity

Our results show that dendritic $\alpha 7$ -nAChR activation in interneurons boosted the induction of LTP of the Schaffer collateral pathway. A stimulation paradigm that normally failed to produce LTP (it rather induced depression) was able to boost LTP production when a sufficiently large $\alpha 7$ -nAChR-induced depolarization was elicited and timed to coincide with the electrical stimulation. The added depolarization caused by $\alpha 7$ -nAChR activity would help to relieve the Mg^{2+} block of NMDARs, setting into motion the calcium-dependent cascade and the electrical events leading to LTP (Malenka and Nicoll 1999; Martin et al. 2000). Nevertheless, an increased postsynaptic depolarization does not explain all the effects of $\alpha 7$ -nAChR activity, because when we simply doubled the postsynaptic depolarization that was paired to the electrical stimulation of Schaffer collaterals, LTP could not be consistently produced.

An alternative possibility is that the activation of presynaptic $\alpha 7$ -nAChRs resulted in the increased probability of LTP (Mansvelder and McGehee 2000; McGehee 2002). However, under our experimental conditions, this form of modulation is most likely not involved in the nicotinic enhancement of LTP, because neither CV nor PPR were changed following LTP induction.

The temporal fidelity of input integration and firing in pyramidal neurons is determined by the balance of excitation and inhibition. The selective nicotinic boost of LTP formation may increase the inhibition provided by feedforward interneurons, narrowing the temporal window of integration. Therefore, the dendritic $\alpha 7$ -nAChRs of interneurons may regulate temporal fidelity in the hippocampus.

GABAergic interneurons innervating pyramidal cells are ideally suited to control the pattern and timing of their target cell (Penttonen et al. 1998; Freund 2003). Although a direct effect of nAChRs on pyramidal cell LTP has been suggested in one study (Ji et al. 2001), a more possible explanation is an indirect effect which is mediated

by GABAergic inhibition (Couey et al. 2007). The action of inhibitory cells can synchronize action potential discharges at theta and/or gamma frequencies, and/or during hippocampal sharp waves. These synchronous events are thought to be crucial in different sleep states, in various cognitive functions, and in the encoding and retrieval of information (Freund 2003; Buzsaki 2005; Somogyi and Klausberger 2005). Thus, the modulation of bAP and synaptic transmission by dendritic $\alpha 7$ -nAChRs of interneurons and the LTP boosted by these receptors may play a determining role in hippocampal functions.

IX. CONCLUSIONS

Dendritic spikes are intensively studied events, since they may enhance the computational complexity of neurons. Although thoroughly investigated in principal cells, the occurrence of these events has not been shown in interneurons before our work. In my thesis I clarify some points regarding the computational properties of interneuron dendrites.

Firstly, I could confirm that aspiny dendrites can show functional instead of morphological compartmentalization. Furthermore, these compartments seemed to be dynamic clusters of inputs, and where sliding interaction zones served as a computational subunit that were not limited to the single dendritic segments.

Secondly, my results show that the compartments can interact with each other, boosting the neighboring compartments' responses in a nonlinear fashion. In addition, the interaction between compartments can happen within a 10 ms time window, leaving ample time for coincidence detection.

Next, we have investigated the nature of these compartments by using newly developed 3D imaging techniques. The novel tools proved to be indispensable for following the tortuous dendritic processes and for mapping long dendrites during the localization of spontaneous events. The localized compartments showed a similar input-output curve as to the ones observed for pyramidal neurons, where clusters of synchronously active inputs produced the amplification of synaptic responses, leading to dendritic spikes. The different stimulation techniques assured that these results stand on firm experimental grounds, while the imaging combined with electrophysiology proved that supralinearity exists for both local Calcium and more global, somatically recorded signals.

To clarify the exact mechanisms responsible for the appearance and nature of dendritic spikes, we turned to pharmacology. Here, the blockage of VGCCs or Na_V -channels had no significant impact on the appearance of dendritic spikes. On the other hand, the NMDA-receptor blocker AP5 clearly switched the sigmoid input-output curve for both local Calcium and somatically recorded EPSPs to linear. This, supported by the low- Mg^{2+} experiments, provided clear evidence that the observed phenomena on interneuron dendrites are dendritic NMDA-spikes.

We have also shown that NMDA-spike trigger zones can serve as hot spots on interneuron dendrites, since these locations showed supralinear increase when synaptic stimulation was combined with backpropagating action potentials.

Our final study provided evidence that nonsynaptic $\alpha 7$ -nAChRs can also modify bAPs and LTP induction on interneuron dendrites.

In conclusion, our results provide insight on the dendritic computation of aspiny hippocampal interneurons. The gathered evidence suggests that interneurons show similar supralinear signal integration to pyramidal cell dendrites, and that the complexity of dendritic computations is a more general phenomenon in the nervous system. These dendritic regenerative events increase the computational power of neurons. Moreover, since our data showed that there are computational subunits below the dendritic branch level, this suggests that interneurons might be able to solve more elaborate computational tasks than we ever thought before.

Finally, the fact that dendritic spikes appeared spontaneously points to the direction that these regenerative events might play a more important role in network computations than previously imagined. Whether dendritic spikes in interneurons contribute significantly to network functions such as hippocampal oscillation remains to be identified, but recent data suggest that similar events are constantly shaping synaptic strength and re-tuning neurons *in vivo*, in the intact neuronal network of the brain.

X. ÖSSZEFOGLALÁS

Az idegsejtek különféle módon képesek a beérkező jelek információtartamának feldolgozására, hogy végül kimenő jelükkel, akciós potenciállal válaszoljanak. Piramissejteken igazolták, hogy dendritjeiken nem pusztán matematikai jelösszegzést végeznek, hanem megfelelő szinkronicitás esetén képesek a jelek felerősítésére is. Így egy kis amplitúdójú jelsorozat értéke is megnőhet az agy információs hálózatában.

Munkám során a hippocampalis interneuronok dendritjeit vizsgáltam, laboratóriumunkban kifejlesztett két-foton mikroszkópai módszerek és egysejt elvezetés segítségével. A szinaptikus jelek esetünkben lehettek a) spontán eredetűek (új típusú szeletfenntartó kamra révén) (Chiovini et al. 2010); b) elektromosan kiváltott jelek (fokális elektromos stimuláció révén), vagy c) két-foton fotokémiaileg aktivált glutamát felszabadítás segítségével kiváltott posztzinaptikus jelek (Katona et al. 2011).

Eredményeimben kimutattam, hogy a jelösszegződés a funkcionális alegységeket tartalmazó interneuron dendriteken szupralineáris lehet anatómiai kompartmentalizáció nélkül is, 10 ms időablakon belül. Kilenc szomszédos szinapszis szinkron aktiválása esetén a lokális Ca^{2+} beáramlás és a sejttesten elvezetett elektromos jel is nagyobb amplitúdójú volt, mint a kilenc egyedi jel matematikai összege. Farmakológiai kísérletekkel kizártuk a feszültségfüggő Na^+ és Ca^{2+} csatornák szerepét, és igazoltuk, hogy NMDAR-közvetítette dendritikus akciós potenciál jelentkezik az interneuronokon is. Emellett a dendritikus nACh-receptorok aktivációja modulálta a visszaterjedő akciós potenciál (vAP) dendritikus Ca^{2+} beáramlását, és LTP-t váltott ki vAP és szinaptikus stimuláció szinkron alkalmazásakor (Rozsa et al. 2008).

Eredményeink alapján a piramissejteknél tapasztalható szupralineáris jelösszegződés az általunk megfigyelt interneuronokra is jellemző, és ezek funkcionális alegységei a szupralinearitás által növelhetik a sejt információfeldolgozó képességét.

XI. SUMMARY

Neurons can process the information in afferent inputs in different ways, which all might lead to their output, the action potential firing. Recent data showed that pyramidal cells do not merely add the signals of synchronous inputs in a mathematical fashion on their dendrites, but the signals are locally amplified, which will lead to the increase in the significance of information content of relatively small amplitude signals. Pyramidal cells take advantage of the dendritic spines for these phenomena.

My work involved the study of hippocampal interneurons with aspiny dendrites, by using newly developed two-photon imaging methods and patch-clamping. Here, the synaptic signals were of a) spontaneous origin by utilizing a slice holding chamber that allowed higher overall activity (Chiovini et al. 2010); b) induced by focal electrical stimulation, or c) evoked by two-photon glutamate photoactivation (Katona et al. 2011).

The results show that signal integration can also be supralinear for the co-activation of functional compartments in a 10 ms time window. In addition, if 9 clustered inputs were synchronously activated, the local Calcium influx and the somatically recorded electric signals showed higher values than the arithmetic sum of 9 individual responses. Pharmacological experiments ruled out the role of voltage-dependent Sodium and Calcium channels, and proved that dendritic NMDA-spikes appear on interneuron dendrites. Furthermore, dendritic nACh receptor activation modulates backpropagating action potential (bAP) induced calcium responses and induces LTP on Schaffer collateral inputs on interneuron dendrites during simultaneously occurring bAP and synaptic stimulation (Rozsa et al. 2008).

In conclusion, our results show that dendritic signal integration can increase the computational power of interneurons in the same manner as for pyramidal cells.

XII. BIBLIOGRAPHY

Abrahamsson, T., L. Cathala, K. Matsui, R. Shigemoto and D. A. DiGregorio (2012). Thin dendrites of cerebellar interneurons confer sublinear synaptic integration and a gradient of short-term plasticity. *Neuron* **73**(6): 1159-1172.

Andersen, P. The hippocampus book. Oxford University Press, Oxford ; New York, 2007.

Andrasfalvy, B. K., M. A. Smith, T. Borchardt, R. Sprengel and J. C. Magee (2003). Impaired regulation of synaptic strength in hippocampal neurons from GluR1-deficient mice. *J Physiol* **552**(Pt 1): 35-45.

Antic, S. D., W. L. Zhou, A. R. Moore, S. M. Short and K. D. Ikonomu (2010). The decade of the dendritic NMDA spike. *J Neurosci Res* **88**(14): 2991-3001.

Araya, R., J. Jiang, K. B. Eisenthal and R. Yuste (2006). The spine neck filters membrane potentials. *Proc Natl Acad Sci U S A* **103**(47): 17961-17966.

Ariav, G., A. Polsky and J. Schiller (2003). Submillisecond precision of the input-output transformation function mediated by fast sodium dendritic spikes in basal dendrites of CA1 pyramidal neurons. *J Neurosci* **23**(21): 7750-7758.

Ascoli, G. A., L. Alonso-Nanclares, S. A. Anderson, G. Barrionuevo, R. Benavides-Piccione, A. Burkhalter, G. Buzsaki, B. Cauli, J. Defelipe, A. Fairen, D. Feldmeyer, G. Fishell, Y. Fregnac, T. F. Freund, D. Gardner, E. P. Gardner, J. H. Goldberg, M. Helmstaedter, S. Hestrin, F. Karube, Z. F. Kisvarday, B. Lambolez, D. A. Lewis, O. Marin, H. Markram, A. Munoz, A. Packer, C. C. Petersen, K. S. Rockland, J. Rossier, B. Rudy, P. Somogyi, J. F. Staiger, G. Tamas, A. M. Thomson, M. Toledo-Rodriguez, Y. Wang, D. C. West and R. Yuste (2008). Petilla terminology: nomenclature of

features of GABAergic interneurons of the cerebral cortex. *Nat Rev Neurosci* **9**(7): 557-568.

Barth, A. M., E. S. Vizi, T. Zelles and B. Lendvai (2008). Alpha2-adrenergic receptors modify dendritic spike generation via HCN channels in the prefrontal cortex. *J Neurophysiol* **99**(1): 394-401.

Bernard, C. and D. Johnston (2003). Distance-dependent modifiable threshold for action potential back-propagation in hippocampal dendrites. *J Neurophysiol* **90**(3): 1807-1816.

Bi, G. Q. and M. M. Poo (1998). Synaptic modifications in cultured hippocampal neurons: dependence on spike timing, synaptic strength, and postsynaptic cell type. *J Neurosci* **18**(24): 10464-10472.

Branco, T. and M. Hausser (2010). The single dendritic branch as a fundamental functional unit in the nervous system. *Curr Opin Neurobiol* **20**(4): 494-502.

Branco, T. and M. Hausser (2011). Synaptic integration gradients in single cortical pyramidal cell dendrites. *Neuron* **69**(5): 885-892.

Buhl, E. H., Z. S. Han, Z. Lorinczi, V. V. Stezhka, S. V. Karnup and P. Somogyi (1994). Physiological properties of anatomically identified axo-axonic cells in the rat hippocampus. *J Neurophysiol* **71**(4): 1289-1307.

Burgess, N., E. A. Maguire and J. O'Keefe (2002). The human hippocampus and spatial and episodic memory. *Neuron* **35**(4): 625-641.

Buzsáki, G. (2005). Theta rhythm of navigation: link between path integration and landmark navigation, episodic and semantic memory. *Hippocampus* **15**(7): 827-840.

Buzsáki, G. *Rhythms of the brain*. Oxford University Press, Oxford ; New York, 2006.

Byrne, J. H. Learning and memory : a comprehensive reference. Elsevier, Amsterdam, Netherlands ; San Diego, California, 2008.

Calixto, E., E. J. Galvan, J. P. Card and G. Barrionuevo (2008). Coincidence detection of convergent perforant path and mossy fibre inputs by CA3 interneurons. *J Physiol* **586**(Pt 11): 2695-2712.

Castro, N. G. and E. X. Albuquerque (1995). alpha-Bungarotoxin-sensitive hippocampal nicotinic receptor channel has a high calcium permeability. *Biophys J* **68**(2): 516-524.

Chalifoux, J. R. and A. G. Carter (2011). Glutamate spillover promotes the generation of NMDA spikes. *J Neurosci* **31**(45): 16435-16446.

Chiovini, B., G. F. Turi, G. Katona, A. Kaszas, F. Erdelyi, G. Szabo, H. Monyer, A. Csakanyi, E. S. Vizi and B. Rozsa (2010). Enhanced dendritic action potential backpropagation in parvalbumin-positive basket cells during sharp wave activity. *Neurochem Res* **35**(12): 2086-2095.

Combs, C. A., A. Smirnov, D. Chess, D. B. McGavern, J. L. Schroeder, J. Riley, S. S. Kang, M. Lugar-Hammer, A. Gandjbakhche, J. R. Knutson and R. S. Balaban (2011). Optimizing multiphoton fluorescence microscopy light collection from living tissue by noncontact total emission detection (epiTED). *J Microsc* **241**(2): 153-161.

Conchello, J. A. and J. W. Lichtman (2005). Optical sectioning microscopy. *Nat Methods* **2**(12): 920-931.

Cosgrove, K. E., E. J. Galvan, S. D. Meriney and G. Barrionuevo (2010). Area CA3 interneurons receive two spatially segregated mossy fiber inputs. *Hippocampus* **20**(9): 1003-1009.

Couey, J. J., R. M. Meredith, S. Spijker, R. B. Poorthuis, A. B. Smit, A. B. Brussaard and H. D. Mansvelder (2007). Distributed Network Actions by Nicotine Increase the Threshold for Spike-Timing-Dependent Plasticity in Prefrontal Cortex. *Neuron* **54**(1): 73-87.

Crochet, S., P. Fuentealba, I. Timofeev and M. Steriade (2004). Selective amplification of neocortical neuronal output by fast prepotentials in vivo. *Cereb Cortex* **14**(10): 1110-1121.

Dani, J. A. and D. Bertrand (2007). Nicotinic acetylcholine receptors and nicotinic cholinergic mechanisms of the central nervous system. *Annu Rev Pharmacol Toxicol* **47**: 699-729.

Dani, J. A., D. Ji and F. M. Zhou (2001). Synaptic plasticity and nicotine addiction. *Neuron* **31**(3): 349-352.

Dani, J. A., K. A. Radcliffe and V. I. Pidoplichko (2000). Variations in desensitization of nicotinic acetylcholine receptors from hippocampus and midbrain dopamine areas. *Eur J Pharmacol* **393**(1-3): 31-38.

Davie, J. T., B. A. Clark and M. Hausser (2008). The origin of the complex spike in cerebellar Purkinje cells. *J Neurosci* **28**(30): 7599-7609.

Denk, W., J. H. Strickler and W. W. Webb (1990). Two-photon laser scanning fluorescence microscopy. *Science* **248**(4951): 73-76.

Ding, J. B., K. T. Takasaki and B. L. Sabatini (2009). Supraresolution imaging in brain slices using stimulated-emission depletion two-photon laser scanning microscopy. *Neuron* **63**(4): 429-437.

Duemani Reddy, G., K. Kelleher, R. Fink and P. Saggau (2008). Three-dimensional random access multiphoton microscopy for functional imaging of neuronal activity. *Nat Neurosci* **11**(6): 713-720.

Eccles, J. C. *The physiology of synapses*. Springer, Berlin,, 1964.

Emri, Z., K. Antal, A. I. Gulyas, M. Megias and T. F. Freund (2001). Electrotonic profile and passive propagation of synaptic potentials in three subpopulations of hippocampal CA1 interneurons. *Neuroscience* **104**(4): 1013-1026.

Fan, G. Y., H. Fujisaki, A. Miyawaki, R. K. Tsay, R. Y. Tsien and M. H. Ellisman (1999). Video-rate scanning two-photon excitation fluorescence microscopy and ratio imaging with cameleons. *Biophys J* **76**(5): 2412-2420.

Fayuk, D. and J. L. Yakel (2005). Ca²⁺ permeability of nicotinic acetylcholine receptors in rat hippocampal CA1 interneurons. *J Physiol* **566**(Pt 3): 759-768.

Fitzpatrick, J. S., A. M. Hagenston, D. N. Hertle, K. E. Gipson, L. Bertetto-D'Angelo and M. F. Yeckel (2009). Inositol-1,4,5-trisphosphate receptor-mediated Ca²⁺ waves in pyramidal neuron dendrites propagate through hot spots and cold spots. *J Physiol* **587**(Pt 7): 1439-1459.

Flusberg, B. A., E. D. Cocker, W. Piyawattanametha, J. C. Jung, E. L. Cheung and M. J. Schnitzer (2005). Fiber-optic fluorescence imaging. *Nat Methods* **2**(12): 941-950.

Frazier, C. J., Y. D. Rollins, C. R. Breese, S. Leonard, R. Freedman and T. V. Dunwiddie (1998). Acetylcholine activates an alpha-bungarotoxin-sensitive nicotinic current in rat hippocampal interneurons, but not pyramidal cells. *J Neurosci* **18**(4): 1187-1195.

Freund, T. F. (2003). Interneuron Diversity series: Rhythm and mood in perisomatic inhibition. *Trends Neurosci* **26**(9): 489-495.

Freund, T. F. and G. Buzsaki (1996). Interneurons of the hippocampus. *Hippocampus* **6**(4): 347-470.

Frick, A., W. Zieglgansberger and H. U. Dodt (2001). Glutamate receptors form hot spots on apical dendrites of neocortical pyramidal neurons. *J Neurophysiol* **86**(3): 1412-1421.

Frostig, R. D. (2009). In vivo optical imaging of brain function. *Frontiers in neuroscience*. Boca Raton, CRC Press.

Fucile, S. (2004). Ca²⁺ permeability of nicotinic acetylcholine receptors. *Cell Calcium* **35**(1): 1-8.

Garaschuk, O., R. I. Milos, C. Grienberger, N. Marandi, H. Adelsberger and A. Konnerth (2006). Optical monitoring of brain function in vivo: from neurons to networks. *Pflugers Arch* **453**(3): 385-396.

Gasparini, S., M. Migliore and J. C. Magee (2004). On the initiation and propagation of dendritic spikes in CA1 pyramidal neurons. *J Neurosci* **24**(49): 11046-11056.

Gastrein, P., E. Campanac, C. Gassel, R. H. Cudmore, A. Bialowas, E. Carlier, L. Fronzaroli-Molinieres, N. Ankri and D. Debanne (2011). The role of hyperpolarization-activated cationic current in spike-time precision and intrinsic resonance in cortical neurons in vitro. *J Physiol* **589**(Pt 15): 3753-3773.

Goldberg, J. H., G. Tamas, D. Aronov and R. Yuste (2003a). Calcium microdomains in aspiny dendrites. *Neuron* **40**(4): 807-821.

Goldberg, J. H., R. Yuste and G. Tamas (2003b). Ca²⁺ imaging of mouse neocortical interneurone dendrites: contribution of Ca²⁺-permeable AMPA and NMDA receptors to subthreshold Ca²⁺-dynamics. *J Physiol* **551**(Pt 1): 67-78.

Golding, N. L., H. Y. Jung, T. Mickus and N. Spruston (1999). Dendritic calcium spike initiation and repolarization are controlled by distinct potassium channel subtypes in CA1 pyramidal neurons. *J Neurosci* **19**(20): 8789-8798.

Golding, N. L., W. L. Kath and N. Spruston (2001). Dichotomy of action-potential backpropagation in CA1 pyramidal neuron dendrites. *J Neurophysiol* **86**(6): 2998-3010.

Golding, N. L., T. J. Mickus, Y. Katz, W. L. Kath and N. Spruston (2005). Factors mediating powerful voltage attenuation along CA1 pyramidal neuron dendrites. *J Physiol* **568**(Pt 1): 69-82.

Golding, N. L., N. P. Staff and N. Spruston (2002). Dendritic spikes as a mechanism for cooperative long-term potentiation. *Nature* **418**(6895): 326-331.

Gomez Gonzalez, J. F., B. W. Mel and P. Poirazi (2011). Distinguishing Linear vs. Non-Linear Integration in CA1 Radial Oblique Dendrites: It's about Time. *Front Comput Neurosci* **5**: 44.

Gordon, U., A. Polsky and J. Schiller (2006). Plasticity compartments in basal dendrites of neocortical pyramidal neurons. *J Neurosci* **26**(49): 12717-12726.

Göbel, W. and F. Helmchen (2007). In vivo calcium imaging of neural network function. *Physiology (Bethesda)* **22**: 358-365.

Göbel, W., B. M. Kampa and F. Helmchen (2007). Imaging cellular network dynamics in three dimensions using fast 3D laser scanning. *Nat Methods* **4**(1): 73-79.

Göppert-Mayer, M. (1931). Elementarakte mit zwei Quantensprüngen. *Annalen der Physik* **401**(3): 273-294.

Grewe, B. F., F. F. Voigt, M. van 't Hoff and F. Helmchen (2011). Fast two-layer two-photon imaging of neuronal cell populations using an electrically tunable lens. *Biomed Opt Express* **2**(7): 2035-2046.

Gu, Z. and J. L. Yakel (2011). Timing-dependent septal cholinergic induction of dynamic hippocampal synaptic plasticity. *Neuron* **71**(1): 155-165.

Gulledge, A. T., B. M. Kampa and G. J. Stuart (2005). Synaptic integration in dendritic trees. *J Neurobiol* **64**(1): 75-90.

Gulyas, A. I., M. Megias, Z. Emri and T. F. Freund (1999). Total number and ratio of excitatory and inhibitory synapses converging onto single interneurons of different types in the CA1 area of the rat hippocampus. *J Neurosci* **19**(22): 10082-10097.

Hajos, N., T. J. Ellender, R. Zemankovics, E. O. Mann, R. Exley, S. J. Cragg, T. F. Freund and O. Paulsen (2009). Maintaining network activity in submerged hippocampal slices: importance of oxygen supply. *Eur J Neurosci* **29**(2): 319-327.

Hajos, N. and I. Mody (1997). Synaptic communication among hippocampal interneurons: properties of spontaneous IPSCs in morphologically identified cells. *J Neurosci* **17**(21): 8427-8442.

Hajos, N. and I. Mody (2009). Establishing a physiological environment for visualized in vitro brain slice recordings by increasing oxygen supply and modifying aCSF content. *J Neurosci Methods* **183**(2): 107-113.

Halasy, K., S. R. Cobb, E. H. Buhl, G. Nyiri and P. Somogyi (1996). Sites of synaptic junctions established by a GABAergic basket cell on an interneuron in the CA1 area of the rat hippocampus. *Neurobiology (Bp)* **4**(3): 269-270.

Hao, J. and T. G. Oertner (2011). Depolarization gates spine calcium transients and spike-timing-dependent potentiation. *Curr Opin Neurobiol.*

Hausser, M., N. Spruston and G. J. Stuart (2000). Diversity and dynamics of dendritic signaling. *Science* **290**(5492): 739-744.

Helmchen, F. and W. Denk (2005). Deep tissue two-photon microscopy. *Nat Methods* **2**(12): 932-940.

Helmchen, F., K. Svoboda, W. Denk and D. W. Tank (1999). In vivo dendritic calcium dynamics in deep-layer cortical pyramidal neurons. *Nat Neurosci* **2**(11): 989-996.

Holmgren, C. D. and Y. Zilberter (2001). Coincident spiking activity induces long-term changes in inhibition of neocortical pyramidal cells. *J Neurosci* **21**(20): 8270-8277.

Holthoff, K., Y. Kovalchuk, R. Yuste and A. Konnerth (2004). Single-shock LTD by local dendritic spikes in pyramidal neurons of mouse visual cortex. *J Physiol* **560**(Pt 1): 27-36.

Hu, H., M. Martina and P. Jonas (2010). Dendritic mechanisms underlying rapid synaptic activation of fast-spiking hippocampal interneurons. *Science* **327**(5961): 52-58.

Hu, H., K. Vervaeke, L. J. Graham and J. F. Storm (2009). Complementary theta resonance filtering by two spatially segregated mechanisms in CA1 hippocampal pyramidal neurons. *J Neurosci* **29**(46): 14472-14483.

Hubener, M. and T. Bonhoeffer (2005). Visual cortex: two-photon excitement. *Curr Biol* **15**(6): R205-208.

Iyer, V., T. M. Hoogland and P. Saggau (2006). Fast functional imaging of single neurons using random-access multiphoton (RAMP) microscopy. *J Neurophysiol* **95**(1): 535-545.

Iyer, V., B. E. Losavio and P. Saggau (2003). Compensation of spatial and temporal dispersion for acousto-optic multiphoton laser-scanning microscopy. *J Biomed Opt* **8**(3): 460-471.

Jahr, C. E. and C. F. Stevens (1990). Voltage dependence of NMDA-activated macroscopic conductances predicted by single-channel kinetics. *J Neurosci* **10**(9): 3178-3182.

Ji, D., R. Lape and J. A. Dani (2001). Timing and location of nicotinic activity enhances or depresses hippocampal synaptic plasticity. *Neuron* **31**(1): 131-141.

Jia, H., N. L. Rochefort, X. Chen and A. Konnerth (2010). Dendritic organization of sensory input to cortical neurons in vivo. *Nature* **464**(7293): 1307-1312.

Job, C. and J. Eberwine (2001). Identification of sites for exponential translation in living dendrites. *Proc Natl Acad Sci U S A* **98**(23): 13037-13042.

Kamondi, A., L. Acsady and G. Buzsaki (1998). Dendritic spikes are enhanced by cooperative network activity in the intact hippocampus. *J Neurosci* **18**(10): 3919-3928.

Kampa, B. M., J. J. Letzkus and G. J. Stuart (2006). Requirement of dendritic calcium spikes for induction of spike-timing-dependent synaptic plasticity. *J Physiol* **574**(Pt 1): 283-290.

Kandel, E. R., J. M. Brookhart, V. B. Mountcastle, S. R. Geiger and American Physiological Society (1887-). *Cellular biology of neurons*. American Physiological Society, Bethesda, Md., 1977.

Kaplan, A., N. Friedman and N. Davidson (2001). Acousto-optic lens with very fast focus scanning. *Opt Lett* **26**: 1078-1080.

Katona, G., A. Kaszas, G. F. Turi, N. Hajos, G. Tamas, E. S. Vizi and B. Rozsa (2011). Roller Coaster Scanning reveals spontaneous triggering of dendritic spikes in CA1 interneurons. *Proc Natl Acad Sci U S A* **108**(5): 2148-2153.

Katona, G., G. Szalay, P. Maak, A. Kaszas, M. Veress, D. Hillier, B. Chiovini, E. S. Vizi, B. Roska and B. Rozsa (2012). Fast two-photon in vivo imaging with three-dimensional random-access scanning in large tissue volumes. *Nat Methods* **9**(2): 201-208.

Katz, Y., V. Menon, D. A. Nicholson, Y. Geinisman, W. L. Kath and N. Spruston (2009). Synapse distribution suggests a two-stage model of dendritic integration in CA1 pyramidal neurons. *Neuron* **63**(2): 171-177.

Kerr, J. N. and W. Denk (2008). Imaging in vivo: watching the brain in action. *Nat Rev Neurosci* **9**(3): 195-205.

Khiroug, L., R. Giniatullin, R. C. Klein, D. Fayuk and J. L. Yakel (2003). Functional mapping and Ca²⁺ regulation of nicotinic acetylcholine receptor channels in rat hippocampal CA1 neurons. *J Neurosci* **23**(27): 9024-9031.

Kirkby, P. A., K. M. Srinivas Nadella and R. A. Silver (2010). A compact Acousto-Optic Lens for 2D and 3D femtosecond based 2-photon microscopy. *Opt Express* **18**(13): 13721-13745.

Klausberger, T. (2009). GABAergic interneurons targeting dendrites of pyramidal cells in the CA1 area of the hippocampus. *Eur J Neurosci* **30**(6): 947-957.

Klausberger, T., P. J. Magill, L. F. Marton, J. D. Roberts, P. M. Cobden, G. Buzsaki and P. Somogyi (2003). Brain-state- and cell-type-specific firing of hippocampal interneurons in vivo. *Nature* **421**(6925): 844-848.

Klausberger, T. and P. Somogyi (2008). Neuronal diversity and temporal dynamics: the unity of hippocampal circuit operations. *Science* **321**(5885): 53-57.

Koester, H. J., D. Baur, R. Uhl and S. W. Hell (1999). Ca²⁺ fluorescence imaging with pico- and femtosecond two-photon excitation: signal and photodamage. *Biophys J* **77**(4): 2226-2236.

Kole, M. H. and G. J. Stuart (2012). Signal processing in the axon initial segment. *Neuron* **73**(2): 235-247.

Lamsa, K., J. H. Heeroma and D. M. Kullmann (2005). Hebbian LTP in feed-forward inhibitory interneurons and the temporal fidelity of input discrimination. *Nat Neurosci* **8**(7): 916-924.

Lamsa, K. P., J. H. Heeroma, P. Somogyi, D. A. Rusakov and D. M. Kullmann (2007). Anti-Hebbian long-term potentiation in the hippocampal feedback inhibitory circuit. *Science* **315**(5816): 1262-1266.

Larkum, M. E., K. M. Kaiser and B. Sakmann (1999a). Calcium electrogenesis in distal apical dendrites of layer 5 pyramidal cells at a critical frequency of back-propagating action potentials. *Proc Natl Acad Sci U S A* **96**(25): 14600-14604.

Larkum, M. E. and T. Nevian (2008). Synaptic clustering by dendritic signalling mechanisms. *Curr Opin Neurobiol* **18**(3): 321-331.

Larkum, M. E., T. Nevian, M. Sandler, A. Polsky and J. Schiller (2009). Synaptic integration in tuft dendrites of layer 5 pyramidal neurons: a new unifying principle. *Science* **325**(5941): 756-760.

Larkum, M. E. and J. J. Zhu (2002). Signaling of layer 1 and whisker-evoked Ca²⁺ and Na⁺ action potentials in distal and terminal dendrites of rat neocortical pyramidal neurons in vitro and in vivo. *J Neurosci* **22**(16): 6991-7005.

Larkum, M. E., J. J. Zhu and B. Sakmann (1999b). A new cellular mechanism for coupling inputs arriving at different cortical layers. *Nature* **398**(6725): 338-341.

Lechleiter, J. D., D. T. Lin and I. Sieneart (2002). Multi-photon laser scanning microscopy using an acoustic optical deflector. *Biophys J* **83**(4): 2292-2299.

Lei, S. and C. J. McBain (2002). Distinct NMDA receptors provide differential modes of transmission at mossy fiber-interneuron synapses. *Neuron* **33**(6): 921-933.

Lei, S. and C. J. McBain (2004). Two Loci of expression for long-term depression at hippocampal mossy fiber-interneuron synapses. *J Neurosci* **24**(9): 2112-2121.

Llinas, R. and R. Hess (1976). Tetrodotoxin-resistant dendritic spikes in avian Purkinje cells. *Proc Natl Acad Sci U S A* **73**(7): 2520-2523.

Llinas, R., C. Nicholson, J. A. Freeman and D. E. Hillman (1968). Dendritic spikes and their inhibition in alligator Purkinje cells. *Science* **160**(3832): 1132-1135.

Llinas, R. and M. Sugimori (1980a). Electrophysiological properties of in vitro Purkinje cell dendrites in mammalian cerebellar slices. *J Physiol* **305**: 197-213.

Llinas, R. and M. Sugimori (1980b). Electrophysiological properties of in vitro Purkinje cell somata in mammalian cerebellar slices. *J Physiol* **305**: 171-195.

London, M. and M. Hausser (2005). Dendritic computation. *Annu Rev Neurosci* **28**: 503-532.

London, M. and I. Segev (2001). Synaptic scaling in vitro and in vivo. *Nat Neurosci* **4**(9): 853-855.

Lorente de Nó, R. (1938). Analysis of the activity of the chains of internuncial neurons. *J. Neurophysiol.* **1**(3): 207-244.

Lorincz, A. and Z. Nusser (2008). Cell-type-dependent molecular composition of the axon initial segment. *J Neurosci* **28**(53): 14329-14340.

Lorincz, A. and Z. Nusser (2010). Molecular identity of dendritic voltage-gated sodium channels. *Science* **328**(5980): 906-909.

Lorincz, A., B. Rozsa, G. Katona, E. S. Vizi and G. Tamas (2007). Differential distribution of NCX1 contributes to spine-dendrite compartmentalization in CA1 pyramidal cells. *Proc Natl Acad Sci U S A* **104**(3): 1033-1038.

Losonczy, A. and J. C. Magee (2006). Integrative properties of radial oblique dendrites in hippocampal CA1 pyramidal neurons. *Neuron* **50**(2): 291-307.

Losonczy, A., J. K. Makara and J. C. Magee (2008). Compartmentalized dendritic plasticity and input feature storage in neurons. *Nature* **452**(7186): 436-441.

Maccaferri, G. and R. Dingledine (2002). Control of feedforward dendritic inhibition by NMDA receptor-dependent spike timing in hippocampal interneurons. *J Neurosci* **22**(13): 5462-5472.

Magee, J. C. and E. P. Cook (2000). Somatic EPSP amplitude is independent of synapse location in hippocampal pyramidal neurons. *Nat Neurosci* **3**(9): 895-903.

Magee, J. C. and D. Johnston (1997). A synaptically controlled, associative signal for Hebbian plasticity in hippocampal neurons. *Science* **275**(5297): 209-213.

Magee, J. C. and D. Johnston (2005). Plasticity of dendritic function. *Curr Opin Neurobiol* **15**(3): 334-342.

Maggi, L., E. Sola, F. Minneci, C. Le Magueresse, J. P. Changeux and E. Cherubini (2004). Persistent decrease in synaptic efficacy induced by nicotine at Schaffer collateral-CA1 synapses in the immature rat hippocampus. *J Physiol* **559**(Pt 3): 863-874.

Major, G., A. Polsky, W. Denk, J. Schiller and D. W. Tank (2008). Spatiotemporally graded NMDA spike/plateau potentials in basal dendrites of neocortical pyramidal neurons. *J Neurophysiol* **99**(5): 2584-2601.

Makara, J. K., A. Losonczy, Q. Wen and J. C. Magee (2009). Experience-dependent compartmentalized dendritic plasticity in rat hippocampal CA1 pyramidal neurons. *Nat Neurosci* **12**(12): 1485-1487.

Malenka, R. C. and R. A. Nicoll (1999). Long-term potentiation--a decade of progress? *Science* **285**(5435): 1870-1874.

Mansvelder, H. D. and D. S. McGehee (2000). Long-term potentiation of excitatory inputs to brain reward areas by nicotine. *Neuron* **27**(2): 349-357.

Maravall, M., Z. F. Mainen, B. L. Sabatini and K. Svoboda (2000). Estimating intracellular calcium concentrations and buffering without wavelength ratioing. *Biophys J* **78**(5): 2655-2667.

Markram, H., J. Lubke, M. Frotscher and B. Sakmann (1997). Regulation of synaptic efficacy by coincidence of postsynaptic APs and EPSPs. *Science* **275**(5297): 213-215.

Marr, D. *Vision : a computational investigation into the human representation and processing of visual information*. W.H. Freeman, San Francisco, 1982.

Martin, K. A., P. Somogyi and D. Whitteridge (1983). Physiological and morphological properties of identified basket cells in the cat's visual cortex. *Exp Brain Res* **50**(2-3): 193-200.

- Martin, S. J., P. D. Grimwood and R. G. Morris (2000). Synaptic plasticity and memory: an evaluation of the hypothesis. *Annu Rev Neurosci* **23**: 649-711.
- Martina, M., I. Vida and P. Jonas (2000). Distal initiation and active propagation of action potentials in interneuron dendrites. *Science* **287**(5451): 295-300.
- Matsuzaki, M., G. C. Ellis-Davies, T. Nemoto, Y. Miyashita, M. Iino and H. Kasai (2001). Dendritic spine geometry is critical for AMPA receptor expression in hippocampal CA1 pyramidal neurons. *Nat Neurosci* **4**(11): 1086-1092.
- McGehee, D. S. (2002). Nicotinic receptors and hippocampal synaptic plasticity ... it's all in the timing. *Trends Neurosci* **25**(4): 171-172.
- Megias, M., Z. Emri, T. F. Freund and A. I. Gulyas (2001). Total number and distribution of inhibitory and excitatory synapses on hippocampal CA1 pyramidal cells. *Neuroscience* **102**(3): 527-540.
- Milojkovic, B. A., M. S. Radojicic and S. D. Antic (2005a). A strict correlation between dendritic and somatic plateau depolarizations in the rat prefrontal cortex pyramidal neurons. *J Neurosci* **25**(15): 3940-3951.
- Milojkovic, B. A., J. P. Wuskell, L. M. Loew and S. D. Antic (2005b). Initiation of sodium spikelets in basal dendrites of neocortical pyramidal neurons. *J Membr Biol* **208**(2): 155-169.
- Murphy, K. P., G. P. Reid, D. R. Trentham and T. V. Bliss (1997). Activation of NMDA receptors is necessary for the induction of associative long-term potentiation in area CA1 of the rat hippocampal slice. *J Physiol* **504** (Pt 2): 379-385.

Narayanan, R. and D. Johnston (2007). Long-term potentiation in rat hippocampal neurons is accompanied by spatially widespread changes in intrinsic oscillatory dynamics and excitability. *Neuron* **56**(6): 1061-1075.

Nevian, T., M. E. Larkum, A. Polsky and J. Schiller (2007). Properties of basal dendrites of layer 5 pyramidal neurons: a direct patch-clamp recording study. *Nat Neurosci* **10**(2): 206-214.

Ngoi, B. K., K. Venkatakrishnan, L. E. Lim and B. Tan (2001). Angular dispersion compensation for acousto-optic devices used for ultrashort-pulsed laser micromachining. *Opt Express* **9**(4): 200-206.

Nguyen, Q. T., N. Callamaras, C. Hsieh and I. Parker (2001). Construction of a two-photon microscope for video-rate Ca(2+) imaging. *Cell Calcium* **30**(6): 383-393.

Nolan, M. F., G. Malleret, J. T. Dudman, D. L. Buhl, B. Santoro, E. Gibbs, S. Vronskaya, G. Buzsaki, S. A. Siegelbaum, E. R. Kandel and A. Morozov (2004). A behavioral role for dendritic integration: HCN1 channels constrain spatial memory and plasticity at inputs to distal dendrites of CA1 pyramidal neurons. *Cell* **119**(5): 719-732.

Nowak, L., P. Bregestovski, P. Ascher, A. Herbet and A. Prochiantz (1984). Magnesium gates glutamate-activated channels in mouse central neurones. *Nature* **307**(5950): 462-465.

O'Connor, D. H., D. Huber and K. Svoboda (2009). Reverse engineering the mouse brain. *Nature* **461**(7266): 923-929.

O'Keefe, J. and J. Dostrovsky (1971). The hippocampus as a spatial map. Preliminary evidence from unit activity in the freely-moving rat. *Brain Res* **34**(1): 171-175.

Oakley, J. C., P. C. Schwindt and W. E. Crill (2001a). Dendritic calcium spikes in layer 5 pyramidal neurons amplify and limit transmission of ligand-gated dendritic current to soma. *J Neurophysiol* **86**(1): 514-527.

Oakley, J. C., P. C. Schwindt and W. E. Crill (2001b). Initiation and propagation of regenerative Ca(2+)-dependent potentials in dendrites of layer 5 pyramidal neurons. *J Neurophysiol* **86**(1): 503-513.

Paoletti, P. and J. Neyton (2007). NMDA receptor subunits: function and pharmacology. *Curr Opin Pharmacol* **7**(1): 39-47.

Pelkey, K. A., L. Topolnik, J. C. Lacaille and C. J. McBain (2006). Compartmentalized Ca(2+) channel regulation at divergent mossy-fiber release sites underlies target cell-dependent plasticity. *Neuron* **52**(3): 497-510.

Penttonen, M., A. Kamondi, L. Acsady and G. Buzsaki (1998). Gamma frequency oscillation in the hippocampus of the rat: intracellular analysis in vivo. *Eur J Neurosci* **10**(2): 718-728.

Poirazi, P., T. Brannon and B. W. Mel (2003a). Arithmetic of subthreshold synaptic summation in a model CA1 pyramidal cell. *Neuron* **37**(6): 977-987.

Poirazi, P., T. Brannon and B. W. Mel (2003b). Pyramidal neuron as two-layer neural network. *Neuron* **37**(6): 989-999.

Polsky, A., B. W. Mel and J. Schiller (2004). Computational subunits in thin dendrites of pyramidal cells. *Nat Neurosci* **7**(6): 621-627.

Price, J. L. and T. P. Powell (1970). The synaptology of the granule cells of the olfactory bulb. *J Cell Sci* **7**(1): 125-155.

Purves, D. *Neuroscience*. Sinauer, Sunderland, Mass., 2008.

Rall, W. (1969a). Distributions of potential in cylindrical coordinates and time constants for a membrane cylinder. *Biophys J* **9**(12): 1509-1541.

Rall, W. (1969b). Time constants and electrotonic length of membrane cylinders and neurons. *Biophys J* **9**(12): 1483-1508.

Rall, W., G. M. Shepherd, T. S. Reese and M. W. Brightman (1966). Dendrodendritic synaptic pathway for inhibition in the olfactory bulb. *Exp Neurol* **14**(1): 44-56.

Ramón y Cajal, S. *Histologie du système nerveux de l'homme & des vertébrés*. A. Maloine, Paris, 1909.

Ramón y Cajal, S. *New ideas on the structure of the nervous system in man and vertebrates*. MIT Press, Cambridge, Mass., 1990.

Reddy, G. D. and P. Saggau (2005). Fast three-dimensional laser scanning scheme using acousto-optic deflectors. *J Biomed Opt* **10**(6): 064038.

Remy, S. and N. Spruston (2007). Dendritic spikes induce single-burst long-term potentiation. *Proc Natl Acad Sci U S A* **104**(43): 17192-17197.

Rhodes, P. (2006). The properties and implications of NMDA spikes in neocortical pyramidal cells. *J Neurosci* **26**(25): 6704-6715.

Rozsa, B., G. Katona, A. Kaszas, R. Szipocs and E. S. Vizi (2008). Dendritic nicotinic receptors modulate backpropagating action potentials and long-term plasticity of interneurons. *Eur J Neurosci* **27**(2): 364-377.

Rozsa, B., G. Katona, E. S. Vizi, Z. Varallyay, A. Saghy, L. Valenta, P. Maak, J. Fekete, A. Banyasz and R. Szipocs (2007). Random access three-dimensional two-photon microscopy. *Appl Opt* **46**(10): 1860-1865.

Rozsa, B., T. Zelles, E. S. Vizi and B. Lendvai (2004). Distance-dependent scaling of calcium transients evoked by backpropagating spikes and synaptic activity in dendrites of hippocampal interneurons. *J Neurosci* **24**(3): 661-670.

Sabatini, B. L., M. Maravall and K. Svoboda (2001). Ca²⁺ signaling in dendritic spines. *Curr Opin Neurobiol* **11**(3): 349-356.

Sabatini, B. L. and K. Svoboda (2000). Analysis of calcium channels in single spines using optical fluctuation analysis. *Nature* **408**(6812): 589-593.

Schiller, J., G. Major, H. J. Koester and Y. Schiller (2000). NMDA spikes in basal dendrites of cortical pyramidal neurons. *Nature* **404**(6775): 285-289.

Schiller, J. and Y. Schiller (2001). NMDA receptor-mediated dendritic spikes and coincident signal amplification. *Curr Opin Neurobiol* **11**(3): 343-348.

Schiller, J., Y. Schiller, G. Stuart and B. Sakmann (1997). Calcium action potentials restricted to distal apical dendrites of rat neocortical pyramidal neurons. *J Physiol* **505** (Pt 3): 605-616.

Siegel, G. J. *Basic neurochemistry : molecular, cellular, and medical aspects*. Elsevier Academic, Burlington, MA, 2006.

Sjostrom, P. J., E. A. Rancz, A. Roth and M. Hausser (2008). Dendritic excitability and synaptic plasticity. *Physiol Rev* **88**(2): 769-840.

Smith, M. A., G. C. Ellis-Davies and J. C. Magee (2003). Mechanism of the distance-dependent scaling of Schaffer collateral synapses in rat CA1 pyramidal neurons. *J Physiol* **548**(Pt 1): 245-258.

Somogyi, P., T. F. Freund and A. Cowey (1982). The axo-axonic interneuron in the cerebral cortex of the rat, cat and monkey. *Neuroscience* **7**(11): 2577-2607.

Somogyi, P. and T. Klausberger (2005). Defined types of cortical interneurone structure space and spike timing in the hippocampus. *J Physiol* **562**(Pt 1): 9-26.

Spencer, W. A. and E. R. Kandel (1961). Electrophysiology of hippocampal neurons: IV. Fast prepotentials. *J Neurophysiol* **24**(3): 272-285.

Spruston, N. (2008). Pyramidal neurons: dendritic structure and synaptic integration. *Nat Rev Neurosci* **9**(3): 206-221.

Stuart, G. and N. Spruston (1998). Determinants of voltage attenuation in neocortical pyramidal neuron dendrites. *J Neurosci* **18**(10): 3501-3510.

Stuart, G., N. Spruston and M. Häusser. *Dendrites*. Oxford University Press, New York, 1999.

Stuart, G., N. Spruston and M. Häusser. *Dendrites*. Oxford University Press, Oxford ; New York, 2007.

Stuart, G., N. Spruston, B. Sakmann and M. Hausser (1997). Action potential initiation and backpropagation in neurons of the mammalian CNS. *Trends Neurosci* **20**(3): 125-131.

Stuart, G. J. and M. Hausser (2001). Dendritic coincidence detection of EPSPs and action potentials. *Nat Neurosci* **4**(1): 63-71.

Stuart, G. J. and B. Sakmann (1994). Active propagation of somatic action potentials into neocortical pyramidal cell dendrites. *Nature* **367**(6458): 69-72.

Svoboda, K., W. Denk, D. Kleinfeld and D. W. Tank (1997). In vivo dendritic calcium dynamics in neocortical pyramidal neurons. *Nature* **385**(6612): 161-165.

Svoboda, K., F. Helmchen, W. Denk and D. W. Tank (1999). Spread of dendritic excitation in layer 2/3 pyramidal neurons in rat barrel cortex in vivo. *Nat Neurosci* **2**(1): 65-73.

Svoboda, K., D. W. Tank and W. Denk (1996). Direct measurement of coupling between dendritic spines and shafts. *Science* **272**(5262): 716-719.

Svoboda, K. and R. Yasuda (2006). Principles of two-photon excitation microscopy and its applications to neuroscience. *Neuron* **50**(6): 823-839.

Szabadics, J., C. Varga, G. Molnar, S. Olah, P. Barzo and G. Tamas (2006). Excitatory effect of GABAergic axo-axonic cells in cortical microcircuits. *Science* **311**(5758): 233-235.

Takacs, V. T., T. Klausberger, P. Somogyi, T. F. Freund and A. I. Gulyas (2011). Extrinsic and local glutamatergic inputs of the rat hippocampal CA1 area differentially innervate pyramidal cells and interneurons. *Hippocampus*.

Tamas, G., A. Lorincz, A. Simon and J. Szabadics (2003). Identified sources and targets of slow inhibition in the neocortex. *Science* **299**(5614): 1902-1905.

Tamas, G., J. Szabadics and P. Somogyi (2002). Cell type- and subcellular position-dependent summation of unitary postsynaptic potentials in neocortical neurons. *J Neurosci* **22**(3): 740-747.

Theer, P., M. T. Hasan and W. Denk (2003). Two-photon imaging to a depth of 1000 microm in living brains by use of a Ti:Al₂O₃ regenerative amplifier. *Opt Lett* **28**(12): 1022-1024.

Tibshirani, R., G. Walther and T. Hastie (2001). Estimating the number of clusters in a data set via the gap statistic. *Journal of the Royal Statistical Society: Series B (Statistical Methodology)* **63**(2): 411-423.

Topolnik, L., S. Chamberland, J. G. Pelletier, I. Ran and J. C. Lacaille (2009). Activity-dependent compartmentalized regulation of dendritic Ca²⁺ signaling in hippocampal interneurons. *J Neurosci* **29**(14): 4658-4663.

Tukker, J. J., P. Fuentealba, K. Hartwich, P. Somogyi and T. Klausberger (2007). Cell type-specific tuning of hippocampal interneuron firing during gamma oscillations in vivo. *J Neurosci* **27**(31): 8184-8189.

Turner, R. W., D. E. Meyers and J. L. Barker (1993). Fast pre-potential generation in rat hippocampal CA1 pyramidal neurons. *Neuroscience* **53**(4): 949-959.

Varga, Z., H. Jia, B. Sakmann and A. Konnerth (2011). Dendritic coding of multiple sensory inputs in single cortical neurons in vivo. *Proc Natl Acad Sci U S A* **108**(37): 15420-15425.

Vervaeke, K., A. Lorincz, Z. Nusser and R. A. Silver (2012). Gap junctions compensate for sublinear dendritic integration in an inhibitory network. *Science* **335**(6076): 1624-1628.

Vetter, P., A. Roth and M. Hausser (2001). Propagation of action potentials in dendrites depends on dendritic morphology. *J Neurophysiol* **85**(2): 926-937.

Vizi, S. E., B. Rozsa, A. Mayer, J. P. Kiss, T. Zelles and B. Lendvai (2004). Further evidence for the functional role of nonsynaptic nicotinic acetylcholine receptors. *Eur J Pharmacol* **500**(1-3): 499-508.

Vucinic, D. and T. J. Sejnowski (2007). A compact multiphoton 3D imaging system for recording fast neuronal activity. *PLoS One* **2**(8): e699.

Waters, J., M. Larkum, B. Sakmann and F. Helmchen (2003). Supralinear Ca²⁺ influx into dendritic tufts of layer 2/3 neocortical pyramidal neurons in vitro and in vivo. *J Neurosci* **23**(24): 8558-8567.

Waters, J., A. Schaefer and B. Sakmann (2005). Backpropagating action potentials in neurones: measurement, mechanisms and potential functions. *Prog Biophys Mol Biol* **87**(1): 145-170.

Williams, S. R. and G. J. Stuart (2002). Dependence of EPSP efficacy on synapse location in neocortical pyramidal neurons. *Science* **295**(5561): 1907-1910.

Willig, K. I., S. O. Rizzoli, V. Westphal, R. Jahn and S. W. Hell (2006). STED microscopy reveals that synaptotagmin remains clustered after synaptic vesicle exocytosis. *Nature* **440**(7086): 935-939.

Wimmer, V. C., T. Nevian and T. Kuner (2004). Targeted in vivo expression of proteins in the calyx of Held. *Pflugers Arch* **449**(3): 319-333.

Yuste, R. (2005). Fluorescence microscopy today. *Nat Methods* **2**(12): 902-904.

Yuste, R. and W. Denk (1995). Dendritic spines as basic functional units of neuronal integration. *Nature* **375**(6533): 682-684.

Yuste, R., A. Majewska and K. Holthoff (2000). From form to function: calcium compartmentalization in dendritic spines. *Nat Neurosci* **3**(7): 653-659.

Zipfel, W. R., R. M. Williams and W. W. Webb (2003). Nonlinear magic: multiphoton microscopy in the biosciences. *Nat Biotechnol* **21**(11): 1369-1377.

XIII. LIST OF THE AUTHOR'S PUBLICATIONS

XIII.1. Publications Related to the Thesis

Katona, G.*, A. Kaszas*, G. F. Turi, N. Hajos, G. Tamas, E. S. Vizi and B. Rozsa (2011). Roller Coaster Scanning reveals spontaneous triggering of dendritic spikes in CA1 interneurons. Proc Natl Acad Sci U S A 108(5): 2148-2153.

**These authors contributed equally to this work.*

Chiovini, B., G. F. Turi, G. Katona, **A. Kaszas**, F. Erdelyi, G. Szabo, H. Monyer, A. Csakanyi, E. S. Vizi and B. Rozsa (2010). Enhanced dendritic action potential backpropagation in parvalbumin-positive basket cells during sharp wave activity. Neurochem Res 35(12): 2086-2095.

Rozsa, B., G. Katona, **A. Kaszas**, R. Szipocs and E. S. Vizi (2008). Dendritic nicotinic receptors modulate backpropagating action potentials and long-term plasticity of interneurons. Eur J Neurosci 27(2): 364-377.

XIII.2. Patents Related to the Thesis

Rózsa B, Katona G, Vizi ES, Kaszás A, Turi GF

Method and measuring system for scanning multiple regions of interest (multiple free line scan). E08462011

Rózsa B, Katona G, Vizi ES, Kaszás A, Turi GF

Method and measuring system for scanning multiple regions of interest (multiple free line scan). 12/998,668

XIII.3. Other Publications

G. Katona*, G. Szalay*, P. Maák*, A. Kaszás*, Máté Veress, D. Hillier, B. Chiovini, E. S. Vizi, B. Roska, B. Rózsa (2012) Fast two-photon in vivo imaging with three-dimensional random access scanning in large tissue volumes. *Nat Methods* 9(2): 201-208.

**These authors contributed equally to this work.*

Bhattarai, J. P.*, **A. Kaszas***, S. A. Park, H. Yin, S. J. Park, A. E. Herbison, S. K. Han and I. M. Abraham (2010). Somatostatin inhibition of gonadotropin-releasing hormone neurons in female and male mice. *Endocrinology* 151(7): 3258-3266.

**These authors contributed equally to this work.*

Barabas, K., E. M. Szego, **A. Kaszas**, G. M. Nagy, G. D. Juhasz and I. M. Abraham (2006). Sex differences in oestrogen-induced p44/42 MAPK phosphorylation in the mouse brain in vivo. *J Neuroendocrinol* 18(8): 621-628.

XIV. ACKNOWLEDGEMENTS

There is a multitude of people who aided my efforts to finish my thesis. First of all, I would like to thank my supervisors for guiding me through this wonderful scientific adventure. I am clearly indebted to Balázs, who tirelessly instructed me to learn the elaborate imaging methods and to get accustomed with the practical issues of electrophysiological measurements.

I would like to thank all the people from the Department of Pharmacology for the continuous support and the relentless work.

My thesis would have been much more disorganized and would have lacked many of the well-placed references without the constructive criticism of Dr. Szabolcs Káli, who has thoroughly read my thesis in a very short time to help in bettering it. The questions and discussion by the people from the Institute of Experimental Medicine also helped in shaping both the defense and the thesis to be more coherent.

I would also like to thank my colleagues in the laboratory for all the useful discussions that helped to shape the work and guide it towards the finish line. Gergely Katona took many of his precious time to improve or even develop the methods I worked with, while Gergely Szalay helped to have the setups work at their optimum constantly.

Here I have to thank the students who dared to trust my advice and listened to all the tiring talks on my views of how to improve. I was lucky to see them turn from student to colleague.

My thanks go out to the people at the company Femtonics, who did all in their power to support the research, both devoting their time and the company assets to neuroscience.

Last, but not least, I would like to thank my family for pushing me to finish the thesis. Andi took all the burden of family matters for weeks or even months to help me have the time to write this work, often staying up late and not sparing her energies to help me save on mine. Her proofreading corrected for many minor and major mistakes. Finally, I hope my children can forgive the hours of staying up late and missing their Dad for weeks on end.